学位論文

Optical, electrical and local fine structural characterisation of Rare-Earth doped TiO_2 thin films for application as luminescent phosphors in LEDs

(希土類添加 TiO_2 薄膜の LED 応用に向けた発光、電気、局所構造特性に関する研究)

A thesis submitted to Tokyo University of Science
for the degree of Doctor of Philosophy
in the Department of Physics

Mariko Murayama
The Graduate School of Science
March 2021

’Everything exisits in limited quantity

- especially happiness’

-Pablo Picasso

Contents

List of Figures

List of Tables

ABSTRACT

The work presented throughout this thesis describes study on rare earth-doped TiO_2 luminescent materials, which were fabricated using laser ablation technique. This research mainly focuses on characterisation of luminescent property and understanding mechanics of rare earth-related luminescence and aims to apply these unique materials to efficient LED devices in the future. To achieve these purposes and fulfill scientific interest, this work was planned and approaches of preparing materials and their characterisation are selected. Mainly, estimations which help to understand luminescent properties of rare earth, its mechanics and used materials by experience/modification were paid attentions.

Photoluminescence (PL) and X-ray Absorption Fine Structure (XAFS) are the main experiments for a characterisation of luminescent and local fine structural properties to discuss the connection between them and to find which factor is critical/what is responsible for strong luminescence/stimulating rare earth excitation.

This thesis consists of three parts as follows:

Part 1:
Effect of annealing on luminescent/local fine structural properties of samarium (Sm)-doped TiO_2 thin films and their connection.

Part 2:
Effect of aluminium (Al) co-doping on luminescent/local fine structural properties of neodymium (Nd)-doped TiO_2 thin films and their connection.

Part 3:
Electrical property of Sm-doped TiO_2 (TiO_2:Sm) thin films with ruthenium (Ru) or gold (Au) Schottky contacts and preparation for Deep Level Transient Spectroscopy (DLTS) measurement.

Both part 1 and 2 are discussed from the same viewpoint, assuming local fine structure is one of the keys to enhance rare earth emissions. Part 3 is a brief summary of prerequsite electrical characterisations of TiO_2:Sm for a preparation of junction spectroscopy and device applications.

In part 1, samples with 2 different crystalline phases of TiO_2 (anatase and rutile,

A-/R-) were prepared with different ablation and annealing process. PL and XAFS were employed for characterisation and comparison. PL result revealed that sample prepared with anatase-phase showed emissions in red wavelength region and they were approximately 200 times stronger than that for rutile-phase TiO_2:Sm (R-TiO_2:Sm) samples. In addition, Sm-doped anatase TiO_2 (A-TiO_2:Sm) annealed at 700 °C exhibited the most intense luminescence in all samples. For this result, XAFS measurements were carried out and analysis showed the correlation between PL intensity and local fine structure. For samples with strong emissions, a low symmetrical model with different atomic distance in each of the first and the second nearest neighbours (F.N.N. and S.N.N.) of Sm atoms showed good agreement through fitting analysis, whereas a high symmetrical model with the same atomic distance in each N.N. fitted with samples showed weak or no emissions.

In part 2, Nd-doped TiO_2 were prepared with Al co-doping and compared about their luminescence with local fine structure as a function of Al concentration. PL result showed luminescence in near-infrared wavelength region increased with increase of Al concentration. In contrast, luminescence dramatically quenched when Nd^{3+} ions were directly excited (without medditated by TiO_2). In addition, change in spectral shape and peak shift was observed for heavier co-doped samples. XAFS analysis revealed that distortion was caused for those samples with intense emissions/peak shifted by co-doping Al. Both Sm and Nd results are discussed in the same way of local structure effect.

In part 3, niobium (Nb) was co-doped into TiO_2:Sm to improve conductivity of sample for application to LEDs. Electrical properties of this sample with lateral (Ohmic and Schottky contacts were on the surface) and vertical (Schottky on the front, Ohmic on the back) structure are discussed whose informations help to improve a sample for measuring junction spectroscopy. Carrier density and built-in potential of TiO_2 and TiO_2:Sm were compared and Sm-doping results in more carriers than that without dopants. Finally, sensitiveness of TiO_2-based samples to environment in a cryostat is discussed.

ACKNOWLEDGEMENT

I would like to express my gratitude, which will never be enough, to following beautiful people:

My family, for their unlimited support, patience and love to bring me here from a bottom of the dark ocean. My sincerest gratitude goes to my mum who has been always there for me and shined my heart and future like the sun.

My family in the UK, my aunt Cecile, David, Heather-my mum in the UK, Allan, Benjamin, Stephen, Dominique and late David, whom love and kindness during my stay in Manchester and still go on. Neither legal nor genetical connection ties our relationships, but we are definitely a family.

Professor Xinwei Zhao, my supervisor, for his seemingly nonchalant, but very thoughtful support and guidance over 6 years. I could fly to everywhere and try everything I wanted to because of your encouragement and confidence on me.

Professor Shuji Komuro (Toyo University), my second supervisor and guardian, for his kindness and support both in professional and personal way. It was a true joy to have a cup of coffee in your office during an interval between the experiments.

Dr Iain Forbes Crowe (The University of Manchester), my supervisor in Manchester,

for his very powerful encouragement, support and making me confident. I really enjoyed discussing research and other things with you.

Dr Masashi Ishii (National Institute for Materials and Science), for his advice and making such a wonderful triangle between NIMS-UoM-TUS.

Dr Hiroaki Nitani (High Energy Accelerator Reserch Organization) for his technical support and advice for XAFS measurements and analysis for 6 years. You kindly listened to a presentation by an undergraduate student who was struggling with unsuitable beamline to her samples with no idea to resolve the problem.

Professor Matthew Halsall, Dr Vladimir Markevich and Professor Tony Peaker (The University of Manchester) for their guidance and time- I took very long time for my presentation almost every time at a group meeting!

Dr Simon Hammersley (The University of Manchester), whose knowledge, advice, support and kindness plus beautiful lasagna. It was a pleasure to meet you and have so many discussions not just only in Manchester, but at Manchester - Tokyo video meeting.

Dr Ian Hawkins and Mr Mal McGowan, Experimental Officers of The University of Manchester, for their technical support and small chats in the corridor.

Prfessor Mika Gamo and Professor Toru Katsumata (Toyo University), for their limitless encouragement, kindness and the lovely tea time at Prof Komuro's memorable office.

My colleagues of Zhao lab, some of them have already graduated, some will graduate with me and some will continue their journey of science in Zhao lab. It was really nice to work with you and passed through all those problems together.

My BFF, Ms Joyce Ann T. De Guzman (The University of Manchester) for her

love, friendship and giving me the positive energy- you have literally changed my life completely: I will never forget the importacne of self-love and being happy. It really was a nice memory to work with you in the lab and have lunch/chat at the pantry in Sackville Street Building.

My graditude also goes to all my friends and colleagues/staffs of the universities who helped me. And Elsevier, Wiley-VCH and The Brazilian Chemical Society for kindly giving me permissions to reprint figures in this thesis. Appologise not to write whose names due to keeping space for the main text.

List of publications

1. **A review on research progress in electrolytes for sodium-ion batteries (in Chinese)**

   X Xie, M Murayama, S Guan and X Zhao, Sci. Sin. Tech., Sci. China Press, **50**, 247–260, 2020.

2. ***Effect of Al co-doping on the luminescence properties of Nd^{3+}-doped TiO_2 thin films**

   M Murayama, K Yoda, S Komuro, I F Crowe and X Zhao, J. Lum., Elsevier, **216**, 116656, 2019.

3. ***Influence of Al on the local structure of Nd-doped TiO_2 thin films: A combined luminescence and X-ray absorption fine structure analysis**

   M Murayama, K Yoda, S Komuro, H Nitani, I F Crowe and X Zhao, Mater. Sci. & Eng. B, Elsevier, **246**, 49–52, 2019.

4. ***Photoluminescence enhancement and change in the second nearest neighbor distance of Sm-doped TiO_2 thin films**

   M Murayama, K Yoda, K Shiraishi, I F Crowe, S Komuro and X Zhao, Phys. Status Solidi B, John Wiley & Sons, **256**, 6, 1800522, 2019.

5. **Influence of anneal temperature in air on surface morphology and photoluminescence of ZnO thin films**

   S Guan, L Hao, M Murayama, X Xie, S Komuro and X Zhao, J. Phys.: Conf., IOP Publishing, **522**, 012004, 2019.

6. **Photoluminescence and Structural Analysis of Samarium Doped TiO_2 Thin Films and Their Applications to Visible LEDs**

   M Murayama, Y Yanagida, S Komuro and X Zhao, Opt. and Photonics J., Scientific Research Publishing, **8**, 5, 146-164, 2018

7. **Effect of doping concentration on Nd-related photoluminescence in TiO_2 with Al co-doping**

   M Murayama, K Yoda, K Shiraishi, S Guan, S Komuro and X Zhao, J. Phys.: Conf., IOP Publishing, **864**, 012068, 2017.

* Papers contributed to this thesis.

List of presentations

1. **Influence of annealing and co-doping on local fine structure of rare earth-doped semiconductors and their applications to opto-electronic devices**

   M Murayama, and X Zhao, Invited talk for the Graduate Seminar Class of the Physics Department, Mindanao State University-Iligan Institute of Technology, Iligan Philippines (online), 30 Sept. 2020.

2. **Electrical characterisation of Sm-, Nb-co-doped TiO_2 thin films**

   M Murayama, I F Crowe, S Hammersley, V P Markevich, M P Halsall, A R Peaker, K Sato, S Iwana, K Shiraishi, S Komuro, M Ishii and X Zhao, The 45th MNE (International Conference on Micro and Nano Engineering), Rhodes Greece, 25 Sept. 2019.

3. **Photoluminescence enhancement and change in the second nearest neighbour of Sm-doped TiO_2 thin films**

   M Murayama, K Yoda, K Shiraishi, S Komuro and X Zhao, The 34th ICPS (In-

ternational Conference on the Physics of Semiconductors), Montpellier France, 2 Aug. 2018.

4. **Photoluminescence and Structural Analysis of Samarium Doped TiO_2 Thin Films and their Applications to Visible LEDs**

   X Zhao, M Murayama, S Guan, K Yoda, K Shiraishi, T Ishii and S Komuro, NMDC 2017 (IEEE Nanotechnology Materials and Devices Conference), Singapore, 2 Oct. 2017.

5. **Change in local fine structure in rare earth doped TiO_2 thin films and its luminescence properties optimised by annealing and co-doping**

   M Murayama, K Yoda, S Komuro and X Zhao, Invited talk at Photon Science Institute, The University of Manchester, Manchester United Kingdom, 28 Sept. 2017.

6. **Effect of cluster dispersion on co-doping Al in Nd^{3+}-doped TiO_2 thin films with luminescence properties**

   M Murayama, K Yoda, S Komuro and X Zhao, The 43rd MNE (International Conference on Micro and Nano Engineering), Braga Portugal, 19 Sept. 2017.

7. **Effect of doping concentration on Nd-related photoluminescence in TiO_2 with Al co-doping**

M Murayama, Y Yanagida, S Komuro and X Zhao, The 33rd ICPS (International Conference on the Physics of Semiconductors), Beijing China, 2 Aug. 2016.

Chapter 1

Introduction

1.1 Background

It is very essential to produce energy to the most of developed countries, and it is also crucial for developing countries for their further development. At the same time, *how to use and/or how efficiently to use energy*- as you manage your life depending on your bank account, is also very important. There are so many inventions due to this reason such as computers, smartphones, lighting equipment, solar panels etc, and their efficiencies have been improved by scientists. They made our lives more convenient and saved our limited money and energy, and most importantly, we couldn't have a benefit of them if there were no semiconductors in the world. Because they are hearts of most of our electronic devices and equipment for our lives. This means our lives have been developed with semiconductors.

Nowadays, LEDs, so-called the 5th generation of our lighting equipment, are widely

used in everywhere, not just for general illuminations, but also for medical usages, communications and backlights of display. Gallium (Ga)-based (III-V compounds including Ga such as GaN and GaAs) LEDs are widely used because it is an optimal material for very efficient applications. Nevertheless, it is unclear to keep the amount of importing Ga as much as companies and researchers demand because of the political issues between exporting and importing countries [1]. Hypothetically, it can be replaced by other wide-band gap semiconductors. Thus, the purpose of this thesis is understanding the nature of rare earth with the combination of oxide semiconductors which is abundant in the earth to induce its luminescence efficiently as much as we can.

1.2 What is rare earth?

1.2.1 Introduction

The rare earth materials (often characterised by different names such as rare earth elements, rare earth metals or rare earth oxides) are members of Group IIIB in the periodic table. They seem like actors of "supporting role" as you can see in Fig. 1.1. However, this Group IIIB- the scandium (Sc), yttrium (Y) and lanthanoids, from lanthanum (La) to lutetium (Lu) (21, 39 and 57 - 71 in atomic numbers) is the biggest group in the elements. The most remarkable thing of rare earths is that their chemical and physical properties are very similar to each other. It is therefore very easy to try some idea and compare it with each other [2].

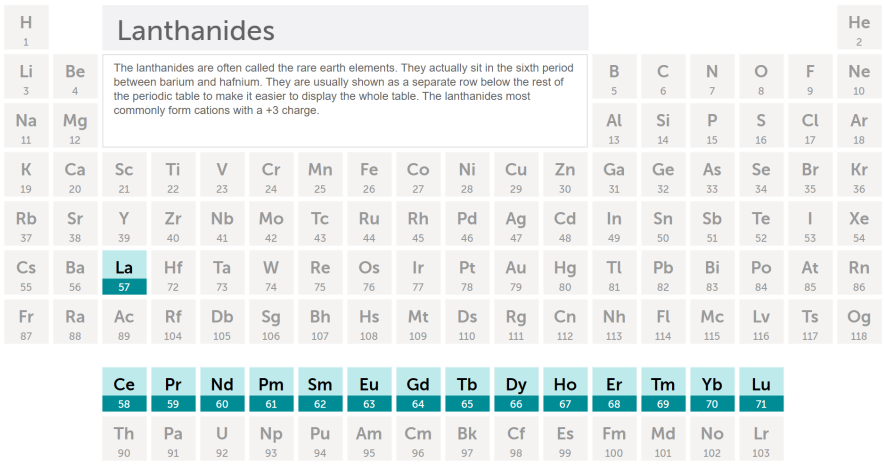

Figure 1.1: Lanthanides in a periodic table. Image from Royal Society of Chemistry website: https://www.rsc.org/periodic-table/.

1.2.2 History of rare earth materials

Rare earth materials relatively sound unfamiliar to the most of the people, however they are very beneficial in our lives in terms of improving performance of commercial, industrial, medical, military and space applications [3]. Here, we would like to look back on the history of rare earth materials for the readers who have just started their research using rare earths or just got interested. The first question will be definitely "Are rare earth materials so rare?". The answer is "No".

There is a huge contribution of scientists in Sweden, Norway and other European countries who put a lot of efforts on mining operations to the discovery of rare earth materials. An encounter with rare earth materials for human beings was finding a rare earth mineral by Carl Axel Arrhenius in a quarry in Ytterby village in Sweden in 1792. This black, heavy mineral was actually a rare earth compound consisting of cerium, yttrium, iron, silicon and other elements, which was named gadolinite in 1800.

The Finnish mineralogist/chemist Gadolin received this compound and he successfully first isolated rare earth oxide "yttrium (Y)" from this compound. It had been 30 years after this discovery to find the other rare earth elements, and took over 150 years for identification and discovery of all 17 elements. This is the reason why you can find some North European names in rare each elements: Some of them are named based on locations where they were found, and some are after the scientists who contributed to their discovery or to understanding their chemical properties. One significant fact is that their names do not agree with their natures. Rare earth elements are abundant in the earth except promethium (Pm). Let us show you one example: cerium (Ce), 0.006% in the earth's crust, is as abundant as copper (Cu), 0.0068%, which is in somewhere from the second half to the beginning (around 25th) in abundance list [3]. However, it is often difficult to separate rare earth compounds into individual element so that they are rare in that meaning. Rare earth elements are lithophile elements, therefore they never present in pure, but oxides. Main rare earth contained materials are phosphate minerals, ion-adsorbing clays, magmatic-related deposits (carbonatites) and placer deposits (marine and beach sands). Carbonatites and ion-adsorbing clays are two main deposits to obtain rare earths for commercial purpose, but rare earth elements are basically by-products of other resources such as titanium (Ti), iron (Fe), uranium (U), tin (Sn), and so on. The two most famous mines of carbonatites are Mountain Pass Mine, California, USA, which was the world' greatest concentration of rare earth elements in 1949, and Baiyun Obo Mine, Inner Mongolia, China, which has 83% of the Chinese deposit concentrations. Some of carbonatites such as perovskites and monazites are rare earth-replaced minerals (Ca replaced by rare earths in $CaTiO_3$

and Ce in $Ce(PO_4)$). Monazites also can be found in marine and beach sand. They are mined in Florida and Idaho, USA, Australia, India or Brazil. Mainly, ion-adsorbing or rare earth contained clays are occurred in south China. Japanese scientists reported the Pacific Ocean has a potential for rare earth element resources in 2011. So far, there is no physical or mineral shortage for rare earth elements. However, we need to solve some issues such as technological, political and possibly economic problems.

1.2.3 Physical and chemical properties of rare earth elements

Transition metals- *d*-block metals and *f*-block metals

Physical and chemical properties of rare earth elements and their applications are shown in this section. Rare earth elements with smaller atomic numbers from La to gadolinium (Gd) and Sc are classified as light rare earth elements (57 - 64 and 21 in atomic numbers), and others with bigger atomic numbers from terbium (Tb) to Lu and Y (65 - 71 and 39 in atomic numbers) are referred to as heavy rare earth elements. From samarium (Sm) to holmium (Ho) (62 - 67 in atomic numbers) are occasionally called the medium or middle rare earth elements [4]. The heavy rare earth elements are rarer than the light rare earth elements. They can occur only in ion-adsorbing clays mentioned in the previous section, and only found in south China. The electron configurations are considered for defining the boundaries between the light/heavy rare earth elements due to the remarkable stability of the electron configurations in the $4f$ orbital such as unoccupied (f^0), half occupied (f^7) and fully occupied (f^{14}) the $4f$ orbital. Chemical behaviour and ionic radius of Y is very similar to Ho so that Y is attributed to the heavy rare earth elements.

Rare earth elements belong to transition metals/elements (with unfilled inner-shells,) [5]. Generally, in the elements, electrons start filling low energy orbitals first, in other words, closer to the nucleus. This means that you can see the consistency between distance from the nucleus and the energy. However, the transition metals such as *d*-block (from the group 3 to 12 metals although the group 12 metals are occasionally not included) and *f*-block (lanthanoids and actinoids, from actinium (Ac, 89) to einsteinium (Es, 99)) [6] behave totally in different way. In *f*-block, the 4 *f* orbitals are not filled by electrons until after 6*s* is occupied. In other words, outer appearance of lanthanoids remain the same even though the atomic numbers and numbers of electron fill the 4*f* orbitals are different- the reason being that the chemical properties of rare earth elements are almost the same, but physical properties are not. This means that electrons in 4*f* orbital, which is responsible for excitation and transition, is gently shielded by outer shells of 5*s* and the 5*p* orbitals. This "shield" prevents to be affected luminescent properties (i.e. emission wavelength and spectral width) by external potentials such as temperatures and crystal field. Usually the optical properties of the given luminescent centre such as doped phosphors in different host materials/lattices are different (different shapes of emission spectra, etc) due to influence by crystal field of host material. In addition, there is no availability of covalent bonding because the 4*f* orbitals are deep inside of the outside shells and deep-lying buried. Probability of finding an electron in the 4*f* orbital is much higher than in the *d* orbital of *d*-block due to shorter distance from the nucleus. Also, *f*-block metals are similar to each other much more than the *d*-block metals. Usually, trivalent lanthanoides are the most stable in solids. The trivalent rare earth elements occur due to removing two electrons from the 6*s* orbitals and one

electron from the 4*f* orbitals (sometimes from 5*d* intestead of 4*f*). Interesting and/or useful special properties of rare earths such as magnetic, chemical, electro-optical and nuclear properties used for many applications are mainly this the 4*f* orbital-related.
Researches on rare earth elements made progress around 1960 as a part of the world-wide major atomic energy programme of 1950', which was carried out first in the United States and England, then other European countries followed after them. This programme was established since the discovery of nuclear fission in 1939, which aimed for substantial electric power generations by nuclear technology. Rare earth elements are not dangerous to the environment due to their chemical property: they are physiologically inert so that they are considered to be suitable for polishing applications. Rare earth elements, especially, rare earth oxides play an important role for the extensive chemical reactions on the surface of the glass to remove the material.

1.2.4 Physical property of Rare Earth

If the atomic number increases, the number of electrons should be increased so that ionic radius would be also increased to fill electrons in its orbitals. Generally, this is how to expand the ionic radius of the elements, however there are some exceptions such as lanthanoids, actinoids and transition metals. There is one similarity between the two: both of them have the incomplete *f* orbital, and that is buried inside of the other outer shells. Note that the 4*f* orbital of actinoids is closer to the outermost shell than lanthanoids, which means that 4*f* electrons are expanded enough to correspond to the chemical bonding. This is why there are various ionisation states in actinoids. The

size of atomic and ionic radius of lanthanoids decreases with increasing atomic number. This is called the lanthanoid contraction. In common, the contraction of ionic radius is widely explained as the result of increase of nuclear charge (increase of atomic number), and the increasing $4f$ electrons cannot keep this charge within themselves so that the nucleus attracts outer atomic orbitals closer [7, 8]. The lanthanoide contraction has some regularities of decrease of ionic radius with increasing atomic number, however the actinoides do not regularly contract. There are two reasons why it was difficult to separate rare earth minerals or compounds into each individual element: the first reason is very similar chemical properties of rare earth elements due to the electron configuration, the incomplete $4f$-inner shell (for all trivalent rare earth elements, the outermost electron configuration is the same as s^2p^6). Secondly, rare earth elements have very similar size of the ionic radius to each other. The ionic radius of 16 rare earth elements are in a range of 0.01 nm except Sc so that it was very difficult to identify individual rare earth element.

We need to consider the orbital angular momentum of $4f$ electrons for further discussions about the $4f$ orbital-related properties of rare earth elements such as electro-optical and magnetic properties. Describing these momenta is difficult and complex though we introduce an abbreviated way of description here [9]. In quantum mechanics, we describe the angular momentum operator as $\boldsymbol{l}$ and the spin operator as $\boldsymbol{s}$. Now, we define $\boldsymbol{l}_i$ as the angular momentum of a $4f$ electron and $\boldsymbol{s}$ as the spin operator of a $4f$ electron. There are three types of interactions can occur in atom system:

- spin-spin coupling
- orbit-orbit coupling
- spin-orbit coupling.

In the LS approximation of rare earth, it is assumed as follows [10]:

spin-spin coupling>orbit-orbit coupling>spin-orbit coupling.

The total orbital angular momentum operator of all the electron in the 4*f* orbital can be defined as

$$\boldsymbol{L} = \boldsymbol{\Sigma l_i}. \tag{1.2.1}$$

$\boldsymbol{L}$ takes values 0, 1, 2, 3,..., which is indicated by the notation of *S*(when the value is 0), *P (1), D (2), F (3), G (4), ...* Those notations are derived from the orbitals (*s, p, d, f, g,* ...). Also for the total spin operator of all the electron in the 4*f* orbital:

$$\boldsymbol{S} = \boldsymbol{\Sigma s_i}, \tag{1.2.2}$$

which takes the values of 0, 1/2, 1, 3/2, ... If the spin-orbit coupling can be neglected, we can handle *L* and *S* independently. Note that the number $2S + 1$ is called the multiplicity of the state or of the term. This number characterises the possible number of the states of the total spin angular momentum, and it is written on the upper left of the letter.

Finally, the total angular momentum operator of the atom is described as:

$$\boldsymbol{J} = \boldsymbol{L} + \boldsymbol{S}, \tag{1.2.3}$$

which takes the values of 0, 1/2, 1, 3/2, ... This time, this number is written on the lower right of the letter. This approximation, the Russel-Sanders coupling or the LS coupling describes the electron configurations such as the ground states and the excited states. When the ground states are written by LS coupling, the ground terms are deduced by Hund's Rules, which consist of three rules:

1. The ground term has the maximum multiplicity (***S***), which corresponds to the lowest energy. In other words, all the electron spins need to be parallel as much as they can for making the most stable electronic configuration.

2. If there is more than 1 term with the maximum multiplicity, the ground term has to have the largest value of ***L***.

3. *J*, the value of the total angular momentum is equal to (|***L-S***|) or (|***L+S***|).

The third Hund rule is consequent the sign of the spin-orbit interaction. The spin-orbit coupling was ignored to explain the LS approximation, however this would need to be taken into account for considering heavy atoms including rare earth elements. The spin-orbit coupling is the interaction between spin and orbital momenta, therefore each

momentum is not independent. This occur by the force, which tries to make $\boldsymbol{l}_i$ and $\boldsymbol{s}_s$ different directions as much as possible. If the spin-orbit interaction is taken into acount, the LS coupling can be described in two different ways as follows:

1. If the incomplete shell is occupied less than half full, then

$$\boldsymbol{J} = \boldsymbol{L} - \boldsymbol{S}. \tag{1.2.4}$$

2. If the incomplete shell is occupied more than half full or the shell is fully occupied, then

$$\boldsymbol{J} = \boldsymbol{L} + \boldsymbol{S}. \tag{1.2.5}$$

In the case of the 4*f* orbital, the first equation is applied to La - Eu (number(s) of electrons in the 4*f* orbital: 0 - 6 over 14), and the second applied to Gd - Lu (7 - 14 over 14).

Even though spin-orbit coupling has the smallest influence in LS approximation, it effects on 4*f* configurations [19]. Firstly, energy levels are affected by the central field (H_0) in free ions' H_0 separates the different configurations (5*p*, 4*f*, 5*d*, etc) in 10^5 cm^{-1} in energy. The degeneracy of 4*f* configurations is kept because the H_0 term has a purely radial contribution. However, the interelectronic repulsion interaction (H_{e-e}) removes the degeneracy of 4*f* configurations resulting $^{(2S+1)}$L levels separated by an

energy about 10^4 cm^{-1}. Each levels is affected by the spin-orbit coupling term (H_{SO} removing the degeneracy of $^{(2S+1)}$L levels. It results a separation of 10^3 cm^{-1} within the $^{(2S+1)}L_J$ levels. Diminution of the symmetry from a spherical field (free ion)to a non-spherical crystal field (V_{CF}) induces the loss of degeneracy of $^{(2S+1)}L_J$ as d electrons. Shtark split due to the crystal field symmetry is the energy separation of 10^2 cm^{-1}. Detailed information of 4*f* configurations of used rare earth with removed degeneracy the perturbations are shown in Section 1.2.6 and 1.2.7, Chapter 1.

According to the Pauli principle (Pauli exclusion principle), a state of two or more identical fermions cannot occupy the same quantum state describes as following so-called Slater determinant:

$$\psi_a = \frac{1}{\sqrt{N!}} \begin{vmatrix} \psi_{n1}(1) & \psi_{n1}(2) & \cdots & \psi_{n1}(N) \\ \psi_{n2}(1) & \psi_{n2}(2) & \cdots & \psi_{n2}(N) \\ \cdots & \cdots & & \cdots \\ \psi_{nN}(1) & \psi_{nN}(2) & \cdots & \psi_{nN}(N) \end{vmatrix}. \tag{1.2.6}$$

This is the reason why two or more particles cannot exist in the same state in a system of identical fermions [9].

1.2.5 Rare earth as a phosphor

Rare earth is widely used as luminescent centre (activator/phosphor) for application to LEDs, Laser Diodes (LDs) and waveguide amplifiers [11, 12, 13, 14, 15]. However, there is some barriers to breakthrough for obtaining their intense, sharp and unique emissions: typically, the absorption cross-section of rare earth elements is very small. The 4*f*-*f* transitions of electric-dipole transition in free rare earth ions is generally forbidden and very weak limited transitions (oscillator strength, $f < 10^{-6}$) consisted of allowed magnetic-dipole and electric quadrupole transitions. In solid, electric-dipole transition can be partially allowed because the 4*f* wavefunction is affected by the crystal filed. In this section, we would like to discuss about spectral strength of rare earth and its selection rules [13, 14, 16, 17, 19]. Generally, luminescent intensity is described by using the primary attenuation:

$$I(t) = -\frac{dn}{dt} = \frac{n}{\tau}, \;\; n = n_0 \exp(-\frac{t}{\tau}), \tag{1.2.7}$$

where *n* is concentration of the phosphor, τ is decay time and *t* is time, therefore

$$I(t) = (\frac{n_0}{\tau})\exp(-\frac{t}{\tau}). \tag{1.2.8}$$

The optical transition probability between the ground state ($v = 0$) and the vibration level in an excited state ($v = v'$) is proportional to:

$$< e|r|g >< \chi_{\nu'}|\chi_0 >, \tag{1.2.9}$$

where e and g refer the electronic wavefunctions of the excited state and the ground state, r is the electric-dipole operator driving the transition and χ are the vibrational wavefunctions. For consideration of the whole absorption band, one has to sum over v'.

1.2.6 Neodymium, 60

Neodymium (Nd) is used with various materials (glasses, substate crystals, alloys) in many kinds of applications such as laser diodes (Nd:YAG) and permanent magnets. Nd oxidized in the +2, +3 and +4 oxidation states. Trivalent Nd (Nd^{3+}) is mainly used for luminescence with IR wavelength emissions. The ground state of Nd^{3+} is $^4I_{9/2}$ and the 4*f* orbital which is responsible for the transition is filled by 3 electrons ($4f^3$). The electronic configurations of Nd^{3+} is [Xe] $4f^3$ ([Xe]: $1s^2 2s^2 3p^6 3s^2 3p^6 3d^{10} 4s^2 4p^6 4d^{10} 5s^2 5p^6$). 4*f*-5*d* emission for Nd^{3+} can be also observed under certain conditions. Haas et al reported the 4*f*-5*d* emissions of LaF_3:Nd^{3+} crystal characterised by X-ray excited luminescence [18]. The 4*f*-5*d* peaks are observed at 173, 216, 245 nm, whilst the 4*f*-4*f* lines are located at 354, 382, 414 and 448 nm. The lowest energy absorption band of 5*d* is located at 159 nm. The decay time is only 6 nsec because of the $\tau \sim \lambda^2$ relation. Figure 1.2 (a) illustrates a schematic of the $4f^3$ configuration of Nd^{3+} with the removed degeneracy by perturbation. Schematic diagram of typical transitions of Nd^{3+} with energy transfer from anatase-phase TiO_2 is shown in Fig. 1.2 (b).

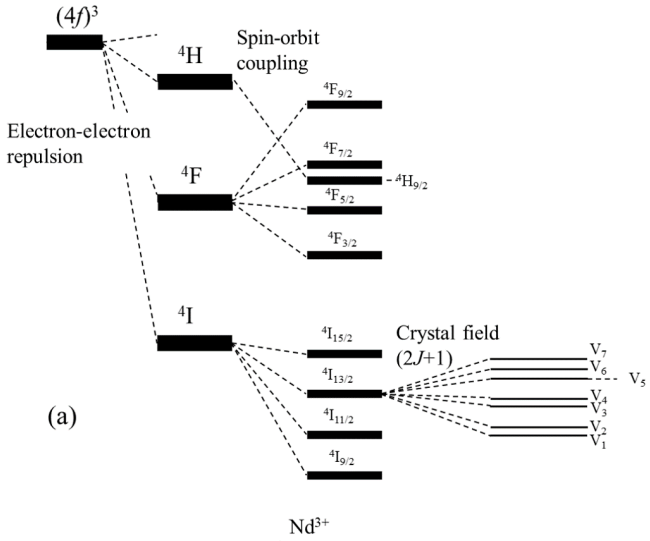

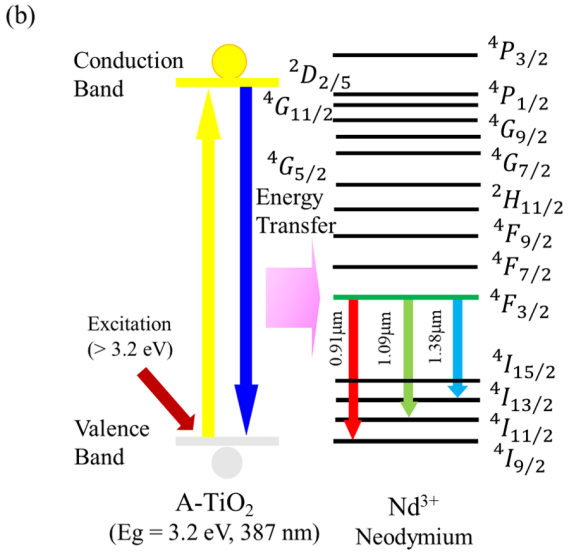

Figure 1.2: Schematic diagram of (a) $4f^3$ configuration states of Nd^{3+} (b) typical Nd^{3+} transitions with energy transfer from anatase-phase TiO_2.

1.2.7 Samarium, 62

Divalent and trivalent Sm (Sm^{2+}, Sm^{3+}) are used as a phosphor. For the ground state of Sm^{3+} is ${}^6H_{5/2}$ and the 4*f* orbital which is responsible for the transition is filled by 5 electrons ($4f^5$). The electronic configurations of Sm^{3+} is [Xe] $4f^5$. Schematic of the $4f^5$ configuration of Sm^{3+} with the removed degeneracy by perturbation and a shematic diagram of transitions of Sm^{3+} with energy transfer from anatase-phase TiO_2 is shown in Figs. 1.3 (a) and (b). We show energy levels of the $4f^n$ configurations of trivalent rare earth elements in Fig. 1.4 [19] for conclusion of this section.

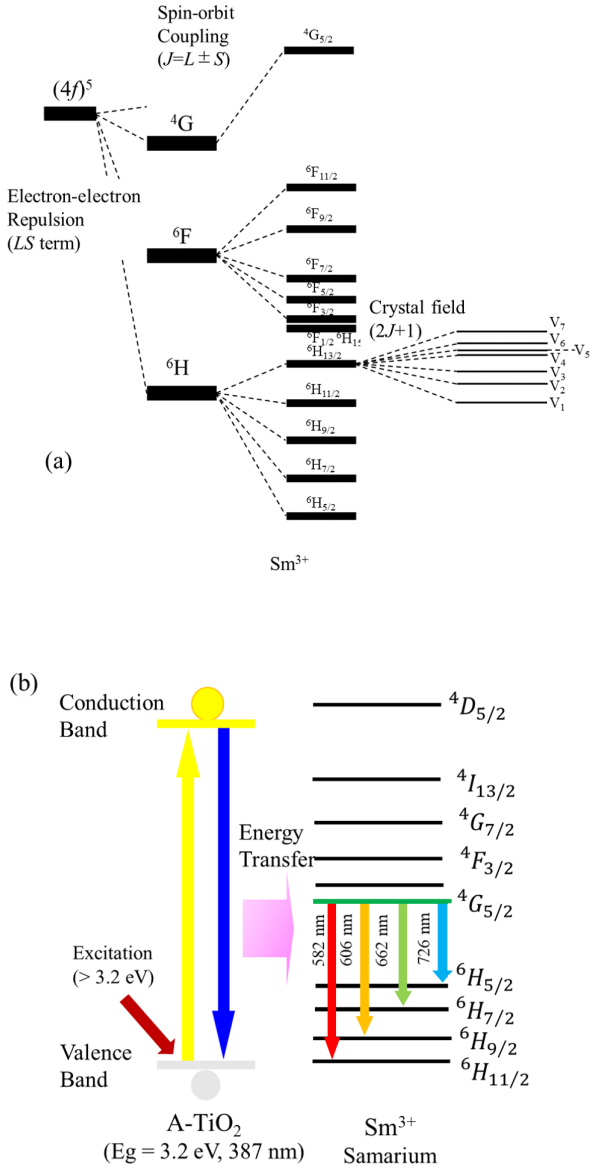

Figure 1.3: Schematic diagram of (a) $4f^5$ configuration states of Sm^{3+} (b) typical Sm^{3+} transitions with energy transfer from anatase-phase TiO_2.

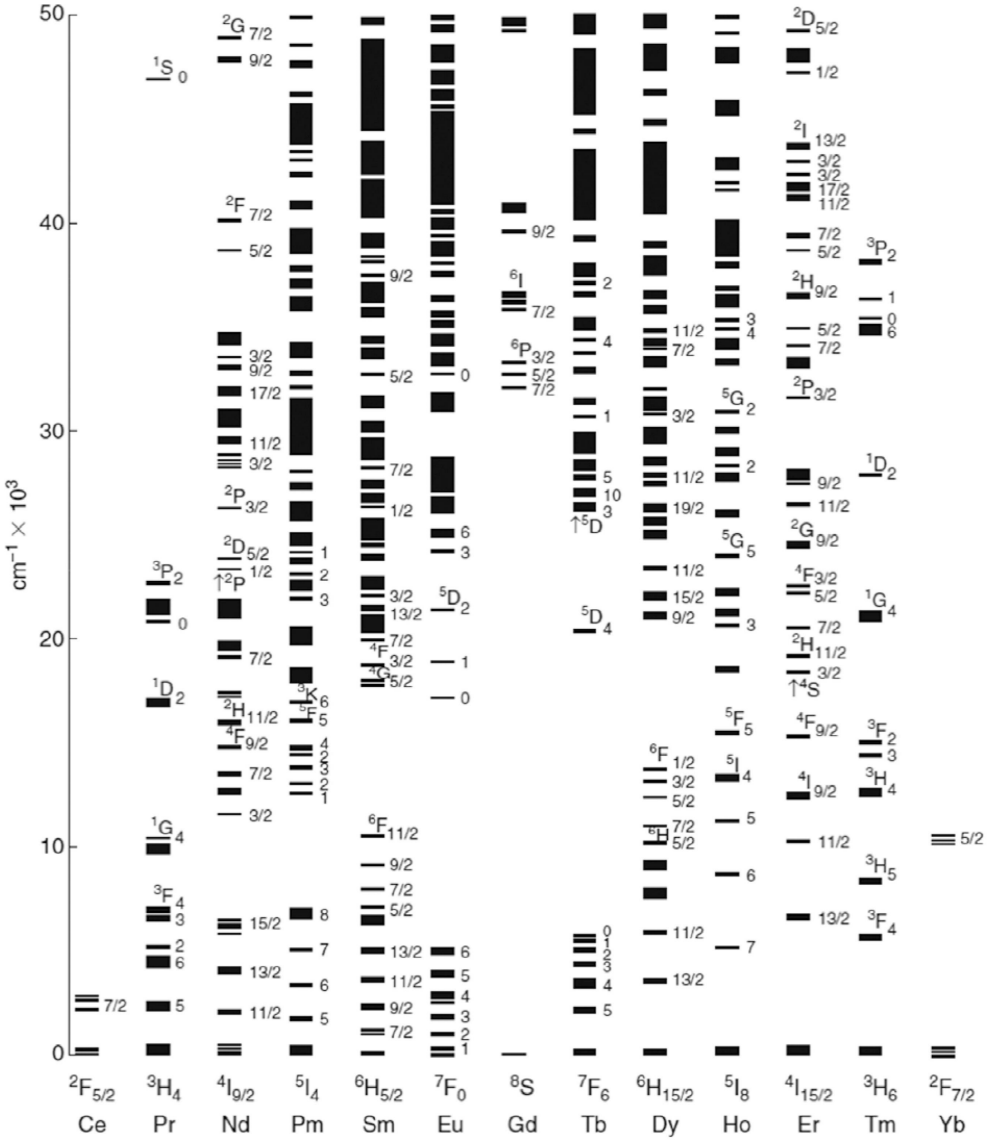

Figure 1.4: Energy levels of the $4f^n$ configurations of trivalent rare earth elements. Reprinted with permission from [19], copyright reserved by The Brazilian Chemical Society, 2015.

1.3 TiO_2

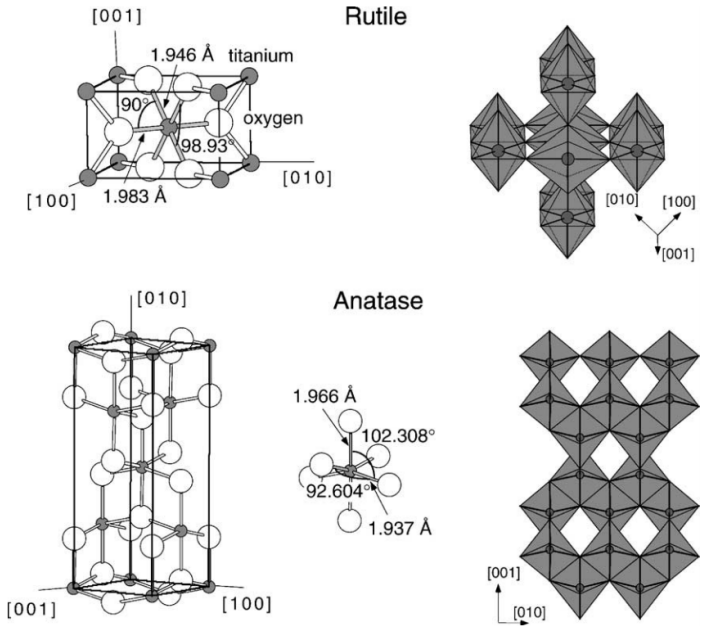

Figure 1.5: Unit cell of anatase- and rutile-TiO_2 Reprinted with permission from [20], copyright reserved by Elsevier, 2003.

As discussed in Section 1.2.5, Chapter 1, rare earth needs to be doped into a host material because rare earth needs the effect of the crystal field on its wavefunction of the 4*f* orbital. To the best of our knowledge, a wide band-gap semiconductor is a better candidate for a host material, especially, rare earth has good chemistry with oxides: rare earth generally exists as rare earth oxides. In this thesis, we selected titanium oxide/titania (TiO_2) as the host material for a rare earth phosphor. TiO_2 have been widely studied over the years because of its interesting general properties in a various range of fields namely, from commercial, environmental and energetical view points. For commercial applications, TiO_2 has been used including as paints, inks

(its whitish colour), water and air purification, self-cleaning surfaces, sensor devices (its environmental properties), solar cells, photocatalysis and ultra-violet absorption in sunscreens and cosmetic products (its energetical properties) [21, 22, 23, 24, 25, 26]. TiO_2 is an inorganic compound with three crystalline phases (band-gap energy/crystal system/space groups): anatase (3.2 eV/ Tetragonal/ $I4_1$), rutile (3.0 eV/ Tetragonal/ $P4_2$) and brookite (3.26 eV/ Orthorhombic/ Pbca). Figure 1.5 shows the unit cell of (a) anatase- and (b) rutile-TiO_2 [20]. For either case, the valence band is mainly made up of O 2*p* states with some Ti 3*d* and Ti 4*sp* character combined with the empty Ti 3*d*/4*sp* conduction-band states. Heating TiO_2 easily to let lose oxygen from the surface and bulk at at temperature around 500 - 700°. Generally, rutile-TiO_2 with the particle size larger than 14 nm is more stable phase than that for anatase under ambient conditions. Anatase at small particle sizes is the most stable in three TiO_2 phases [27]. The phase transition efficiency decreases with time, and the crystalline growth rate increases by the phase transition of anatase-to-rutile [28]. The anatase-to-rutile phase transition is caused by annealing. This transform kinetics is determined by several factors such as growth rate, temperature and atmosphere. As other *n*-type semiconductors such as ZnO, TiO_2 tends to become the *n*-type semiconductor with the presence of donor-like oxygen vacancies whose states are close to the Fermi level [23]. For anatase, (101) is the most stable surface and the easiest to have surface oxygen-defects with the higher photocatalytic activity of anatase over rutile [29]. Literatures report property of electrical conductivity for (001)-oriented anatase can be found and its surface is difficult to have oxygen-vacancies.

1.4 Semiconductors and defects

Defects have a substantial impact in semiconductors especially in terms of applications to device for everyday use. Since there are always defects in semiconductors which give a huge effect on properties of semiconductors: sometimes it would dramatically improve device functions, and sometimes it can work opposite. They are intentionally introduced by impurities such as dopant atoms (shallow-level impurities) to change the type of semiconductors or carrier concentrations, or recombination centres (deep-level impurities) to reduce the device lifetime [30]. Also, defects are unintentionally introduced during fabrication or device processing (i.e. atmosphere in a chamber during crystal growth, annealing conditions). Understanding carrier generation, recombination and trapping process is very important for discussing semiconductors or devices because these processes would determine efficiency of devices. There are several ways to create carriers such as thermal excitation, however the optical excitation is described. For producing carriers, a photon needs to have the same as or greater energy than the difference of the energy between the bottom of the conduction band and the top of the valence band, i.e. bandgap in direct bandgap semiconductors. In indirect bandgap semiconductors, thing is more complex due to the different electron momentum of electrons and holes in the conduction band and valence band, therefore wave vector is not conserved after excitation. This difference means it is not necessary to be “the minimum conduction band” and “the maximum valence band”. After excitation, a hole/an electron is created in the valence band/the conduction band, which emits luminescence and/or thermal perturbation after recombination process.

1.5 Purpose of this study and thesis outline

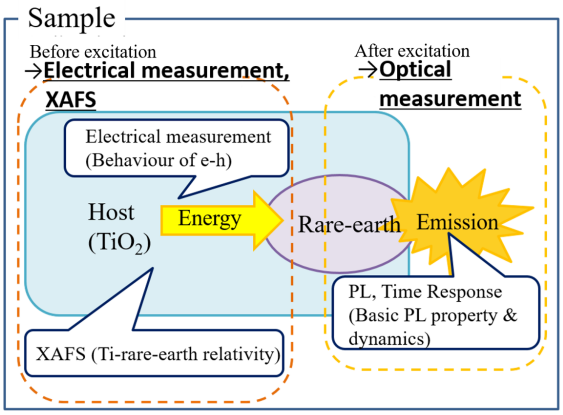

Figure 1.6: Schematic of this study.

Main theme and motivation throughout this thesis are understanding rare earth emissions including their mechanism such as factors of enhancing their emissions and energy transfer process. This study is strongly motivated by future applications of rare earth-doped semiconductors, especially TiO_2 to practical LEDs. One of outstanding points of this work is that it focuses on not just only the process of "excitation of rare earth to emissions" (after excitation), but also the process of "excitation of a host material to excitation of rare earth ions"(before excitation) as shown in Fig. 1.6, . This study was well planned, and all measurements shown in this work were carried out based on understanding each process. Energy transfer is a process considered as follows, however it is not experimentally well understood:

1. Excite a host material with excitation source (i.e. laser) higher than a band gap energy of a host material.

2. Excited electrons and holes recombine at an *intermediate state* in the host material.

3. Recombination energy transfers to rare earth ions to excite them.

4. Rare earth ions exhibit emissions.

There is a huge energy difference between excitation energy of a host material (semiconductors, 3.2 eV for anatase-TiO_2) and a luminescent centre (rare earth, visible wavelength region). This suggests an existence of intermediate state in a host material which *catches* excited electrons and holes and *releases* recombination energy. The intermediate state can be a defect state below the conduction band of a host material caused by a rare earth dopant or doping rare earth. This study shows results of PL measurements (after excitation), XAFS measurement (before excitation) and electrical measurements (before excitation) for understanding how PL intensity can be enhanced and how energy transfer from a host material to rare earth.

In Chapter 3 and 4, a connection between luminescent properties and local fine structure of rare earth is discussed. Authors discuss *from the viewpoint of rare earth* especially in these two chapters. Possibly most of the readers imagine the crystal structure of a host material or think from the viewpoint of the outside of the lattice when local structure of luminescent centres is discussed. However, although there is not much effect on the crystal structure of a host material, a co-ordination around rare earth (very local and limited as the word describes) is strongly affected by the outside influence such as annealing (Chapter 3) and co-doping (Chapter 4). These two different approaches were done for the enhancement of rare earth emissions. Change in local fine structure of rare earth is compared between two different influences (annealing

and Al co-doping). Estimating this *change* in co-ordination around the luminescent centres is very crucial for understanding rare earth emissions and further discussions of energy transfer from a host material to the luminescent centres. Local fine structure of rare earth is estimated by XAFS analysis. It was already reported that the distortion of local fine structure, especially the first nearest neighbour, of rare earth is one of the most important factors for the enhancement of the rare earth emissions. The second outstanding point of this study is that quantitative and highly accurate estimation of local fine structure of the luminescent centres is successfully done (please find discussions about an accuracy of XAFS measurement and analysis in Section 2.3.1, Chapter 2). In addition, this is the first time ever to be done with quantitative, metrical and accurate estimations of the second nearest neighbour of rare earth ions. We can expect that this expands discussions of energy transfer. Energy transfer is an excitation process of rare earth via the host material: distortion of the second nearest neiboughr of rare earth is possibly a better environment for enhancing energy transfer. Because the intermediate state can exist near the second nearest neighbour (Ti) of rare earth and distortion (or optimal bond length) introduces better potential valleys for energy transfer.

In Chapter 5, in contrast, electrical characteristics of rare earth-doped TiO_2 are discussed. The third outstanding point of this thesis is that doped rare earth enhancing conductivity of TiO_2 is confirmed. In addition, we experimentally revealed that rare earth provides donors to a host material. These results directly support understanding energy transfer and application to opto-electronic devices.

A brief summary of each chapter is as follows:

Chapter 2 provides the general experimental techniques used throughout this thesis.

Namely, sample fabrication includes laser ablation and annealing, some of the measurements use X-rays and photoluminescence.

Chapter 3 describes the optical and local fine structural properties of Sm-doped anatase- and rutile-phase TiO_2 thin films. This chapter focuses on the influence of annealing temperature on luminescence and the change in local fine structure.

Chapter 4 examines the sensitising effect of Al-co-doping on luminescence property of Nd-doped TiO_2 and its local fine structure.

Chapter 3 and 4 are *twins* which focus on the connection between rare earth luminescence and local fine structure with different approaches to emission enhancement.

Chapter 5 provides a brief summary of electrical properties of TiO_2, TiO_2:Sm and TiO_2:Sm:Nb for further study of estimation of rare earth-related defect levels using junction spectroscopies.

Finally, in Chapter 6, we conclude throughout thesis and give some future prospects.

Chapter 2

General experimental techniques

2.1 Sample preparation

2.1.1 Laser ablation

For all of the samples, rare earths doped TiO_2 thin films on substrates, described in this study were prepared using laser ablation (i.e. pulsed laser deposition, PLD). Figure 2.1 illustrates a schematic of standard laser ablation system. Laser ablation is one of the physical vapor deposition techniques such as evaporation, sputtering and ion-plating. It allows from room temperature to couple of hundreds degrees deposition (by substrate heating) in a vacuum chamber with a wide range of targets. A typical system for laser ablation is relatively simple: a laser source and a chamber, which is properly vacuumed

with a target and substrate set on holder. A high intensity laser source is focused onto a target, then remove few layers from the target surface, which form an ablation plume. Thin film is fabricated on the substrate when plume reaches to the substrate. Many types of pulsed lasers are used for ablation such as Ruby lasers, Nd:YAG and excimer lasers [31, 32, 33]. Commonly, a laser source with wavelength of approximately 200 nm is used for ablation. Laser intensity can be determined by pulse energy (related to wavelength), focal spot area and pulse duration (from milliseconds to femtoseconds), which is crucial for a deposition in terms of laser-material interactional as follows:

$$\mathrm{Laserintensity(W/cm^2)} = \mathrm{peakpower(W)/focalspotarea(cm^2)}, \tag{2.1.1}$$

$$\mathrm{Fluence(J/cm^2)} = \mathrm{laserpulseenergy(J)/focalspotarea(cm^2)}, \tag{2.1.2}$$

while the peak power is

$$\mathrm{Peakpower(W)} = \mathrm{pulseenergy(J)/pulseduration(sec)}. \tag{2.1.3}$$

The longer laser pulse duration means less irradiance. For instance, if the duration is microseconds, irradiance would be approximately 10^6 W/cm^2, whereas the irradiation of nano-seconds duration is 10^9 W/cm^2 [31].

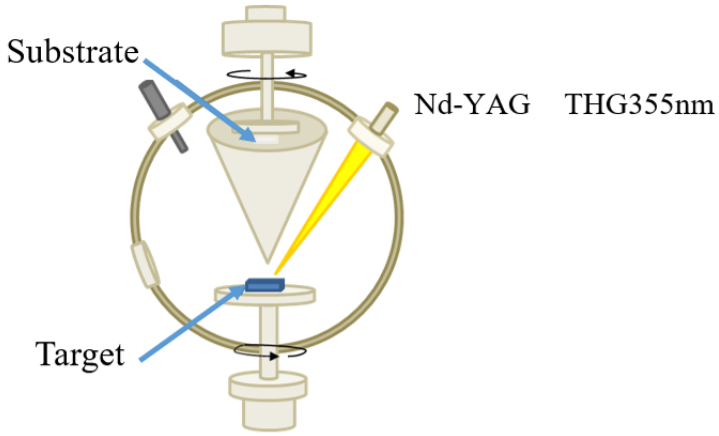

Figure 2.1: Schematic diagram of a laser ablation system.

2.1.2 Annealing

Annealing is a thermal treatment which alters physical and/or chemical properties of materials. Especially, it is done after sample fabrications to make fabricated samples soft with some side effects. As-prepared samples (or rather say, crystalline materials) have obtained stored free energy during fabrication such as dislocations, vacancies and strains, which is thermodynamically unstable [34]. Annealing can be explained or called *deformation* because annealing changes crystallinity, removes or sometimes adds dislocations, defects and strains, and these effects are undergone depending on annealing temperature. To remove these defects, materials need to be heated at a high temperature, otherwise these instabilities remain after deformation. Most of the fabrication techniques generally remove a target surface of materials (compounds), and during this process, the source of removing materials/deposition cut bonding of the removed materials. Annealing has the following effects in crystal growth of semiconductors:

- Recovery
- Recrystallisation
- Grain growth
- Doping/inducing defect sites.

During recovery, annealing releases the energy from point defects, and also, rearranges dislocations. This recovery process is important for semiconductors, which are used for electro applications. Electrical resistivity is reduced due to the release of the energy. However, this change affect in microstructure during recovery process is not observable under a light microscope. Dislocations are also rearranged into lower energy configurations. In addition, residual strains are reduced due to conversion of elastic strains to plastic strains by creep if enough creep occurs. Annealing at higher temperature facilitates faster stress relief.

Replacement of grains by new grains with fewer dislocations occurs in recrystallisation process. The fraction of recrystallisatising materials, f can be described using Avrami expression:

$$f = 1 - \exp(-bt), \tag{2.1.4}$$

where b is a constant and t is time. Note that this approximation can be used at any annealing temperature. Certainly, annealing temperature facilitates crystal growth, and the time to achieve recrystallisation is written using Arrhenius equation:

$$t = A\exp(\frac{Q}{RT}). \tag{2.1.5}$$

After recrystallisation, grains grow with expensing other recrystallised grains. The driving force for grain growth is related to reduction of energy of grain boundaries. Strains induce migration of grain boundaries toward their centres of curvature to look for more correct near neighbours, which is, the general tendency of atoms.

In addition, defect states occur by annealing: annealing in the vacuum ambient remove oxygens out of some of semiconductors. As a result, annealed semiconductors would have oxygen vacancies. Hydrogen annealing with oxide semiconductors such as TiO_2 and ZnO also induce oxygen vacancies due to the reduction of oxygen by hydrogen atoms. For semiconductor manufacturing, these processes of annealing are commonly used such as furnace annealing, microwave annealing, flash lamp annealing, sub-melt laser annealing and melt laser annealing [35]

2.1.3 Sample preparations

All samples were prepared using a laser ablation. Ceramic targets including a mixture of TiO_2, the host material, rare earth (RE) and co-dopant (CD) were irradiated for deposition by the 3rd harmonic of a YAG laser (355 nm, 1 J/cm^{-2} at 10 Hz, 5 nm/sec). Table 2.1 shows informations of used targets for a deposition process. Thickness of thin films were approximately 900 nm for all samples. Table 2.2 describes detailed informations of sample preparation process including details of laser ablation and annealing conditions. Annealing was done in a chamber with an O_2 gas for crystal growth to form the nanometer-sized crystals and optical activation of rare earth ions of the luminescent centre.

It is already reported that trivalent rare earth ions replace tetravalent Ti in TiO_2 matrix

[36, 37], although a substantial difference of ionic radii between trivalent rare earth (approximately 0.95 Å) and tetravalent Ti (0.61 Å). Doped rare earth satisfies the local charge neutral condition and provides donors to TiO_2. Assumingly, doped rare earth induces oxygen vacancies in TiO_2 and they introduce a donor state which provides donors. Detailed experimental results are discussed in Chapter 5.

Table 2.1: Used targets for a laser ablation.

	TiO_2:Sm	TiO_2:Nd:Al	TiO_2:Sm/TiO_2:Sm:Nb
RE	Sm_2O_3 (1 wt%)	Nd_2O_3 (1 wt%)	Sm_2O_3 (1 wt%)
CD	-	Al_2O_3 (0, 0.1, 1, 5 wt%)	Nb_2O_3 (11 wt%)
RE (at %)	0.23	0.24	0.23
D (cm^{-3})	1.1×10^{20}	2.5×10^{20}	1.1×10^{20}
CD (at %)	-	0.08, 0.8, 3.9	6
D (cm^{-3})	-	3.7, 3.7, $1.9 \times 10^{19,20,21}$ cm^{-2}	2.9×10^{21}

Table 2.2: Details of sample preparation.

	A-/R-TiO_2:Sm	TiO_2:Nd:Al	TiO_2/TiO_2:Sm/TiO_2:Sm:Nb
Crystalline phase of TiO_2	Anatase/Rutile	Anatase	Anatase
O_2 pressure (Torr)	1.5×10^{-2}/2.0×10^{-5}	1.5×10^{-2}	1.5×10^{-2}
Substrate	Si(100)	Si(100)	Si(100)/$SrTiO_3$:Nb(100)
Annealing atmosphere	O_2	O_2	O_2
Annealing temperature (°C)	400 -1100	500	700
Annealing time (min)	10	3	30

In Chapter 3, anatase or rutile-phase TiO_2:Sm thin films were fabricated on Si(100) substrate by laser ablation. A mixture of ceramic including TiO_2:Sm_2O_3 (1 wt%, 0.23 at%) was used as the deposition source. The density of Sm atoms in the target is calculated to be 1.1×10^{20} cm^{-3}. The crystalline phase of TiO_2 (anatase/rutile) is possible to be selected by controlling the oxygen pressure in the vacuumed chamber. Detailed information is available in elsewhere [38]. This case, the atmosphere in the chamber was carefully controlled at 1.5×10^{-2} Torr for fabrication of anatase-phase

TiO_2:Sm and 2.0×10^{-5} Torr for rutile phase, respectively. After deposition, a sample series of anatase-phase Sm-doped TiO_2 (A-TiO_2:Sm) and rutile-phase (R-TiO_2:Sm) were treated by post annealing at 8 different temperatures, which is in the range of 400 °C to 1100 °C with 100 °C intervals. Annealing time was 10 minutes for each sample and in a chamber with an O_2 gas. Sm^{3+} shows luminescence in red and infra-red wavelength regions. Comparing luminescent and local fine structural properties between different crystalline phase of TiO_2 would show which crystal structure is better for emissions from rare earth and what is the key property for the enhancement.

In Chapter 4, Nd-doped and Nd-Al-co-doped TiO_2 thin films (TiO_2:Nd/TiO_2:Nd:Al) were deposited on Si(100) surface by laser ablation. Annealing temperature and time were fixed based on optimal condition for stimulating Nd^{3+}-related luminescence in Al co-doping samples for the best of our knowledge from our previous work [39]. Samples were prepared as A-TiO_2 because anatase is better crystal structure for enhancement of rare earth emissions as discusses in Chapter 3. During laser ablating, an O_2 pressure of 1.5×10^{-2} Torr was kept in a growth chamber for selecting crystalline phase of TiO_2 as anatase-phase. A ceramic target is a mixture of host, rare earth and co-dopant, including TiO_2:Nd_2O_3 (1.0 wt%, 0.24 at%):Al_2O_3 (0, 0.1, 1.0, 5.0 wt%/0, 0.08, 0.8, 3.9 in at%). The atomic density of Nd included in the target is simply calculated as 2.5×10^{20} cm^{-3}. The samples were post annealed at 500 °C for 3 minutes in a chamber filled with O_2 gas. Nd^{3+} ions show emissions in infra-red wavelength region. And Al_2O_3 was co-doped as a sensitiser for Nd^{3+} emissions. It disperses Nd^{3+} ions (prevents forming Nd^{3+} clusters) to improve the luminescence.

In Chapter 5, TiO_2, TiO_2:Sm_2O_3 and TiO_2:Sm_2O_3:Nb_2O_3 thin films were fabri-

cated on $SrTiO_3$:Nb(100) or Si(100) substrates by laser ablation. Si(100) substrate was used for samples with *lateral* structure for I-V measurement which means that both Ohmic and Schottky electrodes were deposited on the surface of thin films and bias voltage was applied horizontally. For the vertical structure, $SrTiO_3$:Nb(0.5 at%)(100) (Shinkosha, Japan) substrate was used. $SrTiO_3$:Nb is a highly conductive (3 - 7 $\times$ 10^{-3} Ω) substrate with a doping concentration of 1 -2 $\times$ 10^{20}. A mixture of ceramic including TiO_2:Sm_2O_3 (1 wt%) and TiO_2:Sm_2O_3 (1 wt%, 0.23 at%):Nb_2O_3(11 wt%, 6 at%) were used as the deposition source. The density of Sm atoms in the target is simply calculated to be 1.1 $\times$ 10^{20} cm^{-3}. Anatase phase was selected for the crystalline phase of TiO_2 by controlling the oxygen pressure in the vacuumed chamber. The atmosphere in the chamber was carefully controlled at 1.5 $\times$ 10^{-2} Torr for fabrication. After deposition, samples were annealed at 700 °C for 30 minutes in a chamber with an O_2 gas. Annealing time was fixed for enhancing crystal growth. Nb_2O_3 was co-doped for enhancing conductivity of TiO_2:Sm.

2.2 X-ray Diffraction (XRD)

Yielding information about the nano-scale crystallographic structure is very essential to work with materials, especially, semiconductors. For semiconductors, knowing the crystalline structure such as which plane was well grown and which was poor, is a very important factor. Because each material has an axis to be responsible for conductivity. Therefore, fabricating samples with growth of intended direction of axis has substantial impact, especially for improvement of electric properties such as conductivity, for their

application to devices. X-ray diffraction (XRD) can collect these informations quickly and easily. Especially, XRD is a very efficient technique for large sample areas to be covered. Let us consider about an atom and its structure. In matter, the electric potential is inversely proportional to the distance between the charges on an atomic scale. This "distance" is about 1 Å, which means that the electric potential is altered in solid by an applied electromagnetic field is difficult [40, 41, 42]. However, the atomic potential can modify electromagnetic waves so that electromagnetic waves can be a probe for investigating the atomic structure of matter with no effect on the atomic potentials. X-rays are electromagnetic waves in 10 pm to 10 nm wavelength region, namely, around Å (0.1 nm) order, which is the same order as atomic distance of most of the crystals. The incoming electromagnetic wave field is deflected coherently at the electric or magnetic potential of sample can be considered as X-ray scattering and diffraction. We need to consider scattering at each specific case namely, in bulk, powder, disordered matter and at surfaces.

Firstly, we consider about the scattering at single electrons. The incident electro-

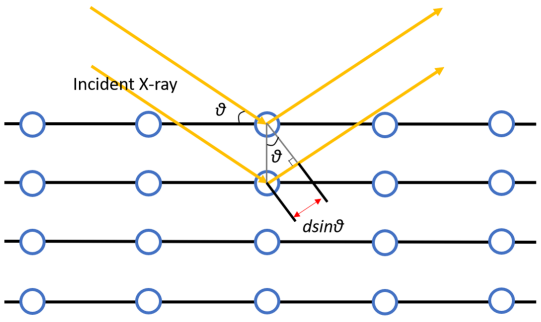

Figure 2.2: Schematic diagram of the Bragg's diffraction.

magnetic wave is considered as a plane wave with wavelength λ. The wave number is described using the wavelength as $k = 2\pi/\lambda$. The wavelength and the photon energy of electromagnetic waves are connected via $E = \hbar\omega$, $\omega = ck$, where $\hbar$ is the reduced Planck constant (Dirac's constant) and ω is the frequency with *c, the* speed of light. If the incident electromagnetic wave radiates just a single electron, exciting the electron and it shows a spherical wave with the same wavelength as the incident beam. The scattering by those electrons can be calculated in the Born approximation by adding the whole corresponding spherical waves. The scattered amplitude by a single particle is described as follows:

$$A(\mathbf{k}) \propto \exp(i\mathbf{k} \cdot \mathbf{r}), \tag{2.2.1}$$

where **q** is wave vector transfer (**q** = $\mathbf{k}_f$ - $\mathbf{k}_i$, the incoming wave $\mathbf{k}_i$ and the outgoing wave $\mathbf{k}_f$). Using this easily connects scattering angles (2θ) with q-space and the opposite is also true:

$$q = 2k\sin\frac{2\theta}{2}. \tag{2.2.2}$$

In crystalline matter, the scattered X-ray intensity is determined by the symmetry of the crystal lattice. The unit cell repeats in all three dimensions for a single crystal. Some of our samples are "perfect" single crystal, but in some cases, they are polycrystals, which means that the orientation of the crystallite is random and no preferred direction: crystals with short to long-ranged ordered atoms over the sample. Contribution of the scattering to one unit cell is taken into account the position of the single atom, which is

called ***S(q)***, structure factor. ***S(q)*** has the information of the phase of the unit cell. The rule of symmetry properties, on the other hand, might cause amplification or extinction of the scattered amplitude for **q** , wave vector transfers. Three lattice vectors **a, b, c** corresponds to a Laue function:

$$\mathbf{q}_{Bragg} = \frac{2\pi}{\mathbf{a}\cdot(\mathbf{b}\times\mathbf{c})}(h[\mathbf{b}\times\mathbf{c}], k[\mathbf{c}\times\mathbf{a}], l[\mathbf{a}\times\mathbf{b}])^T, \tag{2.2.3}$$

where *h*, *k*, *m* are Miller indices. The Bragg angle θ_{Bragg} can be written as q_{Bragg} = $2k\sin\theta_{Bragg}$. A Laue function is described as follows:

$$|F|^2 = f^2\frac{\sin^2(N\frac{2\pi a\sin\theta}{\lambda})}{\sin^2(\frac{2\pi a\sin\theta}{\lambda})}. \tag{2.2.4}$$

The Bragg peaks or Bragg reflections located at the Bragg condition when a Laue function is maximum (a denominator is 0):

$$\frac{2\pi a\sin\theta}{\lambda} = n\pi. \tag{2.2.5}$$

This leads to Bragg's law:

$$2d\sin\theta = n\lambda, \tag{2.2.6}$$

where *d* refers to the interplanar distance between lattice planes, θ is the glancing angle, *n* is a positive integer and λ is the wavelength of the incident beam. As shown in Fig.2.2, $2d\sin\theta$ is the path difference between two incident radiant undergoing interface.

XRD can estimate approximate crystalline domains, *D* ($\approx$ grain size or particle size)

using the Scherrer equation [43]:

$$D = \frac{k\lambda}{\beta \cos\theta}, \tag{2.2.7}$$

where *k* is a mean shape factor, β is the full width at half maximum (FWHM) of XRD peak intensity (radian) and θ is the bragg angle. A mean shape factor *k* is selected as 0.9 due to it is the most suitable for our laser ablated TiO_2 samples [38, 44]. Note that obtained grain size using the Scherrer equation is smaller than actual grain size.

In this study, XRD measurements were carried out for identification of the crystalline phase of prepared samples such as identification of host TiO_2 crystalline phase and ensuring no existance of rare earth oxides clusters. Grain size is estimated for obtaining approximate grain size of samples to compare it between anatase and rutile-TiO_2 and confirming no out-deffusions.

2.3 X-ray Absorption Fine Structure (XAFS)

XRD is efficient technique for yielding crystal structural information over large areas which requires proper length-ranged ordered atoms. In contrast, X-ray absorption fine structure (XAFS) can give information of oxidation state, co-ordination chemistry, co-ordination number, atomic distances and identification of neighbouring atoms surrounding selected element (absorbing element) without requiring crystallinity. XAFS is a very useful atomic probe, but measurement itself is relatively straightforward: firstly, we need an intense/energy-tunable X-ray source for an incident radiant, which means

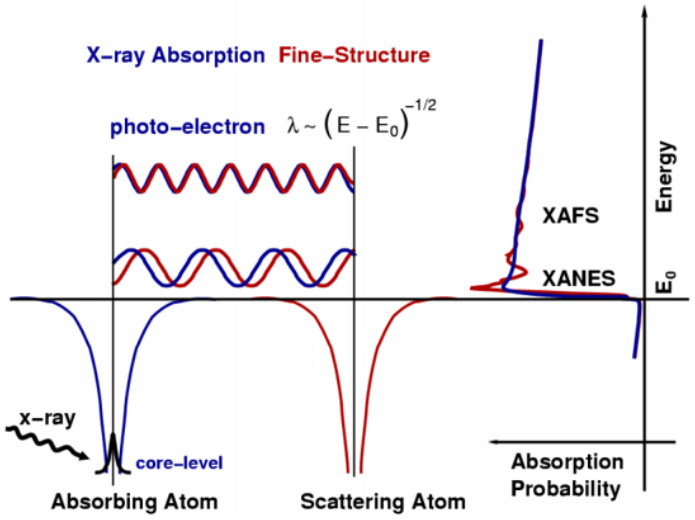

Figure 2.3: Photo-electron excitation from core-level to the continuum and its scattering wave: the connection with XANES and EXAFS spectra. Reprinted with permission from [45], copyright reserved by the Mineralogical Society of America, 2014.

using synchrotrons in most of the cases. The reason why we need an intense X-ray is that binding energy of a core-level electrons such as electron in K or L shells ($1s$ or $2p$ level) is high (tightly bound). When the incident X-ray meets binding energy, a core-level electron promotes out of the atom as shown in Fig 2.3 [45]. This "promotion" to the continuum can be seen in measured XAFS spectra as a very sharp peak. Figure 2.4 shows XAFS spectra. The sharp peak is an absorption edge, which corresponds to the absorption of the incident energy and excitation to the continuum. If the energy of incident X-ray is less than that of the binding energy of core-level, it is not absorbed by the electron. If it is larger than the binding energy, the X-ray is absorbed by the electron and a photo-electron obtains the excessed electronic binding energy. Actually, this is familiar *photo-electric effect*. Simple understanding of XAFS is seeing the energy

difference between a monochromatized incident X-ray intensity I_0 and a transmitted X-ray intensity *I* as follows according to Beer's Law:

$$I = I_0 e^{-\mu t}, \tag{2.3.1}$$

where *t* is the sample thickness and μ is the absorption coefficient determined by each absorption element. This equation gives the measured absorption dependence of the energy coefficient in energy space (*E*) $\mu(E)$ as follows:

$$\mu(E) \sim \log(\frac{I_0}{I}). \tag{2.3.2}$$

Note that *t*, the sample thickness can be seen a contact for an X-ray. This is the reason why we need *tunable* X-ray: each atom has core-level and its binding energy is well known so that the absorption element can be easily *selected* just by tuning the X-ray energy to an appropriate absorption energy [45]. Namely, the hard X-ray is used for a radiant to excite *K* and *L* levels. *K* level in relatively light elements can be excited by the soft X-ray region since the edge energies are varied with atomic number such as Z^2. As can be seen in Fig. 2.4, the XAFS spectra can be dived into two areas in terms of information we can obtain: X-ray absorption near-edge spectroscopy (XANES) and extended X-ray absorption fine-structure spectroscopy (EXAFS). XANES is sensitive to oxidation state and co-ordination chemistry of absorption element with a energy range of 100 eV from the pre-edge (before the absorption edge) to the post-edge (after the absorption edge). Whilst EXAFS is very powerful technique to determine the atomic distances, co-ordination number and identification of the neighbouring atoms

surrounding the absorption element with higher energy range than XANES namely, up to 1 keV from the absorption edge.

XAFS has three modes such as transmittance, fluorescence and electron yield.

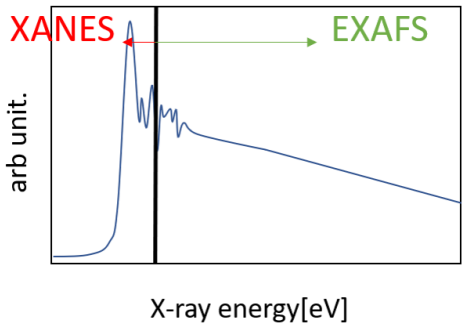

Figure 2.4: XAFS spectra: XANES and EXAFS.

The transmittance mode is the typical mode for measuring XAFS spectra [46, 47]. It is very important to measure good $\mu(E)$ because how to interpret XAFS result totally depends on analysists so that not fairly precisely or accurately measured XAFS spectra (error in $\mu(E)$ is $\approx 10^{-3}$) increase the probability to mislead. It is always good to use the transmittance mode if your sample is suitable for that since it is the authentic and fundamental way of measuring and the technique exactly expresses the basic equation of XAFS spectra ($\mu(E) \sim \log(I_0/I)$). XAFS spectra obtained using other two modes are *modified* based on the theory of the transmittance mode. The fluorescence mode is suitable for "thin and concentrated" or "thick and dilute" (down to the ppm level and lower) samples. If a sample is thin enough, the accuracy of measured XAFS spectra is almost the same as that for measured using the transmittance. Settings of transmission and fluorescence XAFS experiments are shown in Fig 2.5 and 2.6.

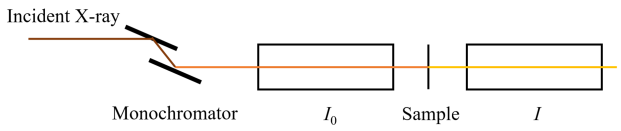

Figure 2.5: Transmission XAFS experiments.

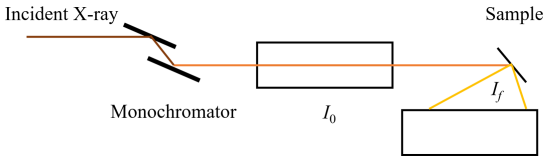

Figure 2.6: Fluorescence XAFS experiments.

We introduce further information of the fluorescence mode since our sample is thin films on a substrate so that it is difficult to obtain the transmitted spectrum through the sample. As can be seen in Fig. 2.6, the sample is placed at an proper angle (usually 45°) and the fluorescence detector is set at 90° to the incident beam in the horizontal plane. Note that the position of the detector and the sample need to be selected to minimise elastically scattered X-rays, which are substantial to increase noise in the detected spectra. Ion chambers (detectors, I_0 and I in Fig. 2.6) are filled with mixed inert gas such as He, N_2 and Ar to be approximately 20%, 90% of the detection efficiency for I_0, I. The incident/fluorescent X-rays ionise a fill-gas are then detected by a parallel plate capacitor with a high voltage and counts pulse (or integrates current) for I_0 and counts photons for I. We can obtain XAFS spectra from X-ray fluorescence using the fluorescence mode whilst we see the energy difference between the incident and

the transmitted X-rays for the transmitted XAFS. There are two de-excitation processes following X-ray absorption. First one is X-ray fluorescence, in which electron in higher level fills the deeper core level. The fluorescence X-ray emits during this transition and the energy of this fluorescence is well-defined and characteristic of the atom. For instance, the electron transition from an *L* shell to an *K* level gives the K_α line. The second decay process of the excited atomic state is that the Auger Effect, in which an electron drops from an excited electron level and a second electron is kicked out and emitted into the continuum (and might go out of the sample). For the electron yield mode, this Auger electrons are detected for indirectly obtaining XAFS spectra. The fluorescence X-ray intensity (I_F) can be given by:

$$(I_F = \frac{\epsilon\mu_i(E)\mathrm{cosec}(\alpha)\,d\Omega}{4\pi}) \int_x^0 \exp(-f(E))x')\,dx', \tag{2.3.3}$$

where ϵ is the fluorescence quantum yield, μ_i(*E*) is absorption coefficient of the absorption element and energy *E* is incident, dΩ/4π is a solid angle to measure the fluorescence, α is the incident angle and x is the depth from the sample surface. Also, *f*(*E*) can be described:

$$f(E) = \mu_T(E)\mathrm{cosec}(\alpha) + \mu_T(E_f)\mathrm{cosec}(\beta), \tag{2.3.4}$$

where, μ_T(*E*) refers to the total absorption coefficient of the sample and β is the escape angle of the fluorescence X-ray. Here, μ_T can be considered to consist of the absorption coefficient of the interest and the absorption coefficient of the others: $\mu_T = \mu_i + \mu_{BG}$. Note that the fluorescence X-ray energy of the selected absorption element, E_f is lower than that for the absorption energy. Integrating these equations and over the detector

solid angle Ω, then the obtained fluorescence X-ray intensity, I_F is:

$$I_F = \frac{\mu_i(E)\epsilon\mathrm{cosec}(\alpha)}{4\pi}\int_{\alpha}^{\alpha+\Omega}\frac{1-\exp(-f(E)x)}{f(E)}d\Omega. \tag{2.3.5}$$

If the sample is very thick, but dilute $f(E)x \gg 1$ and $\mu_i(E) \ll \mu_T(E)$, the exponential term can be neglected and the expression can be simplified as

$$I_F = \mu_i(E)\frac{\epsilon\mathrm{cosec}(\alpha)}{4\pi}\int_{\alpha}^{\alpha+\Omega}\frac{1}{f(E)}d\Omega. \tag{2.3.6}$$

If $f(E)$ changes smoothly with energy sweep, then we can measure $\mu_i(E)$ as we wish. The attenuation caused by absorbance of the sample is always constant because the interest element does not affect the absorbance of fluorescence X-ray and its energy is constant.

On the other hand, for the thin and concentrated sample $f(E)x \gg 1$, then Taylor expansion can be carried out on the equation:

$$I_F = \mu_i(E)\frac{x\epsilon\mathrm{cosec}(\alpha)}{4\pi}\Omega. \tag{2.3.7}$$

In this case, I_F only depends on $\mu(E)$ so that we can obtain accurate XAFS spectrum. However, if the sample is thick and not dilute, I_F is not proportional to an increase of $\mu_i(E)$ because the change of $\mu_i(E)$ over $\mu_{BG}(E)$ is not neglectable [48]. This means that this is the suitable condition for the transmittance mode. This nonlinear dependence of measured signal on $\mu_i(E)$ causes distortion in XAFS spectra and they are no longer to reflect the absorption coefficient. The fluorescence mode is very useful technique

and unnecessary to calculate atomic concentration over the thickness of the sample like the transmittance mode, however the measuring spectra need to be always monitored to keep

$$\mu(E) \propto I_f / I_0. \tag{2.3.8}$$

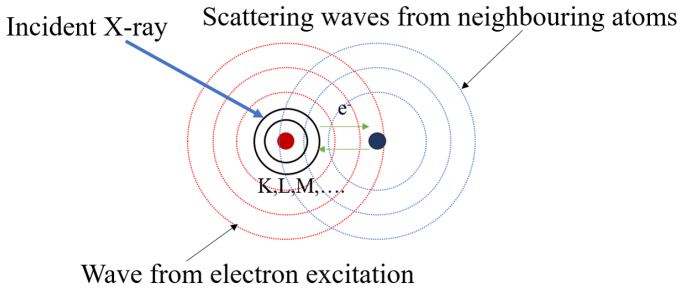

Figure 2.7: How XAFS spectra occur.

For XANES, it is more simple to understand what occurs with the absorption edge. The shape and height of the peak are affected by the energy level of the absorbing atom so that the absorption edge has the information of the oxidisation and co-ordination chemistry [45, 46, 47]. EXAFS needs to be discussed in a more quantitative way with approximations and limits for obtaining better and more accurate informations. When we talk about the EXAFS, it always mean the oscillations above the absorption edge which contains the oscillations of scattering from the neighbouring atoms (informations

of neighbouring atoms) as shown in Fig. 2.7. The EXAFS function can be defined as

$$\chi(E) = \frac{\mu(E) - \mu_0(E)}{\Delta\mu_0(E)}, \tag{2.3.9}$$

where $\mu(E)$ is the obtained absorption coefficient, $\mu_0(E)$ is a smooth background function of the absorption of an isolated atom and $\Delta\mu_0$ is the measured gap between the absorption $\mu(E)$ and the threshold energy E_0. Since we analyse the EXAFS oscillation to obtain the information of the local fine structure around the absorption element (in other words, we are interested in the wave behaviour of the photo-electron created in the process of absorption), it is better and general to convert measured XAFS spectra energy to k, the wave number of the photo-electron. It has dimensions of 1/distance and is given as

$$k = \sqrt{\frac{2m(E - E_0)}{\hbar^2}}, \tag{2.3.10}$$

where m is the electron mass. Now, $\chi(k)$ is the primary quantity for EXAFS, the oscillations as a function of photo-electron wave number, which is usually called the EXAFS. The EXAFS oscillations decay with k so that $\chi(k)$ needs to be emphasised for analysis namely, multiplied by k, but generally k^2 or k^3. The electrons in bound state absorb the incident X-rays and become photo-electrons with spherical wave as shown in Fig. 2.7. The spherical wave photo-electron reaches to neighbouring atoms located at r_i and it is back scattered by them. Different neighbour co-ordination causes the difference of frequencies in the EXAFS oscillations, $\chi(k)$, which can be written and

modeled according to

$$\chi(k) = S_0^2 \sum_i \frac{N_i f_i(k_i) \exp(-2k_i^2\sigma_i^2)}{k_i r_i^2} \sin(2k_i r_i + \delta_i(k_i)), \tag{2.3.11}$$

where $S_0$is the difference in EXAFS between with and without the hole created by the X-ray absorption and multi excitations, N_i is the coordination number, f_i is the backscattering intensity, ${\sigma^2}_i$ is the Debye-Waller factor which includes thermal vibration and static disorder, r_i is the average distance of the *i*th shell and δ_i is the phase shift.

2.3.1 EXAFS Analysis and efforts for improvement of its accuracy

The data reduction and analysis are essential for XAFS measurement. Here, we introduce some efforts we have done for obtaining better and more accurate XAFS spectra and results.

First, sample preparation is the most important process for XAFS measurement. Good samples for the measurement need to meet 1. flat and uniform and 2. including proper number of absorption elements. Some softwares provide optimal thickness or amount (depends on a sample) from the information of the absorption element concentration in a sample (Please find one of them at https://pfxafs.kek.jp/xafs-experiment/software/). After this step, many difficulties await for us to reach accurate results, however, it is always a good idea to come back to a sample preparation process and reconsider about it. For our samples, we fabricated relatively thick films (approximately 900 nm) comparing with our usual films for PL measurement or a layer in LED devices (200 - 300 nm) because of this reason.

Secondly, the data reduction is also crucial for keeping accuracies. The data reduction steps are shown as follows:

1. Conversion of measured signals to $\mu(E)$- correction of systematic measurement errors (i.e. self-absorption effects and detector dead-time) are possibly needed.
2. Subtraction of a smooth pre-edge (before the absorption edge) function from $\mu(E)$ for removing instrumental background and absorption from other edges.
3. Identification of the threshold energy E_0(typically it is the energy of the maximum derivative of $\mu(E)$).
4. Normalisation of $\mu(E)$ to go from 0 to 1- it represents the absorption of an X-ray and it is useful for XANES analysis.
5. A smooth post-edge (after the absorption edge. The software shows red line called "spline" and its accuracy, smooth or not, is determined by the previous steps) background function removal to approximate $\mu_0(E)$.
6. Isolation of the XAFS $\chi(k)$, where $k = \sqrt{2m(E - E_0)/\hbar^2}$.
7. k-weighting XAFS $\chi(k)$ and Fourier Transform into R-space.

For the post-edge subtraction of XAFS in the fifth step, it is better to set the background function in the middle of the oscillations.

Next step after the data reduction is selecting a range of window function and a multiplier for k for a Fourier Transform from XAFS signals in k-space to R-space. These are determined based on the periodicity of the oscillations in XAFS: if the noise level is low enough, we can confirm it at high k (higher than 8). The window function usually starts from 2 , weighting by k^n amplifies the oscillations (n = 1, 2, 3). Higher

k^n emphasies the oscillations at high *k*.

The curve fitting is the most important and the most difficult step for XAFS analysis and always challenging. Including the mean-free-path of the photo-electron λ, the equation 2.3.11 can be written as:

$$\chi(k) = S_0^2 \sum_i \frac{N_i f_i(k_i) \exp(-2k_i^2\sigma_i^2) \exp(-2r_i/\lambda_k)}{k_i r_i^2} \sin(2k_i r_i + \delta_i(k_i)). \quad (2.3.12)$$

For extraction of the distances and co-ordination numbers, accurate values for the scattering amplitude and phase-shifts caused by scattering atom and absorption atom *f(k)* and δk are needed. One tip for accurate determination of these factors is using the information of a standard sample. For *known* sample, a co-odination number *N* and an atomic distance between scattering atom and absorption atom *r* are known and others are unknown. Note that $S_0$and $N_i$determine amplitude, r_i determines peak position of the oscillations and f_i, σ_i and λ_k determine peak height of the each oscillations. From curve fitting on standard sample, we can yield the information of S_0 using $S_0 \times N_i$ = amplitude of measured XAFS spectra. Because S_0 can be applied to other XAFS data if either is measured from the same absorption element. Also, making proper fitting models are also essential: a fitting model is made based on measured XRD data with co-ordinates. We can edit co-ordinates of extracted data such as absorption element and co-ordinates using FEFF programme. This means that we can make various models such as interstitial and substitution. Once fitting model is prepared, we can start the curve fitting. We need to adjust the fitting parameters shown in the equation 2.3.12. Table 2.3 shows the reliable values for the fitting parameters. The fitting programme

Artemis calculates *"R-factor"* at every fitting. R-factor shows the accuracy of the curve fitting and if it is less than 0.1, the result is reliable enough. If the model is close to the crystal structure of measured XAFS spectra, fitting parameters can be adjusted, otherwise it is very difficult to reduce R-factor. Note that all the fiting results shown in this thesis meet these requirements for reliability. R-factors are 0.009 - 0.0038 (fitting results of anatase-/rutile- TiO_2:Sm samples in Chapter 3) and 0.012 - 0.033 (TiO_2:Nd:Al samples in Chapter 4). Error bar is an average of obtained R-factors which is $\pm$ 2.7 for samples discussed in Chapter 3 and $\pm$ 1.7 for samples in Chapter 4.

Table 2.3: Reliable values for fitting parameters in XAFS analysis.

S_0^2	ΔE_0	σ^2	R-factor
0.7 - 1.1	-10 - 10	0.003 - 0.02	<0.1

XAFS measurements were performed at BL-9A (for the measurements in Chapter 3) and BL-9C (for the measurements in Chapter 4) of Photon Factory, High Energy Accelerator Research Organization in Tsukuba, Japan. Figure 2.8 shows inside of the hatch of BL-9A.

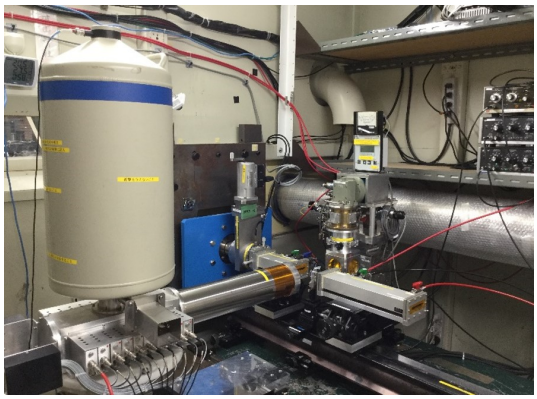

Figure 2.8: BL-9A, Photon Factory of High Energy Accelerator Research Organization, Tsukuba, Japan.

2.4 Optical Spectroscopy

2.4.1 Photoluminescence

Luminescence

Luminescence- emission of light, can occur/be excited by various types of energy source. The most familiar luminescence for people is surely flame luminescence that you can see when you use an oven, a candle and an incense. Chemiluminescence occurs as a result of a chemical reaction such as the luminol test. Blood can be identified by luminescence caused by a chemical reaction between a reagent and iron. Bioluminescence is shown due to biochemical reactions in a living orgasm, reason being fireflies growing is that the oxidation of the luciferin. Fractoluminescence is exhibited by breaking crystal consisting of "material" when two or more hard materials are rubbed by each other. Cathodoluminescence (CL) occurs as a result of electrons striking a luminescent material. Scanning Electron Microscope (SEM) has a cathodoluminescence mode. Televisions of the previous generation have a phosphor coated screen uses a cathode ray tube, which exhibits emissions by electron beam scanning. Electroluminescence (EL) is shown by applied voltage as the result of recombination of electrons and holes in semiconductor. A material with phosphor needs to have *p*-*n* junction or Schottky junction, which have depletion layer. There are two types of EL, one is EL caused by applying relatively low voltage (around 5 V). In other words, applied electric current passes through the circuit. Light emitting diodes (LEDs) shown emissions by this way. Other one occurs by a strong electric filed: accelerated high energy electrons hit/excite luminescent centres in semiconductors and they show luminescence. A familiar exam-

ple is EL displays. Finally, photoluminescence (PL) is a luminescence caused by light (photon). In this work, PL is performed as one of the main experiments.

Photoluminescence (PL)

Photoluminescence (PL) is widely used as a useful optical technique measuring spontaneous radiative transitions between two bound states, an excited state (E_n), electrons/holes/excitons are excited by energy via absorption, and transit to a lower state (E_i) or sometimes the ground state (E_0) in atom, compound or molecular. PL is very powerful technique to specify the relationship between transitions and energy states because the energy difference between E_n and E_i is material-related [14, 33, 49, 50, 51]. For instance, you can see whether it is defect site such as luminescent centre caused by doping phosphor or electronic defect or general native energy state-related such as band-edge recombination in semiconductors from PL spectra. Typical PL system consists of a laser excitation source, monochromator and detector as shown in Fig. 2.9. Emission spectrum (the distribution of the radiant flux) can be described with the relation between E_i and E_n:
the absorption energy E_{abs} is equal to $h\nu_{abs}$ and if it is:

$$E_{abs} = h\nu_{abs} \geq E_i. \tag{2.4.1}$$

It is strong enough to excite electrons/holes/excitons exist in a lower state or the ground state upto an excited state, then

$$h\nu_{in} = E_n - E_i. \tag{2.4.2}$$

Those "emissions" are called radiative transition/return. However, the radiative transition is not the only result of absorption because radiative transition has a competitor: there is non-radiative transition/return, a loss term for luminescence. The fluorescence decay time (effective lifetime) is described as following:

$$\frac{1}{\tau_{eff}} = \frac{1}{\tau_R} + \frac{1}{\tau_{NR}}, \tag{2.4.3}$$

where τ_{eff} is the fluorescence decay, $1/\tau_R$ is radiative transition rate and $1/\tau_{NR}$ is non-radiative transition rate. The result of non-radiative transition appears as phonons, whilst radiative transition shows emissions. The excited energy is used to vibrate the host lattice. The fluorescence quantum efficiency is also given by $\eta = \tau_{eff}/\tau_R$. Therefore,

$$\tau_R = \frac{\tau_{eff}}{\eta}, \quad \tau_{NR} = \frac{\tau_{eff}}{1-\eta}. \tag{2.4.4}$$

This means that measuring the luminescence lifetime allows to calculate radiative and non-radiative transition lifetimes [52].

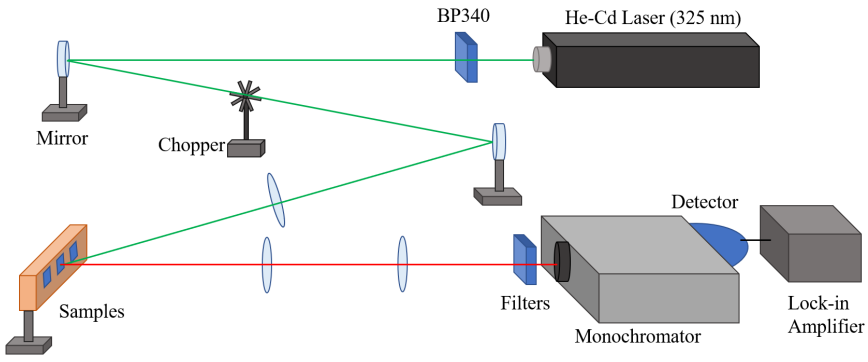

Figure 2.9: Schematic diagram of a simple PL system.

2.4.2 Scanning Electron Microscope (SEM)

Scanning electron microscopy (SEM) is a microscope using electron as a probe which produces sample surface image by scanning the surface. The interaction between electrons and atoms in a sample produces signals containing various information of the surface. Samples are set in a high-vacuumed chamber for *scanning*, and beam currents down to 10^{-11} A to give acceptable secondary electron currents. The most common mode in SEM is detecting secondary electrons emitted by atoms which are excited by an electron beam in a system. A beam energy of SEM is typically over a range of 0.5-30 keV or more with beam divergence from 5 to 100mrad and beam diameter from 1 to 1000 nm. Selecting a particular set of beam conditions is determined by the characteristics of the image contrast or seeking type of information. Figure 2.10 illustrates schematic diagram of the components of a simple scanning electron microscope. The SEM system consists of two subsystems: 1. an electron optical column which produces a finely focused electron probe for a raster scanning over the surface and 2. a detection system including some signal processing and output facilities. Also, the specimen together with the necessary stage facilities is essential. These three essential elements determine the performance of the system [53].

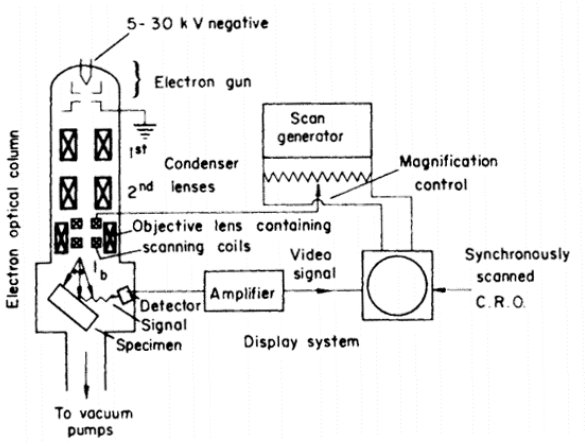

Figure 2.10: Schematic diagram of a simple SEM system components. Reprinted with permission from [53], copyright reserved by Elsevier, 1989.

2.5 Electrical measurement, especially Junction Spectroscopy

2.5.1 Junction structure

To perform electrical measurement such as capacitance - voltage (C-V) measurement needs a sample with depletion layer. Samples with *p*-*n* junction or Schottky junction diodes have depletion region, and its width and depth are changed by direction and the amount of injected electrons. These depletion manageable structures allow us to yield more accurate and useful information about semiconductors. In this section, we would like to focus on *n*-type semiconductors with Schottky contact to understand this structure.

When we deposit a metal on a semiconductor, we need to pay attention to the difference in energy between the work function, ϕ_m of the deposited metal which is

required energy to take an electron from the Fermi level E_F to the vacuum level (outside the surface of the metal), and the electron affinity, χ_s of a semiconductor, the energy difference between the vacuum level and the bottom of the conduction band [30, 55, 56]. If ϕ_m is greater than χ_s as Fig. 2.11, then the semiconductor would have a *Schottky barrier*:

$$\phi_b = \phi_m - \chi_s. \tag{2.5.1}$$

This means that the barrier height, ϕ_b is determined by the energy difference from the Fermi level of semiconductor to the bottom of the conduction band of a semiconductor [55, 30, 56]. The equation above can be applied to the ideal *n*-type semiconductors and metals, or rahter say, the ideal interface. A depletion region is made in a semiconductor near the interface with a metal if the Schottky barrier height is high enough as described in Fig. 2.11. Also, the bult-in potential is given by:

$$q\phi_{bi} = \phi_m - \chi_b(E_c - E_F), \tag{2.5.2}$$

where E_c is the energy of the conduction band-edge and q is the charge of electron. On the other hand, if ϕ_m is greater than χ_s in *n*-type semiconductor as shown below:

$$\phi_m < \chi_s, \tag{2.5.3}$$

it has the Ohmic contact as shown in Fig. 2.12, which can be used for measuring Hall effect measurement, but not for junction spectroscopy.

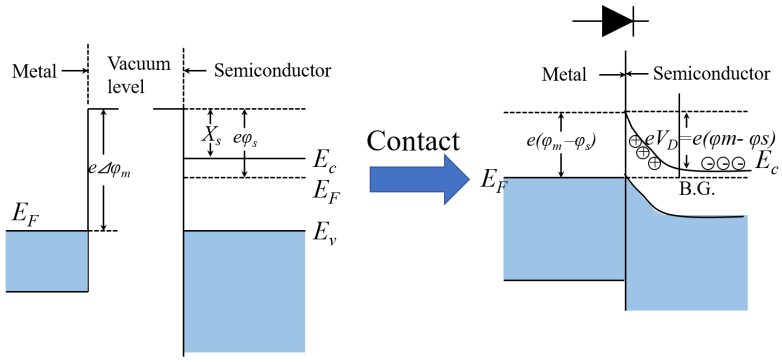

Figure 2.11: Schematic diagram of metal contact with *n*-type semiconductor causing band-bending: Schottky contact.

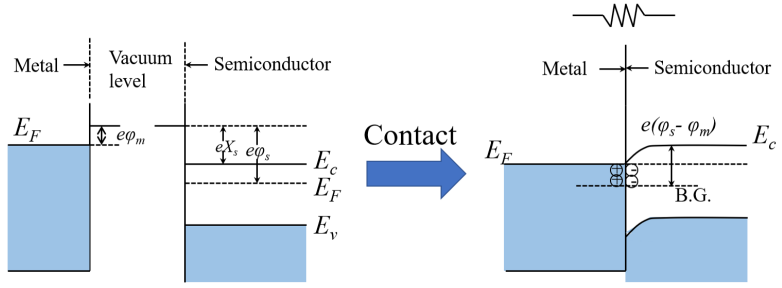

Figure 2.12: Schematic diagram of metal contact with *n*-type semiconductor: Ohmic contact.

Table 2.4 shows an electron affinity of TiO_2, a host material of rare earth and a work function of metals fabricated as Schottky/Ohmic contacts on TiO_2 surface [57, 58, 59]. It shows that for TiO_2 (*n*-type), Au and Ru_2O_3 elecrodes make Schottky contact and a Ti electrode makes Ohmic contact.

Table 2.4: An electron affinity of TiO_2 and a work function of metals fabricated as Schottky/Ohmic contacts on TiO_2 surface.

	TiO_2	Ti	Au	Ru_2O_3
Work function (eV)	-	4.33	5.2	4.6 - 5.0
Electron affinity (eV)	4.23	-	-	-

2.5.2 Capacitance - Voltage (C-V) measurement

Capacitance-voltage (C-V) characterisation is a very important technique for the semiconductor research. It is necessary to evaluating materials, device performance if it is new and/or being improved. In addition, it is the perquisite requirement for junction spectroscopy because the behaviour of diodes such as capacitance, carrier concentrations and depth of the depletion, is critical for measurements. Since the capacitance is used as a probe for the measurements, C-V measurement can be said that technique which evaluates how good probe for the junction spectroscopy. C-V characterisation provides information of: charge carrier density, charge density distribution, drive level capacitance profile and built-in potential.

The capacitance (C) per unit area can be determined by the following equation:

$$C = -\left(\frac{dQ}{dV}\right). \tag{2.5.4}$$

Where *Q* is the charge in the depletion region of the diode and *V* is the junction voltage. The *Q* can be expressed as:

$$Q = qNWA. \tag{2.5.5}$$

Where *q* is the elementary charge, *N* is the doping concentrations, *W* is the width of the depletion region. *A* is the area of the Schottky contact. Whilst the diode is under reverse bias (i.e. positive voltage applies on *n*-type semiconductor or negative voltage applies on *p*-type), the structure can be described as:

$$V = V_{bi} + V_{bias}. \tag{2.5.6}$$

Where V_{bi} is the built-in potential and V_{bias} is the applied voltage. And capacitance is

$$C = -\frac{dQ}{dV} = \frac{\epsilon_0 \epsilon_{semi} A}{W} = qAN(W)\frac{dW}{dV}. \tag{2.5.7}$$

Where ϵ_0 is the dielectric constant under the vacuum. This can be rewritten for acceptor or donor concentrations (N_A or N_D) as

$$N(W) = -\frac{C^3}{q\epsilon_0 \epsilon_{sem} A^2 \left(\frac{dC}{dV}\right)}. \tag{2.5.8}$$

$1/C^2$ against V_{bias} produces a straight line if the doping concentration is uniform. The doping concentration ($N_A{}^-$, $N_D{}^+$) can be determined from the slope in the plot. For the C-V measurements, the application of DC voltage and C-meter which can measure AC

signal are required. The AC frequency from about 10 kHz to 10 MHz are generally used for the measurements. As we manage with AC circuit for admittance spectroscopy, we introduce the complex values for the easier discussion about phase difference between input and output. Resistance, *R* can be defined as the ratio of voltage, *V* to current, *I* , through the object, whilst the conductance, *G* is the inverse of resistance:

$$R = \frac{V}{I}, \;\; G = \frac{1}{R}. \tag{2.5.9}$$

In alternating current (*AC*) circuits, resistance can be extended to impedance, *Z* :

$$Z = R + i\chi. \tag{2.5.10}$$

Where the real part of impedance is resistance, *i* is the imaginary unit and the imaginary part is reactance, χ . In addition, admittance, *Y* is the inverse of impedance, which means impedance represents how resistive and admittance represents how conductive. Admittance can be expressed as follows:

$$Y = \frac{1}{Z} = G + i\omega C, \tag{2.5.11}$$

where the real part of admittance is conductance and the imaginary part is susceptance, $i\omega C$. Where omega is the angular frequency, which can be given by the following relation with the frequency: ω=$2\pi f$. Admittance spectroscopy can scan on either frequency or temperature basis, and analysed as the function of frequency and temperature.

2.5.3 Deep Level Transient Spectroscopy

Deep Level Transient Spectroscopy (DLTS) is one of the junction spectroscopies which can be used for characterising deep level impurities (please find Section 1.4, Chapter 1) within the depletion regions in semiconductors. It has been over 60 years since thermal emission from current carriers from defects was focused as an efficient technique to characterise. The very first clear publication on transient spectroscopy was reported by Sah et al in 1970 [60]. Sah reviewed earlier work on the basis of experimental methods for estimating deep states characteristics within the depletion region of the p-n or Schottky diode. It can be simply described as a development of *C-t* and *I-t* measurements and methods for analysing deep level defects. Earlier works of understanding deep levels before Sah such as thermally stimulated current (TSC) or thermally stimulated capacitance (TSCA) technique mainly focused on bulk high resistivity materials. However, they had major problems such as lack of sensitivity and difficulty of discrimination of different defect levels. The use of the depletion region in junction spectroscopy, therefore, has advantages over bulk. Firstly, it is easy to distinguish a small change or a small number of carriers, which is not easy thing to do with bulk. Secondly, controlling to fill/empty energy levels in the bandgap is easier than in bulk. In 1974, Lang introduced a more simplified technique than previous techniques, which is now called DLTS [30, 55, 61, 62, 63, 64]. The analogue signal processing, so called a double box car system, works as a noise spectrum to enhance the S/N ratio for detecting low concentration traps and to determine emission rate window. With the advantage of junction spectroscopy, it made it possible to characterise a very

small change and a very small concentrations of defect states. This is a very powerful and effective technique for characterisation of both majority and minority carrier traps using *p-n* junction or Schottky diode as a probe to detect them. This technique provides us information about the concentrations of trap, activation energy and capture cross-section. It is possible to measure DLTS with a carrier concentration of 10^{15} cm^{-3} in semiconductor to analyse electrically active defects.

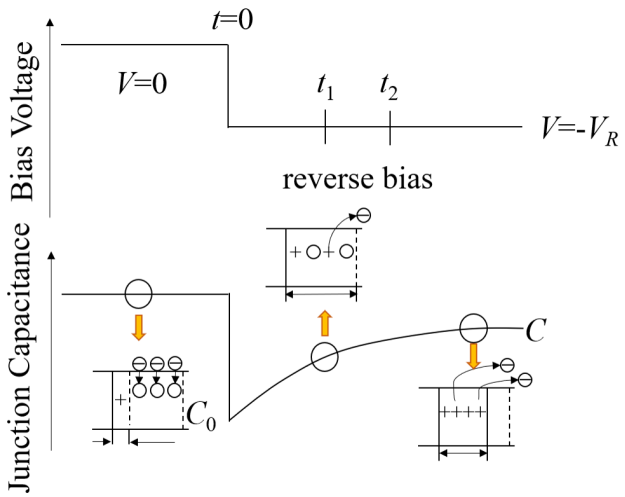

Figure 2.13: Schematic diagram of DLTS measurement.

DLTS is used with a capacitance measurement of the junction as a function of temperature. Basically, DLTS is the simple technique to be implemented. At first, the deep level defects are filled by free carriers, which are excited by excitation source either electrical or optical ways. The pulsed voltage- from zero voltage bias with a short period of time to very low reverse voltage is usual for DLTS. The deep level is filled with majority carriers due to a shift of Fermi level by this process. Then, a thermal release can be observed with changing the temperature as a transient response in capacitance.

A simple, but the most significant difference between DLTS and other previous thermal spectroscopies is measuring capacitance at two set points, t_1 and t_2, which is referred as the rate window. If the temperature is high for thermal activation of filled defect to emit, there is no change in capacitance between t_1 and t_2 ($C(t_1) = C(t_2)$) because emission is too quick. Likewise, if the temperature is too low, there is no DLTS signal. However, when the temperature is just right for emission, the slight difference in capacitance can be observed (usually it's up to pico-Farads order). Schematic diagram of pulsed bias voltage, capacitance and DLTS spectra during increasing temperature is shown in Fig. 2.13.

Chapter 3

Influence of annealing temperature on Sm-doped TiO_2

3.1 Introduction

There are some ways to improve luminescence from rare earth phosphors such as annealing or co-doping. This *improvement* is due to the small absorption cross-section of rare earth elements are affected by the crystal field. The 4*f*-*f* transitions of electric-dipole transition in free rare earth ions is generally forbidden and very weak limited transitions (oscillator strength, $f < 10^{-6}$) such as magnetic-dipole and electric quadrupole transitions are allowed. In solid, electro-dipole transition can be partially allowed because the wavefunction involved in the 4*f* transitions are affected by the crystal filed and lattice vibration.

In addition, there are some literatures reporting that local fine structure around rare earth ions plays an important role to enhance emissions from the luminescent centre [65, 66]. Most of the studies discussed the importance of distortion in the first nearest neighbour (F.N.N) of rare earth atom, which is typically oxygen. However, we can assume that it is also important to analyse local fine structure including the second nearest (S.N.N.) neighbour. Because as we discussed in Chapter 1, an excitation process of rare earth ions is *via* host material so that it is essential to consider both in atomic scale and unit cell scale: if local fine structure is responsible for luminescence intensity, then surely there is a better co-ordination not just only for the F.N.N., but also for the S.N.N. and further. In this chapter, the result of luminescence and local fine structure analysis on samarium (Sm)-doped TiO_2 will be presented. Annealing is a selected technique to give some stimulations to ligands for emission enhancement from rare earth ions.

3.2 Experimental details

Please find sample preparation section (Section 2.6, Chapter 2) for detailed informations. Prepared samples are anatase or rutile-phase TiO_2:Sm (1 wt%, 0.23 at%) thin films annealed at 8 different temperatures, which is in the range of 400 °C to 1100 °C with 100 °C intervals.

X-ray diffraction (XRD) was used to subject all samples to structural determination and calculate grain size. The excitation source for photoluminescence (PL) measurement was a He-Cd laser (λ = 325 nm).

For analysing local fine structure around Sm^{3+}, fluorescence X-ray absorption fine

structure (XAFS) spectra were measured by synchrotron radiation (SR) at the High Energy Accelerator Research Organization on BL-9A, Photon Factory in Tsukuba prefecture, Japan. The SR beam is monochromatised by a Si(111) double crystal set and a nineteen-element Ge-solid state detector was used for detecting signals. The fluorescence signal from the samples excited by an X-ray with the incident angle of 45° were counted using a seven-element pure-Ge solid-state detector. Free programmes the Athena and Artemis of Demeter created and shared by Bruce Ravel were used to extract the oscillations and fit the Fourier spectra for XAFS analysis [54].

3.3 Results and discussion

3.3.1 XRD measurements and grain size estimations for A- and R-TiO_2:Sm as a function of annealing temperature

XRD patterns for the fabricated sample series of A-TiO_2:Sm are shown in Fig. 3.1 (a). All diffraction peaks originate from anatase-phase characteristic except a spectrum for annealed at 1100 °C, e.g. the (101), (103), (004), (112), (200), (105) and (211) planes at 25.6°, 37.3°, 38.1°, 38.9°, 48.3°, 54.2° and 55.3°. Note that Si-related peak at 33.3° was removed for emphasising TiO_2-related peaks. Characteristic of rutile-phase is found in diffraction peaks for 1100 °C annealed: the (110), (101), (200), (111), (210), (211) and (220) planes at 27.4°, 36.1°, 39.2°, 40.1°, 44.0°, 54.3° and 56.6°. One small peak subjected to the anatase (101) plane can be seen at 25.6°. In general, anatase TiO_2 to rutile phase transform occurs by the kinetics, which typically are caused by

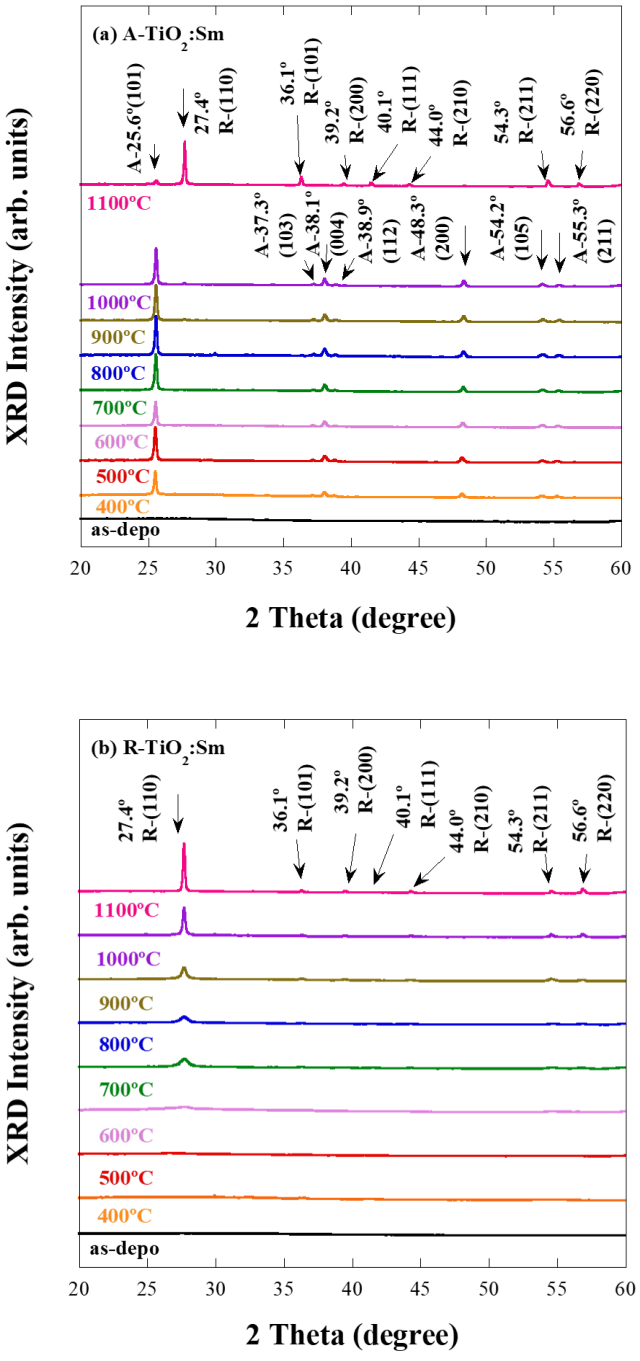

Figure 3.1: XRD patterns of (a) anatase- and (b) rutile-phase TiO_2:Sm [67]. Copyright reserved Wiley-VCH, 2019.

heating energy [68]. Various transition temperatures are reported from 400 to 1200 °C with samples prepared using different synthesis and raw materials (pure bulk anatase). The kinetics of transition are determined by temperature and time: they depend on technique for sample preparation process, impurities, dopants, particle size and shape, surface area, sample volume, heating conditions such as heating rate and flow and so on. In this study with our prepared samples, we confirmed that annealing temperature of 1100 °C is the phase transition temperature. Whereas, samples fabricated as rutile-phase by controlling oxygen pressure in a chamber showed rutile-phase TiO_2 patterns, as shown in Fig. 3.1 (b). Diffraction patterns correspond to the (110), (101), (200), (111), (210) and (220) planes of rutile-TiO_2 at 27.4°, 36.1°, 39.2°, 40.1°, 44.0°, 54.3° and 56.6°. The as-deposited samples of A-, R-TiO_2: Sm showed no peaks except the peak for Si substrate. This suggests that these samples are amorphous phase. For the A-TiO_2 samples, anatase-related peaks can be seen from 400 °C annealed. This means that crystallisation was induced by annealing. On the other hand, the rutile-phase samples showed peaks subjected to rutile-phase from 700 °C (a small bump can be seen at 600 °C annealed). As can be seen in the fact that anatase-phase is transformed to rutile by temperature (energy), it is apparent that rutile needs higher temperature (more energy) to be crystallised than anatase.

Figure 3.2 demonstrates the grain size of crystal derived from a Scherrer analysis of the diffraction peaks (the full width at half maximum, the FWHM of the XRD peaks) presented in Fig 3.1 (a) and (b). Grain lengths along (101) direction were calculated to be 20 to 40 nm for A-TiO_2:Sm samples: grain size increased with increasing annealing temperature up to 800° and kept grain sizes at 900 and 1000°. For 1100° A-TiO_2

sample, grain size dramatically decreased to 15 nm. However, grain size calculated from rutile-related (110) peak was approximately the same size of that for 900 and 1000° samples. This suggests that annealing stopped providing its energy to crystal growth for above 800° samples, but to transforming to rutile-phase. For R-TiO_2 samples, grain sizes were 10 to 40 nm and increased with growing temperature.

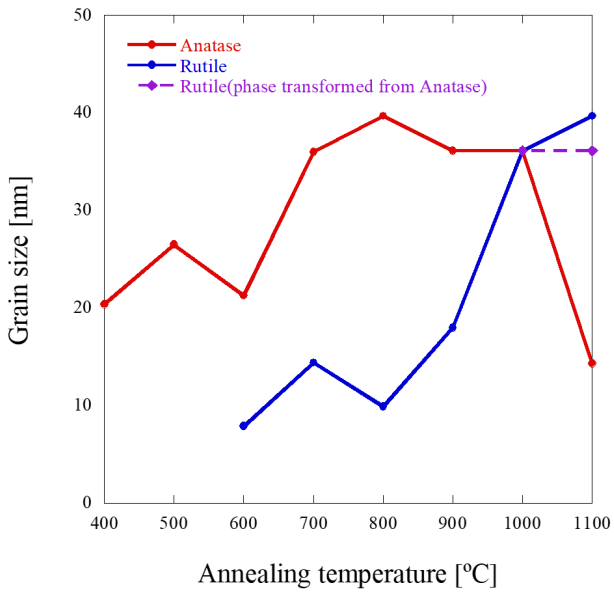

Figure 3.2: Grain size of A- and R-TiO_2:Sm as a function of annealing temperature. Calculated from Fig 3.1 through the Scherrer equation.

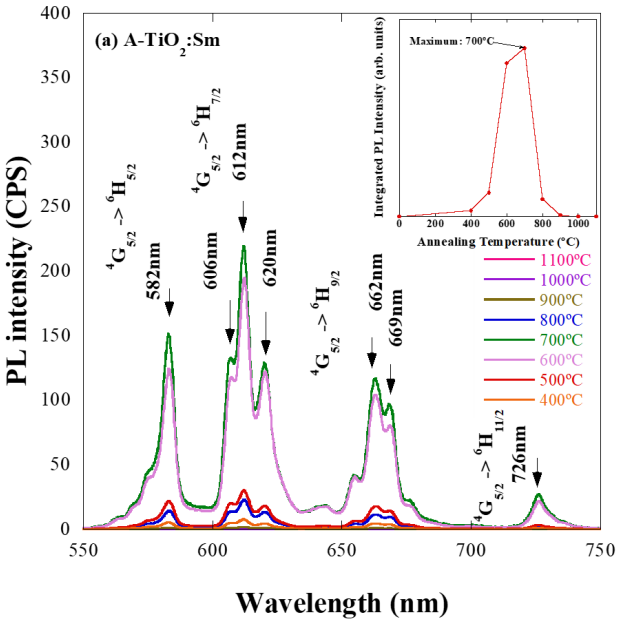

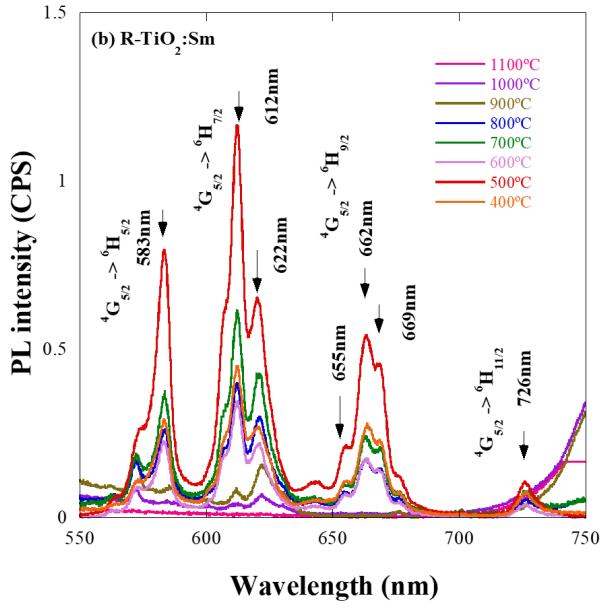

Figure 3.3: PL spectra of (a) anatase- and (b) rutile-phase TiO_2:Sm samples. The inset in (a) is the integrated PL intensity for A-TiO_2 samples [67]. Copyright reserved Wiley-VCH, 2019.

3.3.2 PL measurements for TiO_2:Sm as a function of annealing temperature

The luminescent properties of A- and R-TiO_2 were characterised by PL measurements at room temperature (RT). Figure 3.3 (a) shows PL spectra for a series of A-TiO_2:Sm. Peaks with arrows corresponding to the typical intra-4*f* transitions in Sm^{3+}, $^4G_{5/2} \rightarrow {}^6H_J$ (*J* = 5/2, 7/2, 9/2 and 11/2). Note that peaks without assignment of transition are transitions caused by Shtark effect. The integrated PL intensity at the 612 nm peak for A-TiO_2 as a function of the annealing temperature is illustrated in the inset of Fig. 3.3 (a). The PL intensity increases with annealing temperature increase up to 700 °C, which is the maximum of the intensity. After 700 °C, the intensity quenches dramatically. This result confirms consistency with our previous work [38] and the window of emission activated by annealing is in the range of 400 °C to 800 °C. The PL intensity for 700 °C is two orders of magnitude stronger than above 800 °C samples.

PL spectra for a series of R-TiO_2 are demonstrated in Fig. 3.3 (b). Shape of the PL spectra is similar to that of the A-TiO_2 series. Although they are not precisely the same and it is difficult to be compared with each other since PL spectra of R-TiO_2 are too weak. Basically, both the A-, R-TiO_2:Sm samples have been prepared and stored on the same conditions, such as doping density, fabrication method (except atmosphere) and annealing conditions. Due to the PL nature of Sm, this means that PL peaks for both series appear at almost the same position. However, the PL spectral shape can differ because the transition probability for each energy level is determined by the parity of electron configurations. For rare earth elements, crystal field changes parity to electric-dipole allowed. Therefore, the result of the PL measurements with different spectra

shape suggests that the atomic co-ordination around Sm^{3+} in R-TiO_2 is different from that in A-TiO_2. The maximum PL intensity of the A-TiO_2:Sm is 200 times stronger than for that R-TiO_2:Sm, which indicates that for application to optoelectronic devices, anatase-phase TiO_2 has potential to be a better candidate.

3.3.3 Local fine structure analysis around Sm^{3+} in A-, R-TiO_2

For characterisation of the local fine structure around Sm^{3+} ions of the luminescent centre in TiO_2 host crystal, XAFS measurements were carried out. Obtained signals (Sm^{3+} scatters absorbed incident energy) have the information about electronic configurations, atomic distances and numbers to/of neiboughring atoms. XAFS spectra at Sm L_{III} - edge of (a) A- and (b) R-TiO_2:Sm in shown in Fig. 3.4. In the lowest, a standard sample of Sm_2O_3 powder is also presented. Standard sample is measured to identify ionisation of measuring samples, comparison of the position of absorption edge (also called 'white line') between both. The fine structure of the absorption edge provides information about its electronic (charge) state and the position gives information about the oxidisation state of the absorbing element. The energy shift of absorption edge, which is sometimes caused by system-related issue, not material-related, can be also checked by measuring standard sample. All samples showed the absorption edge at 6720 eV as the same as for the standard sample. This suggests that Sm is properly formed as trivalent in TiO_2 matrix since the valence number of Sm cation is +3 in Sm_2O_3 and this is assigned to 2*p*-5*d* transition of Sm^{3+}. XAFS measurements were carried out also for the series of R-TiO_2:Sm to find consistency or trend with the PL result and to be

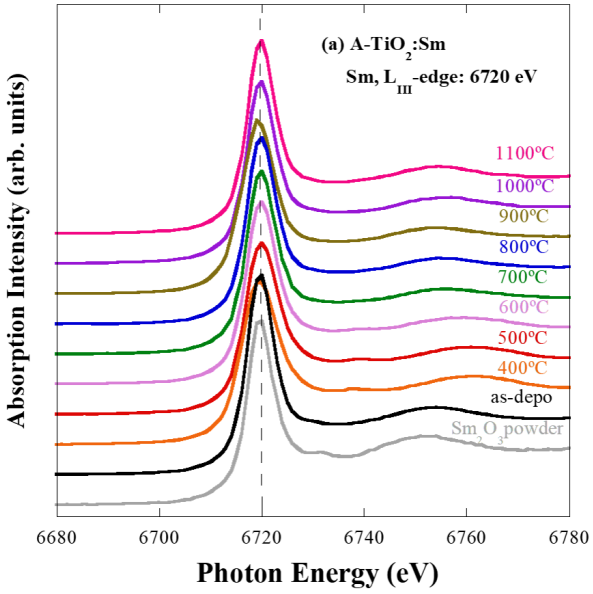

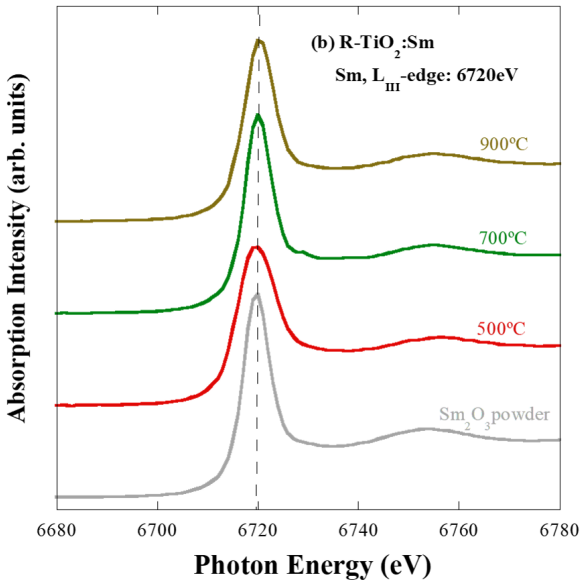

Figure 3.4: XAFS spectra of (a) A- and (b) R-TiO_2:Sm.

compared to A-TiO_2:Sm samples. Three different R-TiO_2 samples are selected because it is previously reported that R-TiO_2:Sm does not change its co-ordination around Sm^{3+} with increase of annealing temperature [44].

Figure 3.5 shows k^3-weighted extended X-ray absorption fine-structure (EXAFS) spectra for A- and R-TiO_2:Sm samples. EXAFS oscillations can be obtained from XAFS spectra with background subtraction with suitable k-weighting. A heavier weighting of k^n means emphasising higher oscillations which contains the information (scattering waves) of neighbouring atoms. This is the reason why we need clear higher oscillations for analysing far neighbouring atoms. Weighting by k^3 means emphasising oscillation at high k (around 8 Å). A window function was performed in the range of 3.0-9.0 $Å^{-1}$, dk = 0.5, chosen on the same basis as for k-weighting. The selected conditions such as range and weighting were fixed for every sample for proper comparison. A Fourier Transformation needs to be performed on the EXAFS spectra analysis for obtaining further information of local fine structure.

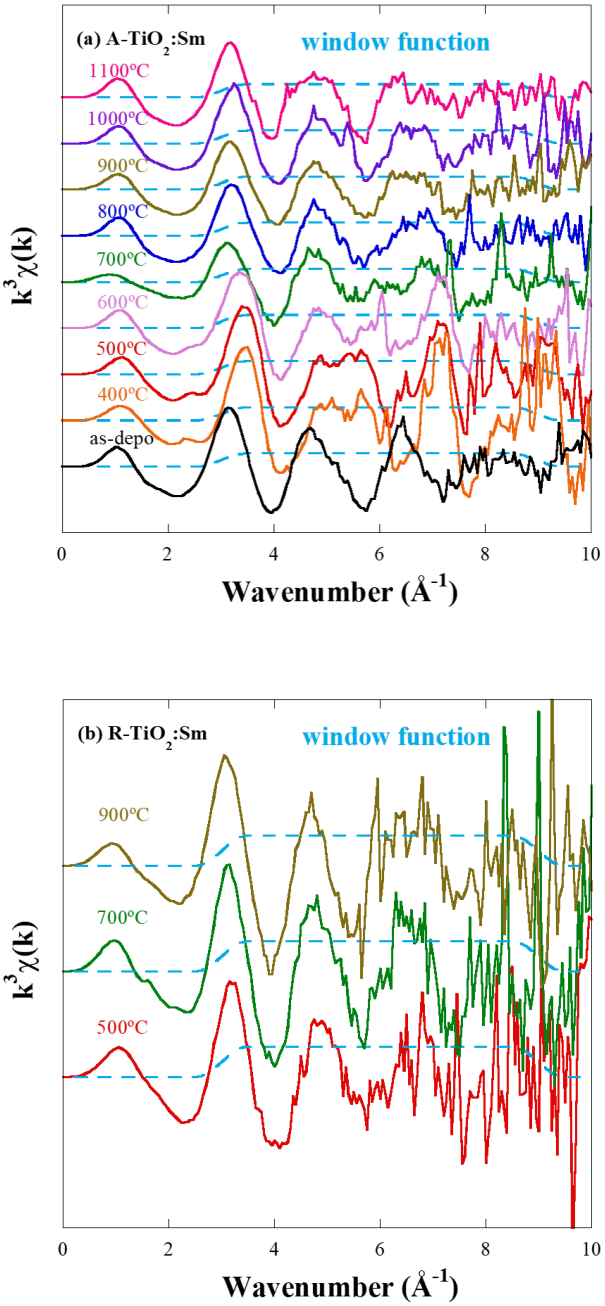

Figure 3.5: EXAFS spectra of (a) A- and (b) R-TiO_2:Sm samples.

The EXAFS spectra shown in Fig. 3.5 were Fourier transformed to radial structural function (RSF) for XAFS analysis using *Athena* and fit using *Artemis* , which are represented in Fig. 3.6, (a) for A- and (b) for R-TiO_2:Sm samples. Note that amplitude (y-axis) of FT XAFS spectra consist of co-ordination numbers of neighbouring atoms and radial distance (x-axis) is simply atomic distance from Sm. RSF XAFS spectra do not take account into some factors such as back scattering factor and Debye-Wallar factor so that radial distance shown in the figure is approximately 0.3 – 0.8 Å shorter than the actual atomic distance with the absorption element. Due to this reason, the curve fitting with theoretically calculated model is needed. A window finction (Hunning) for the curve fitting was performed in a range of 1.00 - 3.29 Å. The areas with shadows in Figs. 3.7 (a) and (b) are excluded for the curve fitting. An EXAFS analysis provides detailed information related to local structure of the absorbing Sm atoms, namely atomic distances and numbers of bonding atoms. This information is obtained from curve fitting for the RSF using theoretical calculation by FEFF programme in order to analyse them[54].

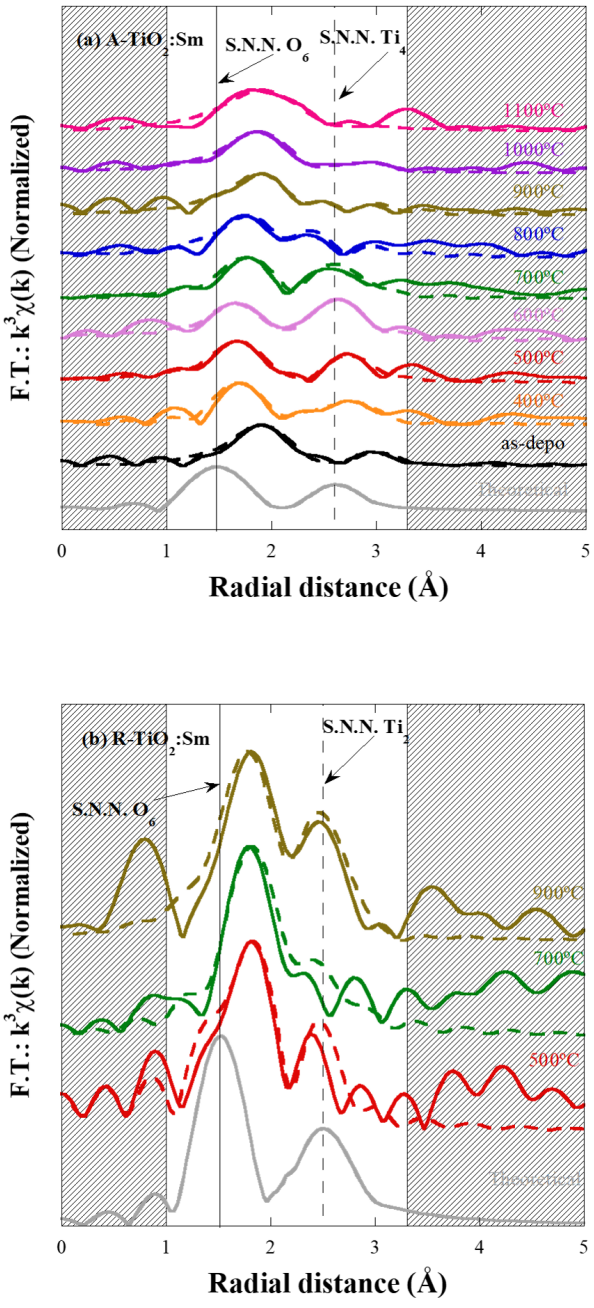

Figure 3.6: Radual structural function and fitting curves of (a) anatase- and (b) rutile-phase TiO_2:Sm Fourier transformed from Fig 3.4.

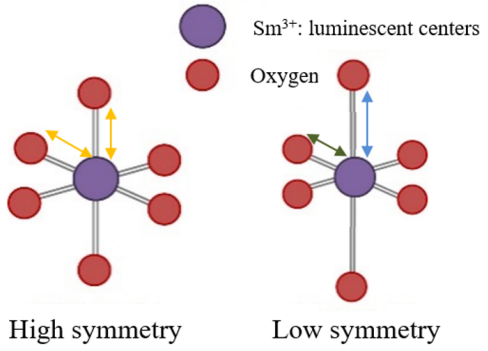

Figure 3.7: Fitting model images for XAFS analysis.

Figure 3.7 illustrates an image of fitting models for XAFS analysis in this study. Two models were prepared for the fitting analysis: highly symmetrical model and low symmetrical model. A high symmetry means that each atom in each nearest neighbour (i.e. 6 O in the first nearest-neighbour, F.N.N.) has the same atomic distance. On the other hand, low symmetrical model has different bond length in each N.N. such as 6 O in the F.N.N. separated into 2 O with shorter atomic distance and 4 O with longer atomic distance. Note that EXAFS spectra in R-space just has 1 dimensional information so that it is difficult to identify the position of shorter or longer neighbouring atoms in the TiO_2 unit cell. If a table with fitting results of XAFS analysis shown as below.

Table 3.1: Example of a XAFS fitting result.

Samples	N	R of the F.N.N. [Å]	R of the S.N.N. [Å]
X	4	2.0 ± 0.01	-
	2	2.4 ± 0.02	-
	2	-	3.2 ± 0.01
	2	-	3.4 ± 0.03

The table means that there are 4 O with shorter (2.0 Å) atomic distance and 2 O with longer (2.4 Å) atomic distance with Sm in the F.N.N.. In S.N.N., there are 2 Ti with shorter (3.2 Å) atomic distance and longer (3.4 Å) atomic distance with Sm in the second nearest-neighbour (S.N.N.).

Table 3.2 describes fitting results of A-TiO_2 samples, where *N* is the number of neighbouring atoms of Sm.The analysis used TiO_2 structure with replaced absorbing element by Sm at the Ti site showed good agreement with all samples and suggested that the F.N.N. of Sm is 6-folded O (O_6) and the S.N.N. is 4-folded Ti (Ti_4) same as the typical TiO_2 crystal structure. The fitting result suggests that change in these neighbouring atomic distances from Sm is correlated with the result of PL measurement: they become shorter with increase of annealing temperature up to 700 °C (the maximum PL intensity was observed for A-TiO_2:Sm), then be back to being the bond lengths as long as for as-depo (no-annealing) again above 700 °C. This correlation is also confirmed in symmetry of co-ordination around Sm^{3+}. The EXAFS fitting revealed that the samples with very weak or no emissions, namely as-depo, 1000 °C and 1100 °C annealed show good agreement with a highly symmetrical model, which means equidistant bond lengths to Sm^{3+} for both O_6 (F.N.N.) and $Ti_4(2)$ (S.N.N.) atoms (2 for 1100 °C sample). Note that 1100 °C was fitted as rutile-phase. On the other hand, a low symmetrical model is suitable for fitting to the samples with emission (varies from weak to intense) for both F.N.N. and S.N.N.. This is exactly the same range of "the window of emitting", the window of annealing temperatures for activation of Sm^{3+} ions to exhibit luminescence, which is the range 400 °C to 900 °C. The low symmetrical model is a fitting model for distorted TiO_2 structure with several atomic distance in each N.N.: the co-ordination

numbers with equidistant bond length divided into co-ordinations with different bond lengths (total co-ordination numbers are still the same). Although each N.N. is split, we still continue to call them F.N.N. and S.N.N.. Namely, the O_6 *of F.N.N.* is divided into O_4-O_2 and the $Ti_4$of S.N.N. is divided into Ti_2-Ti_2. Especially, the analysis revealed that the difference of length between O_4 and O_2 for 600 °C and 700 °C annealed, the two brightest emitting samples, is the largest. These fitting results indicates that increase of annealing temperature distorts the local fine structure of Sm^{3+}, whilist Sm^{3+} ions are activated and exhibit luminescence up to a maximum at 700 °C. Higher annealing temperature leads to a high symmetry structure with weaker emissions and A-TiO_2 transforms to R-TiO_2 in the end. The result also suggests that the local fine structure around Sm^{3+} and atomic distances (Sm-O) are more likely TiO_2 rather than Sm_2O_3 structure despite Ti is replaced by Sm with different ionic radii. Especially, this tendency is predominant with increase of annealing temperature, e.g. for the window of emitting. We can assume from this result that the local fine structure around Sm^{3+} changes from likely Sm_2O_3 structure to TiO_2 structure, then back to Sm_2O_3 structure with increasing annealing temperature and having TiO_2 structural co-ordination around Sm^{3+} is possibly the suitable environment to induce intense emissions.

The fitting results of R-TiO_2 obtained from Fig. 3.6 (b) is shown in Table 3.3. All samples showed good agreement with the high symmetrical model with equidistant bond lengths. Much change is observed neither in symmetry of the local nor bond length with increase of annealing temperature, which is consistent to reports about rare earths-doped oxides [44]. These results indicate that Sm^{3+} ions tend to be more activated in the lower symmetrical structure as the luminescent centre. Also, it is possible

that A-TiO_2 structure is more flexible to accept substituted Sm^{3+} ions than for R-TiO_2.

Table 3.2: Fitting result of A-TiO_2:Sm samples: numbers of neighbouring atoms (*N*) and atomic distances (*R*) [67]. Copyright reserved Wiley-VCH, 2019.

Samples	*N*	*R* of the F.N.N. [Å]	*R* of the S.N.N. [Å]
As-depo	6	2.40826 ± 0.02119	-
	4	-	3.46755 ± 0.07675
400 °C	2	2.13835 ± 0.02201	-
	4	2.19631 ± 0.01386	-
	3	-	3.15581 ± 0.02234
	1	-	3.23131 ± 0.09661
500 °C	2	2.19174 ± 0.02500	-
	4	2.21986 ± 0.02906	-
	4	-	3.19746 ± 0.01146
600 °C	4	2.24929 ± 0.01355	-
	2	2.43859 ± 0.02731	-
	2	-	3.19493 ± 0.00987
	2	-	3.43886 ± 0.02753
700 °C	4	1.97239 ± 0.05379	-
	2	2.28126 ± 0.05379	-
	2	-	3.02660 ± 0.01626
	2	-	3.15415 ± 0.01207
800 °C	4	2.32631 ± 0.01100	-
	2	2.46089 ± 0.04263	-
	2	-	3.2035 ± 0.02062
	2	-	3.33798 ± 0.02005
900 °C	4	2.35694 ± 0.01140	-
	2	2.44638 ± 0.01652	-
	2	-	3.13560 ± 0.02310
	2	-	3.33798 ± 0.02058
1000 °C	6	2.37844 ± 0.01915	-
	4	-	3.37454 ± 0.07675
1100 °C	6	2.43582 ± 0.01132	-
	2	-	3.37989 ± 0.01564

Table 3.3: Fitting result of R-TiO_2:Sm samples: numbers of neighbouring atoms (*N*) and atomic distances (*R*) [67]. Copyright reserved Wiley-VCH, 2019.

Samples	*N*	*R* of the F.N.N. [Å]	*R* of the S.N.N. [Å]
500 °C	6	2.30849 ± 0.0095	-
	2	-	3.02595 ± 0.02389
700 °C	6	2.33218 ± 0.01478	-
	2	-	3.11809 ± 0.002913
900 °C	6	2.30963 ± 0.01003	-
	2	-	3.09122 ± 0.01386

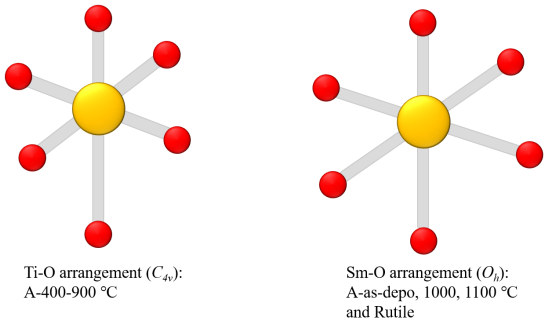

Figure 3.8: Images of predominant bonding arrangement for TiO_2:Sm samples with different crystalline phases/annealing temperatures considered based on *rack and pinion effect* theory.

Microscopic properties of both the host semiconductors and electronic state around doped rare earth determine the optical properties (resulting intra-4*f* transition): an actual rare earth-O cluster in a semiconductor has 6-folded co-ordination (O_6) with high symmetry. However, the crystal field with the highest symmetry (i.e. O_h point group) cannot form the electronic state, even though an octahedron is the simplest 6-folded structure and easy to form. Ishii et al reported the theoretical prediction for

this relationship between the tendency of forming high or low symmetrical structure affected by the crystal field and luminescence intensity supported by the result of the first-principles [69]. An optically activated ErO_6 (Er: erbium, 68, one of the rare earth elements which show emissions in green, red and infra-red wavelength regions) cluster has a stable pseudo-octahedral structure with distortion (C_{4v} symmetry), which is sufficiently smaller than the typical rare earth-O bond length. And the Er distortion from the octahedron rotates the O 2*p* atomic orbital. In A-TiO_2:Er, the Er-O bond was unstable with the structure of Ti-O arrangement (the host crystal-related and more distorted than Er-O arrangement) rather than the chemical properties of Er-O (original structure of the Er-O cluster). Whilst in R-TiO_2:Er with showing weak PL emissions was decided by the Er-O chemical properties (high symmetry) rather than the Ti-O arrangement. Note that both A- and R-TiO_2:Er samples were annealed at optimal annealing temperature (800 °C) for optical activation of Er. The rack and pinion effect yielding a spontaneous symmetry reduction which strengthens the Er-O ionic bond and Ti-O arrangement. A-TiO_2 prevents the rack and pinion effect resulting an unstable Er-O resulting forming the electronic state and stimulating optical activation of Er. In R-TiO_2, because the rack and pinion effect is induced, ErO_6 is stabilised in the host crystal [65].

This *rack and pinion* and *spontaneous symmetry reduction* theories predicted by Ishii et al support our results: although the bondings between Sm and O (also Ti and O) were separated by a laser ablation, Sm exists in TiO_2 matrix as SmO_6 which has a stable pseudo-octahedron structure (Sm-O is predominant, Fig 3.8). This structure is kept even in as-deposited sample for both A- and R-TiO_2:Sm. In A-TiO_2 sample, a stable

octahedron structure is influenced by annealing and distorted as Ti-O arrangement with an increase of annealing temperature. Above 700 °C (maximum PL intensity was observed for A-TiO_2:Sm), the kinetics of annealing are used for the phase transition from anatase to rutile (possibly there are clusters with the mixture of anatase and rutile phase), so that Sm-O arrangement becomes predominant. On the other hand, Sm-O arrangement is always dominant in R-TiO_2:Sm at any annealing temperatures because the rack and pinion effect is smoothly induced.

3.4 Conclusion

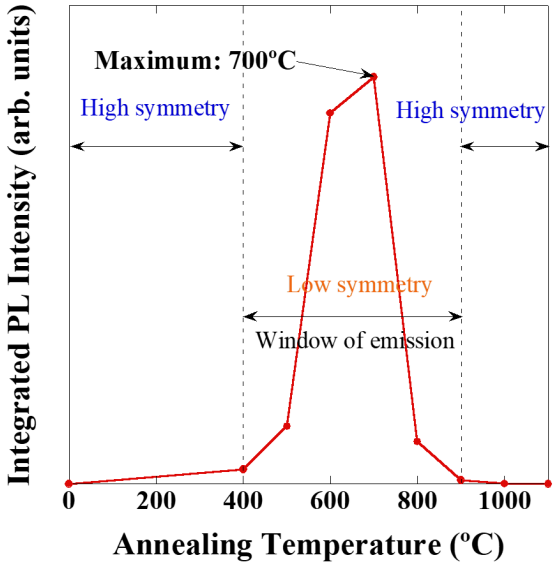

Figure 3.9: A correlation between luminescent and local fine structural properties of A-TiO_2.

Thin films of A- and R-TiO_2:Sm were prepared by laser ablation. An O_2 pressure in the growth chamber was carefully controlled for selecting their crystalline phase, and the result of XRD confirmed that they are properly prepared with selected crystalline phase as intended. From PL measurements, the typical emissions from intra-4*f* transitions in Sm^{3+} were observed from every sample. The PL intensity of A-TiO_2:Sm samples substantially more intense than that for R-TiO_2:Sm samples, which was ap-

proximately 200 times stronger at a maximum. For a series of A-TiO_2:Sm, the intensity of the PL emission from Sm^{3+} gets stronger with increase of annealing temperature up to 700 °C, whereas the luminescence dramatically quenches above that annealing temperature. Differences appeared in the PL fine structure between A- and R-TiO_2:Sm suggests differences of the crystal filed (environment around Sm^{3+} ions) affecting the parity for wavefunctions in configurations determines the transition probability. Based on this result, XAFS measurements were performed to confirm the local fine structure around Sm^{3+}. For the A-TiO_2:Sm samples with the most intense PL emission such as 600 °C or 700 °C annealed, distances between Sm and the first and second nearest-neighbour atoms (Sm-O and Sm-Ti) are shorter, and co-ordination numbers are divided with different distances. They showed good agreement with a low symmetrical model (distorted model) with TiO_2 crystal structure. The samples annealed above 700 °C fit to a high symmetrical model with equidistant bond length, which is consistent to the quenched PL emissions. For the samples with either very weak emissions or no emissions namely, as-deposited, 1000 °C and 1100 °C annealed A-TiO_2:Sm samples and all R-TiO_2 samples are in good agreement with the high symmetrical model. This result suggests that for A-TiO_2:Sm, the distorted co-ordination around Sm^{3+} (low symmetry) caused by annealing is responsible for enhancing emissions (Fig. 3.9). It is possible that A-TiO_2 structure is flexible for accepting Sm^{3+} dopant to become suitable environment by annealing for activation of Sm^{3+}. The highest annealing temperature make phase transition from anatase to rutile, which leads to quenching of emissions and increasing the symmetry. The EXAFS analysis indicates that distortions in the S.N.N. is also probably essential in activation of Sm^{3+} ions. In this chapter, quantitative and highly

accurate estimations of local fine structure of Sm^{3+} was successfully performed. In addition, this is the first time to achieve quantitative, metrical and accurate estimations of the second nearest neighbour of rare earth ions. We can expect that this expands discussions of energy transfer. Distortion occurring in the second nearest neighbour of rare earth is possibly a better environment for enhancing energy transfer. Because the intermediate state can exist near the second nearest neighbour (Ti) of rare earth and distortion (or optimal bond length) introduces better potential valleys for energy transfer.

Chapter 4

Influence of Al co-doping on Nd-doped TiO_2

4.1 Introduction

Co-doping is other approach to enhance rare earth luminescence. Some of elements were co-doped into rare earth-doped phosphors to stimulate their emissions namely, bismuth (Bi), aluminium (Al), silver (Ag) and ytterbium (Yb) [39, 70, 71, 72, 73]. Mainly these co-dopants are trivalent and they lead to O ligand distortion and/or dissolution of rare earth clusters. Increase of radiative relaxation via energy transfer can be expected because of these effects.

In this chapter, effect of Al co-doping on luminescence property of TiO_2:Nd and its local fine structure are shown. Especially, directly and indirectly excited PL results are

discussed. Direct excitation PL is excitation of rare earth ions without going through a host material, whereas indirect excitation is *host meditate* excitation through the energy transfer process. PL spectra measured by direct excitation PL is still affected by the crystal field of a host material, however we can compare the difference of effect of excitation energy between direct and indirect excitation from PL spectra.

4.2 Experimental details

Please find sample preparation details discussed in Section 2.6, Chapter 2. Prepared samples are Nd-doped and Nd-Al-co-doped TiO_2 thin films (TiO_2:Nd/TiO_2:Nd:Al) annealed at 500 °C for 3 minutes. Variations of Al concentration are 0.1, 1.0 and 5.0 wt% (0.08, 0.8 and 3.9 at%)

The crystalline phase of samples is unified as anatase-TiO_2 since an effect of Al co-doping is focused this time. X-ray diffraction (XRD) was carried out for identification of crystalline structure and calculating grain size of the samples. The thickness of the thin films was approximately estimated to be 800 nm from interference of thin film by an optical microscope.

Luminescence properties with different route to excite luminescence centre of the thin films were investigated by PL measurements with a He-Cd laser (325 nm) and a laser diode (785 nm) were used to excite Nd^{3+} ions via host/directly. N_2-cooled Ge p-i-n detector and monochromator (Ritu oyo kogaku, MC-25NP) and lock in amplifier were used to collect signals from the Nd^{3+} ions, which show luminescence in infrared

wavelength region. Wavelength was calibrated by a Hg lamp and a spectral resolution of 4 nm with the entrance slit set at 0.7 mm. PL time response was measured using the 4th harmonic of Q-switched YAG laser (266 nm, 0.1 mW/cm^2, 300 ps) was used for excitation of the Nd^{3+} ions. A photomultiplier tube (PMT) was used for detecting the luminescence. X-ray absorption fine structure (XAFS) measurement was performed at High Energy Accelerator Research Organization, Photon Factory BL-9C, in Tsukuba prefecture, Japan. A Si(111) double-crystal was used to monochromatise the synchrotron radiation (SR) beam. A seven-element silicon drift detector was used for counting photon counts of the fluorescence X-rays. XAFS analysis was performed using *Athena* and *Artemis* of Demeter by Bruce Ravel [54].

4.3 Results and discussion

4.3.1 XRD measurements and grain size estimations for TiO_2:Nd as a function of Al concentrations

XRD patterns for the TiO_2:Nd/TiO_2:Nd:Al samples are shown in Fig. 4.1 (a). All peaks correspond to anatase-phase TiO_2 crystal structure, which confirms that the samples are properly prepared with intended crystalline phase. Figure 4.1 (b) illustrates the grain size of crystal derived from a Scherrer analysis of the (101) diffraction peaks (the full width at half maximum of the XRD line) presented in Fig 4.1 (a). Note that Si-related peak at 33.3° was removed for emphasising TiO_2-related peaks. Grain size of all samples were calculated to be approximately 55 to 60 nm. Small decrease of grain size was confirmed with the highest Al co-doping sample. This seems the small change, however this result suggests that crystallising large crystal of host material replaced by rare earth ions might be naturally prevented by increase of Al concentration. It is possible that the grain boundary limits diffusing Nd^{3+} ions with the treatment at relatively high annealing temperature.

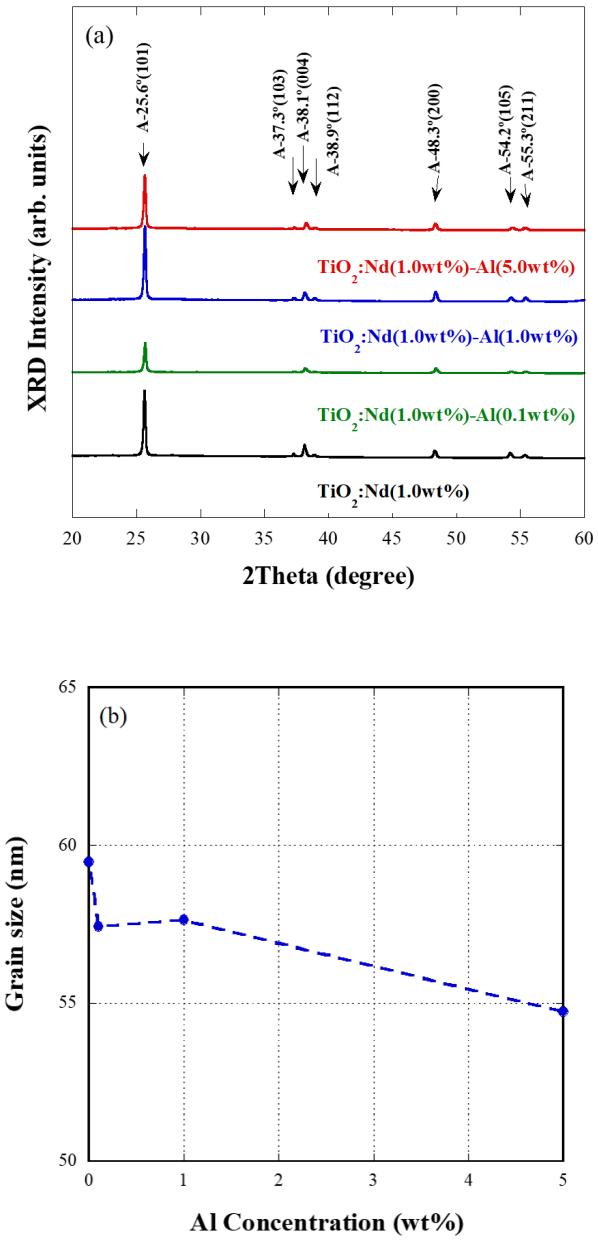

Figure 4.1: XRD patterns of (a) TiO_2:Nd:Al (0, 0.1, 1.0, 5.0 wt%) and (b) grain size [75].

4.3.2 Indirect and direct excitation of PL measurements for TiO_2:Nd as a function of Al concentrations

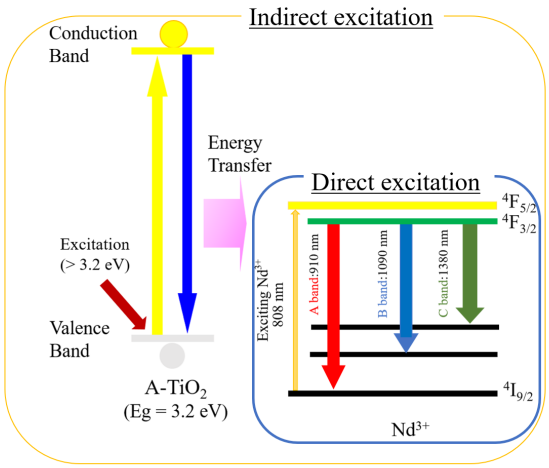

Figure 4.2: Schematic diagram of indirect and direct excitation processes.

Now, we compare PL properties of indirect excitation to direct excitation. Figure 4.2 illustrates a process of exciting rare earth in indirect and direct excitation. The process of the indirect excitation of Nd^{3+} ions means that generated electron-hole pairs in the TiO_2 host by photo-excitation of 325 nm recombine and transfer this energy for Nd^{3+} excitation. On the other hand, the process of the direct excitation is that Nd^{3+} ions simply absorb a 785 nm excitation energy directly, which is close to the energy between the ground state and inner-4*f* ($^4F_{5/2}$, 808 nm) level of the Nd^{3+} [74].

Figure 4.3 demonstrates (a) indirectly excited (host meditated) and (b) directly excited (resonant) PL spectra for TiO_2:Nd/TiO_2:Nd:Al samples as a function of the Al concentration measured at room temperature. The luminescence from Nd^{3+} excited by either of these excitation route originates from $^4F_{3/2} \rightarrow {}^4I_J$ (J = 9/2, 11/2, 13/2)

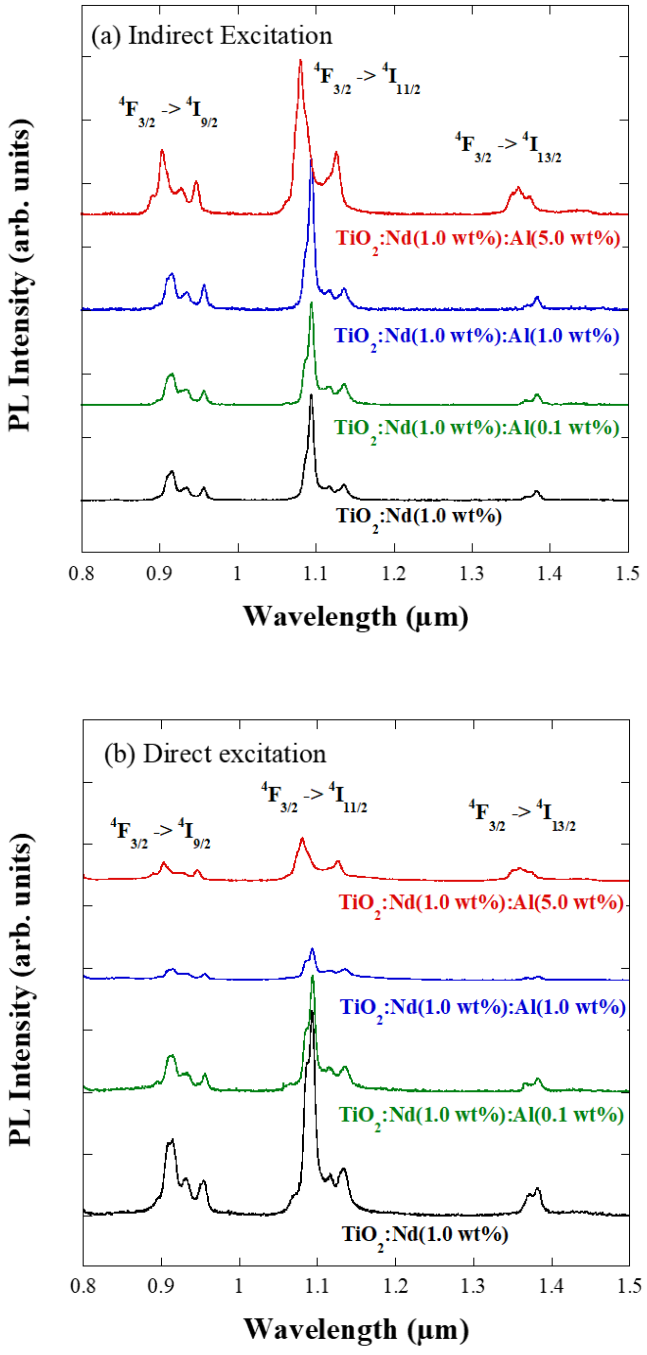

Figure 4.3: (a) Indirectly and (b) directly excited PL spectra of TiO_2:Nd:Al(0, 0.1, 1.0, 5.0 wt%) [75].

transitions of Nd^{3+}. Note that peaks without assignment of transition are transitions caused by Shtark effect. For the indirectly excited PL spectra in Fig. 4.3 (a), a peak shift, change in spectral shape and enhancement of PL emission with increase of Al concentration are observed, especially for the TiO_2:Nd:Al (5.0 wt%) sample. This result suggests that co-doping Al works as the sensitiser for the emissions, and changed the local fine structure (crystal field) around Nd^{3+}, hence PL characteristics of Nd^{3+} such as peak position and PL fine structure are affected and broadened. We can assume that the shifted/broadened sample has Nd^{3+} ion centre with electronic state (ground-excited energy band) consisted of several slightly different wavelengths. For this reason, it is worth analysing the local fine structure around Nd^{3+} to examine a difference.

On the other hand, for the directly (resonantly) excited PL spectra, Nd^{3+}-related emissions are suppressed by the Al co-doping and quenched with increasing Al concentration. This is due to selecting one wavelength of Nd^{3+} energy state, which is close to the excitation wavelength (785 nm) to be resonant. This result indicates that the pure Nd^{3+} centres (808 nm) are decreased with the co-doping Al, and each ground-excited transitions of Nd^{3+} centres become a mixture of various slightly different wavelengths (pure and affected), the same reason of causing a peak shift and change in spectral shape in the indirectly excited PL spectra. The reason why the indirect excitation of PL shows strong emissions and increases PL intensity is that the excitation energy is higher than that for one ground-excited state of Nd^{3+}. A route of the indirect excitation is considered as follows: 1. Excitation of host material, 2. Recombination of electrons and holes, 3. Recombination energy transfers to rare earth ions for exciting them. Therefore, the indirect excitation should cover with a range of wavelengths to

excite more electrons assigned to slightly different ground-excited state transitions more efficient than the direct excitation.

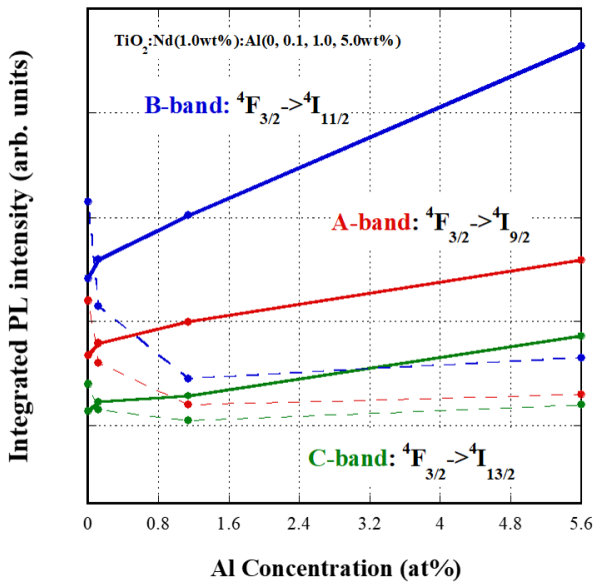

Figure 4.4: Integrated indirectly and directly excited PL intensity of TiO_2:Nd:Al(0, 0.1, 1.0, 5.0 wt%).

The integrated (a) indirect and (b) direct excitation PL intensity obtained from Figs. 4.3 (a), (b) are represented in Figs 4.4 (a) and (b). Note that an y-axis is in linear scale and directly excited PL intensity is amplified 100 times for comparison. The result suggests that indirect (direct) excitation PL intensity increases (decreases) with increasing Al concentration although the number of Nd^{3+} ions are not changed. For the indirect excitation PL intensity is approximately 450 to 600 times stronger in every transitions of Nd^{3+} ($^4F_{3/2} \rightarrow {}^4I_{9,11,13/2}$) than that for the direct excitation. These results reveal that the presence of Al co-dopant affects the structure or in other word, the ratio of

pure to impure Nd^{3+} centres, which determine the $^4F_{5/2}$-Nd^{3+} level: The broadening peaks corresponding to each transition suggests that there is various slightly different wavelengths in the transition, which is due to the different local structure around Nd^{+3}, and that is the reason being the efficient indirect excitation and the inefficient direct excitation.

4.3.3 PL lifetime measurements for TiO_2:Nd with concentrations of Al

Figure 4.5 (a) illustrates the PL time responses for the $^4F_{3/2} \rightarrow {}^4I_{9/2}$ transition of Nd^{3+}. The measurements were carried out at room temperature, and the PL rise time, τ_r (in upper panel) and decay time, τ_d (in lower panel) were detected after 266 nm excitation. The obtained PL transient data were analysed by double exponential curve fitting, representing lifetimes in Fig. 4.5 (b). Curve fitting was undergone as follows: $I(t) \sim A\ exp(-t/\tau_d) - B\ exp(-t/\tau_r)$, where $I(t)$ refers to PL intensity, A and B are pre-exponential constants and τ_d (τ_r) are the decay (rise) times. The measured τ_d in the first term originates from both the radiative (τ_R) and non-radiative (τ_{NR}) recombination; $1/\tau_d = 1/\tau_R + 1/\tau_{NR}$. Whereas, the second term is attributed to the excitation through energy transfer [77]. The characteristics of PL lifetimes obtained from the analysis reveal that both τ_d and τ_r increase with increase of Al concentration. Increasing in τ_d indicates reduction in the contribution of the τ_{NR} term. Generally, τ_R is much longer than τ_{NR}, particularly for rare earth-related transitions [78]. Therefore, suppression of the recombination probability of non-radiative might induce increasing

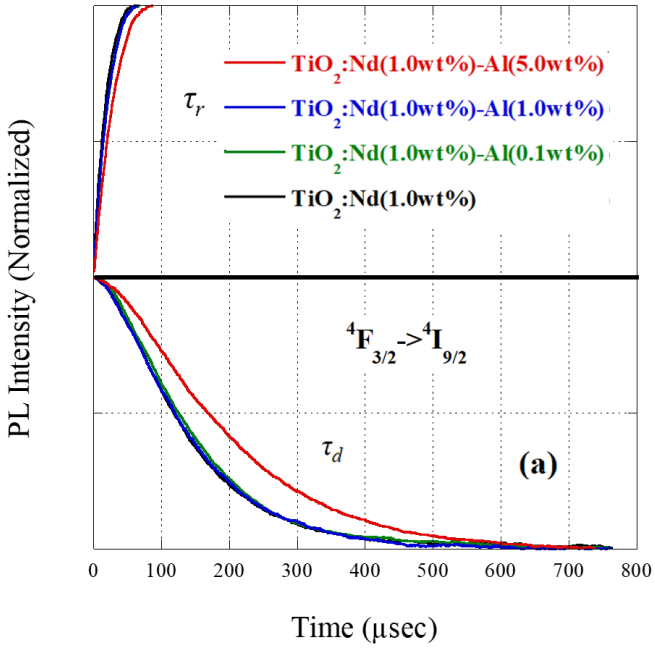

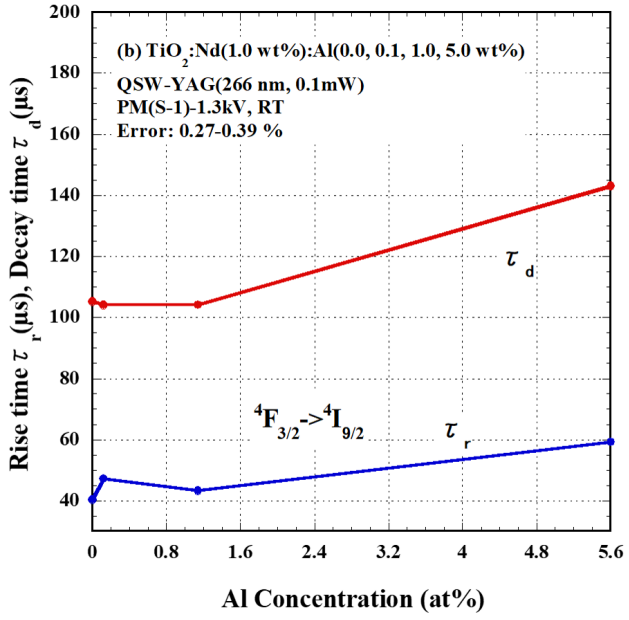

Figure 4.5: (a) Time response PL spectra and (b) PL lifetime of TiO_2:Nd:Al(0, 0.1, 1.0, 5.0 wt%) [75].

τ_d with increasing PL intensity. On the other hand, increasing τ_r with increase of Al concentration suggests an excitation pathway between the $4f$ electrons in Nd^{3+} ions and excitation electron-hole pairs in TiO_2 host. These results indicate that the co-ordination (environment) around Nd^{3+} ions is changed by a co-doping Al, which leads to shifting/broadening/enhancing of the PL spectra from Nd^{3+} transitions and longer lifetimes.

4.3.4 Local fine structure analysis around Nd^{3+} in TiO_2 with concentrations of Al

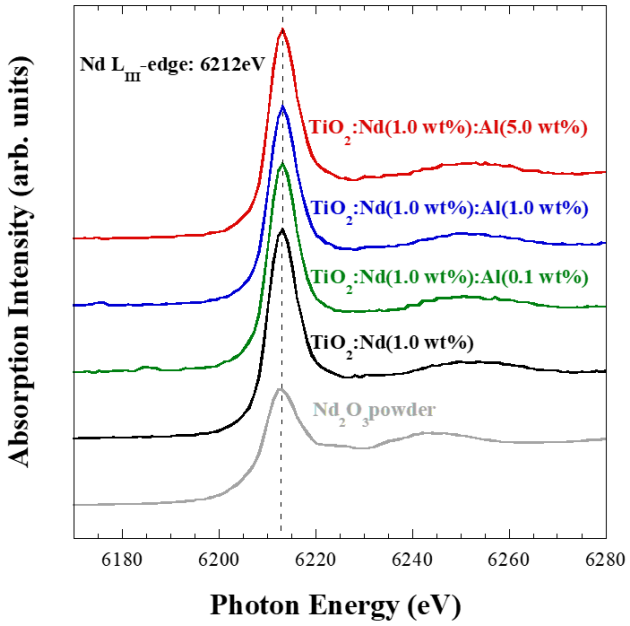

Figure 4.6: XAFS spectra of TiO_2:Nd:Al(0, 0.1, 1.0, 5.0 wt%) [76].

Figure 4.6 demonstrates XAFS spectra at Nd L_{III} - edge of TiO_2:Nd and TiO_2:Nd:Al

samples. The spectra shown in the lowest is a standard sample, Nd_2O_3 powder, measuring for identification of ionisation. The absorption peak of XAFS spectra appeared around 6212 eV arises from $2p$-$5d$ transition of Nd^{3+}, which provides information about its electronic and oxidisation state. Every peak showed its peak in the same position of Nd_2O_3 powder, which typically includes trivalent (3+) ionised Nd ions. This result suggests that doped Nd was properly formed as Nd^{3+} in the TiO_2 matrix.

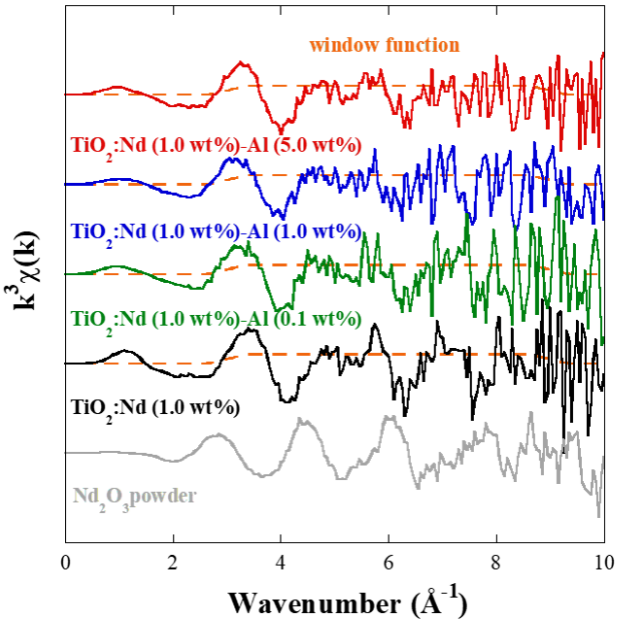

Figure 4.7: EXAFS spectra of TiO_2:Nd:Al(0, 0.1, 1.0, 5.0 wt%) [76].

Figure 4.7 shows k^3-weighted extended X-ray absorption fine-structure (EXAFS) spectra for the XAFS spectra shown in Fig. 4.6. We selected k^3 because measured EXAFS spectra were reasonably clear until 6.0-8.0 $Å^{-1}$. A window function was performed in the range of 3.0-9.0 $Å^{-1}$, dk = 0.5, chosen on the same basis as for

k-weighting. In order to compare properly, the selected conditions such as range and weighting were fixed for every sample. A Fourier Transform (FT) will be performed on the EXAFS spectra for analysis to obtain further information of local fine structure.

A Fourier Transform was performed for XAFS analysis to obtain detailed information about the local fine structures of Nd^{3+}, absorption element of those measurements, such as the co-ordination numbers and atomic distances. Radial structural functions (RSF) around Nd^{3+} obtained by the FT XAFS spectra for the TiO_2:Nd/TiO_2:Nd:Al samples and their fitting curves are illustrated in Fig. 4.8. Note that amplitude (y-axis) of FT XAFS spectra consist of co-ordination numbers of neighbouring atoms and radial distance (x-axis) is simply atomic distance from Nd. FT XAFS spectra do not take account into some factors such as back scattering factor and Debye-Wallar factor so that radial distance shown in 4.8 is approximately 0.3 – 0.8 Å shorter than the actual atomic distance with the absorption element. Due to this reason, the curve fitting with theoretically calculated model is needed. The simulated theoretical spectrum calculated by the FEFF programme using the information of typical anatase-phase TiO_2 with substituted Ti by Nd (absorption element) was shown in the lowest. Note that theoretical curves do not look the same as the fabricated samples however, theoretically, both of them are in the same crystal structure. A window finction (Hunning) for the curve fitting was performed in a range of 1.00 - 3.0 Å. The areas with shadows in Fig. 4.8 are excluded for the curve fitting. We prepared the simulated theoretical calculations for anatase-phase TiO_2 and Nd_2O_3 structure, however as seen in Fig. 4.8, although the peak position was shifted from the theoretical, anatase-phase TiO_2 structure was suitable for fitting the prepared samples. The result of curve fittings indicated that the first nearest neighbour

(F.N.N.) is 6 oxygen atoms (O_6) and the second nearest neighbour (S.N.N.) is 4 Ti atoms (Ti_4) as the typical anatase-phase TiO_2. The substantial peak shifts are observed in the samples with increase of Al concentrations.

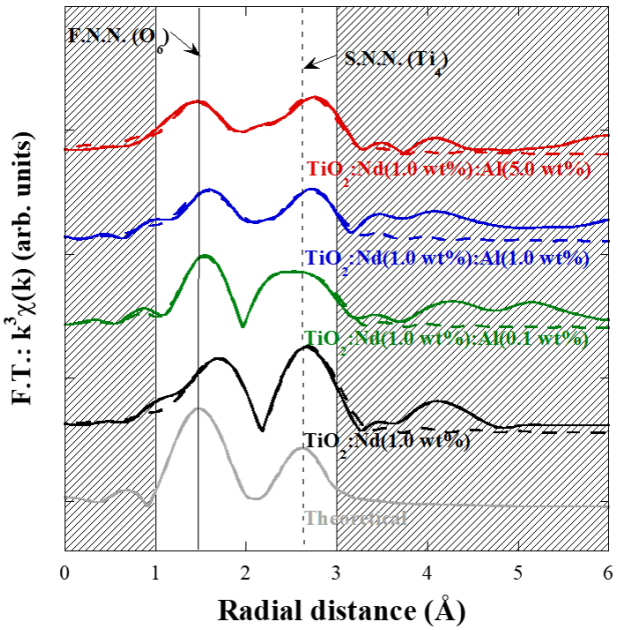

Figure 4.8: Radual structural function and fitting curves of TiO_2:Nd:Al(0, 0.1, 1.0, 5.0 wt%) Fourier transformed from Fig 4.6.

Table 4.1 shows the characteristics of the local fine structure namely, number of neighbouring atoms *N* and atomic distances of TiO_2:Nd/TiO_2:Nd:Al. Typical anatase-phase TiO_2 crystal structure with Ti replaced by Nd was used as the basic fitting model for the starting point. Please find an explanation about a table with XAFS fitting results in Section 3.3.3, Chapter 3 if you find a difficulty to understand meaning of a table. Every sample is in good agreement with specified neighbour atoms, however co-ordination

numbers did not fit properly with the samples with Al. This indicates that Al co-doping is attributed to distortion (low symmetry) of both the F.N.N. and the S.N.N.. For the identification of co-ordination numbers and atomic distance, several fitting models with distortion (low symmetrical model) were calculated, which have separated paths, for instance, the separated co-ordination numbers of 6 (O_6) into (O_{2-4}). For TiO_2:Nd:Al (0.1 wt%), its curve was fit with an O_{5-1} (separated from O_6) and Ti_{1-3} (separated from Ti_4) model. In contrast, lower symmetrical model of O_{1-4-1} and Ti_{2-2} fit with co-doped heavier Al samples, TiO_2:Nd:Al (1.0 and 5.0 wt%). An estimated error about $\pm$ 1.7 % suggests that accuracy of the fittings was reasonable.

Table 4.1: Fitting result of TiO_2:Nd:Al(0, 0.1, 1.0, 5.0 wt%): numbers of neighbouring atoms (*N*) and atomic distances (*R*) [76].

Samples	*N*	*R* of the F.N.N. [Å]	*R* of the S.N.N. [Å]
TiO_2:Nd	6	2.2320 ± 0.00678	-
	4	-	3.2299 ± 0.00574
TiO_2:Nd:Al (0.1 wt%)	5	2.13018 ± 0.00199	-
	1	2.26395 ± 0.00243	-
	1	-	2.94175 ± 0.00677
	3	-	3.18274 ± 0.00243
TiO_2:Nd:Al (1.0 wt%)	1	1.96550 ± 0.03537	-
	4	2.19452 ± 0.01935	-
	1	2.30186 ± 0.01268	-
	2	-	3.01373 ± 0.00529
	2	-	3.20950 ± 0.00798
TiO_2:Nd:Al (5.0 wt%)	1	2.02450 ± 0.02045	-
	1	2.13104 ± 0.00550	-
	4	2.29404 ± 0.02421	-
	2	-	2.8785 ± 0.00858
	2	-	2.95919 ± 0.00868

Now we consider this result based on the Bohr radius of the ground state of hydrogen [5]. a_d can be written using the effective mass and electron affinity of TiO_2 as follows:

$$a_d = \frac{4\pi\epsilon\hbar^2}{m_e e^2} = (\frac{0.53\epsilon}{m_e/m}) = (\frac{0.53 \times 25.44}{0.4m_0}) = 33.7\text{Å}. \tag{4.3.1}$$

This simple calculation showed in Table 4.2 suggests that the wave function of Al and Nd would be overlapped for Al 1.0 wt% co-doped sample and higher concentration of that. In addition, the atomic distance between Al and Nd can be 2.4 nm. This calculation supports the fitting result: distorted local fine structure can be seen especially for Al 1.0 and 5.0 wt% co-doped samples.

Table 4.2: Calculated probability of existance for Nd and Al atoms in TiO_2 unit cells (/cm^3).

Al	Nd/cm^3	vs Ti	Al/cm^3	vs Ti
-	2.5×10^{20}	1:34	-	
0.1 wt% (0.08 at%)		1:34	3.7×10^{19}	1:231
1.0 wt% (0.8 at%)		1:34	3.7×10^{20}	1:23
5.0 wt% (3.9 at%)		1:34	1.9×10^{21}	1:5

These results indicate that low symmetrical Ti and O-atomic bonds by Al co-doping are responsible for increase of PL intensity in these samples. It is clear that the consistency between the longest O_4 in the F.N.N. with the shortened Ti_{2-2} in the S.N.N. of TiO_2:Nd:Al (5.0 wt%) introduced by Al co-doping, which can set the peak shift/broadening of PL spectra. Still, it is unclear from these results to identify where the Al co-dopant exists. There are two models to be considered; 1. Some of Ti site are substituted by Al or 2. Interstitial site between bonds. For elucidating the occupied

site by Al in the TiO_2 matrix, further XAFS measurements at the Al *k*-edge are required.

4.4 Conclusion

Thin films of anatase-phase TiO_2:Nd and TiO_2:Nd with co-doped Al (0.1, 0.5 5.0 wt%) were fabricated on Si(100) substrates by laser ablation. The samples were post annealed for optical activation of Nd^{3+} ions and formation of nano-meter sized TiO_2 crystals. The grain size of samples slightly became smaller with increasing Al concentrations. This result indicates the possibility that co-doped Al in TiO_2 matrix tends to prevent forming large crystal of substituted Nd^{3+} ions. Indirectly excited (host meditated, via host) PL results for TiO_2:Nd/TiO_2:Nd:Al samples showed strong luminescence originates from inner-4*f* transitions of Nd^{3+} in the near-IR wavelength region. Interestingly in contrast, for directly excited (resonant) PL measurements for the samples, very weak PL spectra were observed. PL intensity became more intense for indirectly excited PL with increase of Al concentration, whereas PL intensity under direct excitation decreased with Al co-doping. Al co-doping is effective to enhance the luminescence from Nd^{3+} ions under indirect excitation. Moreover, peak shift and change in spectral shape were observed for all Al co-doped samples, especially for the heaviest Al concentration. The result indicates that co-doping Al changes crystal field around Nd^{3+}, which determines the transition probability of the luminescent centre, changing the PL fine structure. These results suggests that co-doped Al decreased the number of pure (808 nm) Nd^{3+} centres and made a mixture of various Nd^{3+} centres

and pure Nd^{3+} centres. This makes the indirect excitation efficient, whereas direct excitation becomes inefficient because direct excitation just select one wavelength of a ground-excited band of Nd^{3+} from various slightly different Nd^{3+} centres. PL time response showed the rise and decay lifetimes were increased with increasing Al concentration, suggesting a reduction in non-radiative recombination, which is consistent to the more intense PL intensity.

XAFS measurements and theoretical analysis revealed the F.N.N. and S.N.N. in Nd^{3+} as 6 O atoms and 4 Ti atoms. A highly symmetrical model with O_6 , Ti_4 was in good agreement with TiO_2:Nd sample. O_6 and Ti_4 were separated into several paths with increasing Al concentration. For instance, for TiO_2:Nd:Al (5 wt%), the sample with the highest Al concentration, O_6 separated into O_{1-4-1} (the F.N.N. consisted of 3 atomic distances), and Ti_4 divided into Ti_{2-2} (the S.N.N. consisting of 2 atomic distances). These results suggest that distortion (decreased symmetry) in the F.N.N. and the S.N.N. was caused by the presence of co-doped Al. It has been reported that distortion in the F.N.N. is responsible for strong PL emissions, however these results reveal that distortion in the S.N.N. is also important, and it possibly causes the distortion in the F.N.N.. Al co-doping in rare earth-doped oxides is possible to improved opto-electronic materials for application to devices.

Chapter 5

Electrical property of TiO_2:Sm on $SrTiO_3$:Nb

5.1 Introduction

We discussed optimisation of rare earths-doped TiO_2 samples for luminescent enhancement by synthesis and co-doping throughout this thesis. However, either of these focuses on the process of *excitation to emission*. This is critical for luminescence, but at the same time, it is difficult to improve further more than these. Since the final *aim* of this project is surely application of rare earth-doped TiO_2 to LEDs, we focus on the electrical property of our samples to study deep level defect states in our samples and to understand what is a key point to enhance the emission via a bias. As discussed in Chapter 1, the excitation process of rare earth-phosphor semiconductors is

complicated. The wavelength of an excitation source is selected based on the energy gap of a host semiconductor. First, the host semiconductor is excited by the excitation source and recombination energy of electron-hole pair goes to excite rare earth (luminescent centre). This is so-called *energy transfer*. Energy transfer is still unclear although rare earth phosphors have been studied for very long time. We assumed that deep level states in rare earth-doped semiconductors play a significant role for energy transfer because there should be an intermediate state with high enough energy. This is on going project so that we give a brief summary of electrical property of TiO_2:Sm is shown in this chapter.

Niobium-doped TiO_2 has received attention as a transparent conductive layer for recent years [79, 80, 81]. Because TiO_2 is relatively resistive semiconductor, electrical property of with and without Nb-doped TiO_2:Sm samples to be discussed.

5.2 Experimental details

Sample preparation details are summarised in Section 2.6, Chapter 2. Ru and Au were deposited on the TiO_2:Sm or TiO_2:Sm:Nb surface by laser ablation and evaporator. Diameter of Schottky contact is 0.5-1 mm. Fror Ohmic contact, Ti was sputtered on the TiO_2 surface. A work function of metals and an electron affinity of TiO_2 are discussed in Section 2.5.1, Chapter 2.

X-ray diffraction (XRD) was used to subject all samples to structural determination and calculate grain size. Scanning Electron Microscope (SEM) is used for surface observations. I-V and C-V measurements were carried out for characterisation of elec-

trical property of samples.

5.3 Results and discussion

5.3.1 Resistivity of TiO_2:Sm (laterally and vertically applied voltage)

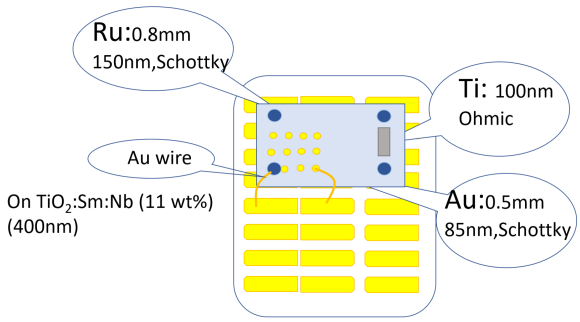

Figure 5.1: Schematic of sample structure (Lateral).

Firstly, a sample with Ohmic contact (Ti) and Schottky contacts (Ru, Au) on the surface was prepared for simple characterisation of TiO_2:Sm:Nb thin film on Si(100) substrate. We tried this *lateral* structure first because DLTS measurement can be difficult due to mismatch of interface. Figure 5.1 shows lateral sample structure. A probe for connecting Schottky contact was set on an Au plate on a ceramic substrate. Sample was glued on a ceramic substrate with Au plates with Ag paint and Schottky contacts were wired to Au plates with an Au wire to prevent damage of putting probes.

Figure 5.2 illustrates I-V curves for TiO_2:Sm:Nb with different Schottky contacts

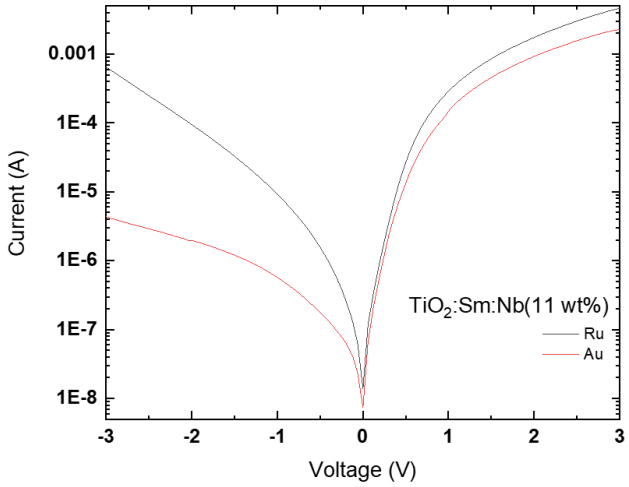

Figure 5.2: I-V result for TiO_2:Sm with Ru and Au Schottky diodes.

(Ru/Au). Au contact showed relatively good rectification, however, the value varied and depended on the position of contacts on sample. One of the issues to fabricate thin films using laser ablation is that roughness of the thickness of thin films. For estimating roughness and finding the reason of causing this, I-V measurements between 90 Ti dots were carried out.

Figure 5.3 (a) shows schematic of sample structure for this measurement. I-V result is described in Fig. 5.3 (b) with the image of the sample. Resistivity was calculated from I-V results and plotted as 3D image. Increase of resistivity is consistent with shifting the colour of thin film. Red is thicker than blue and green [82], suggesting that thinner part of thin film is more resistive than that for thick part. This result indicates that it is very important to grow even thin films with less grain boundaries and possibly

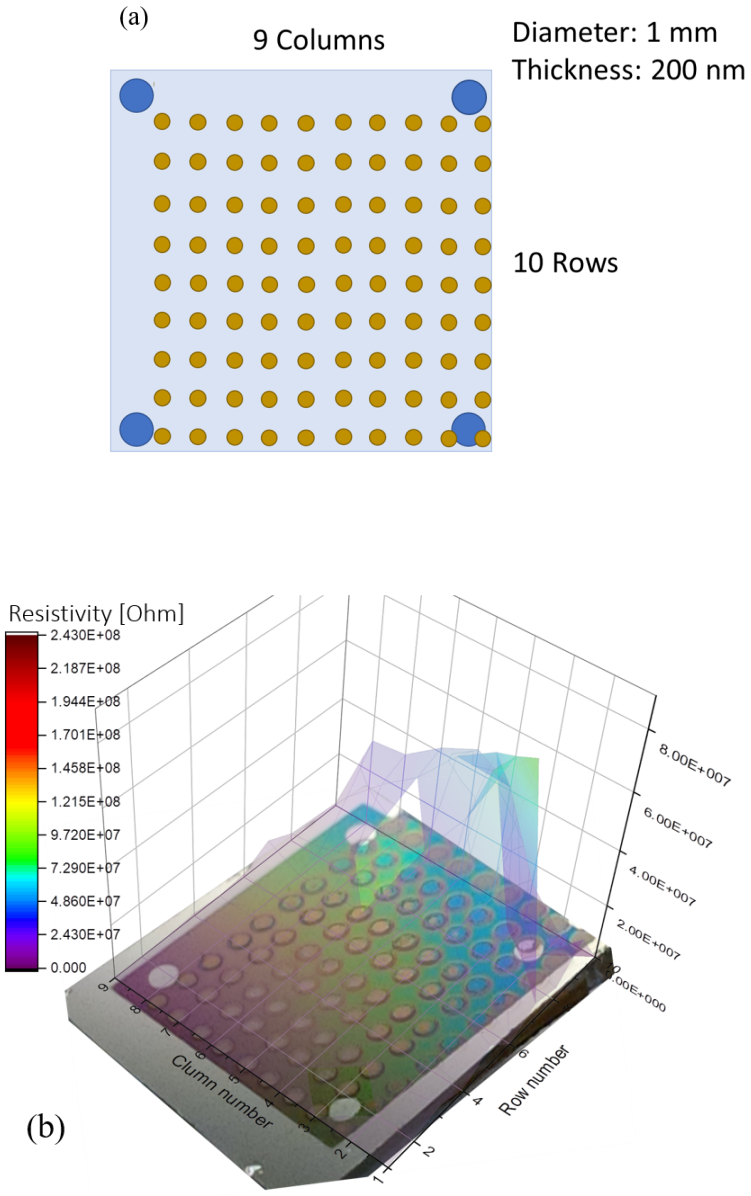

Figure 5.3: (a) Schematic of sample structure for I-V measurement and (b) I-V result for TiO_2:Sm.

it is better to apply bias voltage vertically.

Secondly, a thin film is fabricated on a conductive $SrTiO_3$:Nb substrate with Schottky contacts on the top. $SrTiO_3$:Nb is used for a backside Ohmic contact. This *vertical* sample structure is shown in Fig. 5.4. The bias voltage can be applied vertically using this system.

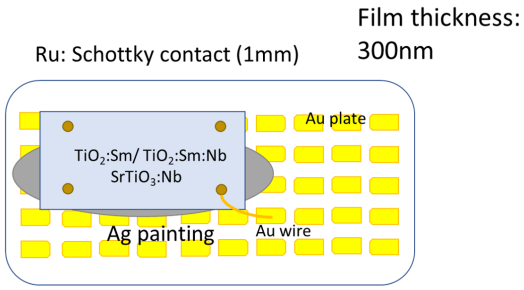

Figure 5.4: Schematic of sample structure (Vertical).

Figure 5.5 illustrates I-V curves for this TiO_2:Sm:Nb device. All 4 contacts on the sample (d1-d4) showed Ohmic characteristics at both direction of applied voltage. This result suggests that TiO_2 is resistive when it is applied voltage laterally. However, it is relatively conductive when voltage applied vertically. We can assume that the grain boundaries on the surface increase the surface resistivity. TiO_2 is relatively conductive when voltage applies vertically so that Nb-doped TiO_2 is too conductive with so many carriers to make the depletion layer thinner.

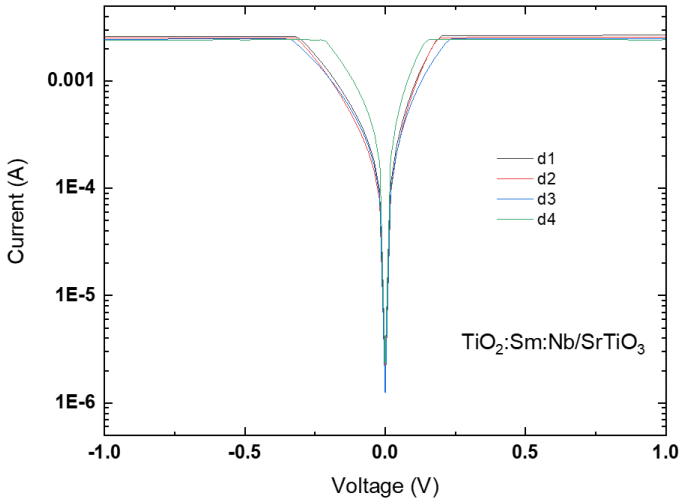

Figure 5.5: I-V result for TiO_2:Sm:Nb with vertical application of voltage.

5.3.2 SEM and XRD with different fabricating conditions to improve crystallinity

The previous section revealed the problem of laser ablation: roughness of the sample surface. According to this result, we tried two different approaches to improve crystallinity as follows:

1. Change the cooling rate after post annealing
2. Change the growth rate during deposition by laser ablation

The first approach was employed based on the study by S Asalzadeh et al, reporting that drastic cooling produces smaller grain size, less rough surface and higher conductivity on TiO_2 thin films [83]. TiO_2:Sm samples for No. 1 were prepared on $SrTiO_3$:Nb

substrate by laser ablation as our usual conditions for fabricating anatase-phase (please find Chap. 3). Thickness of thin films are approximately 300 nm, and distance between substrate and target was 45 mm. After deposition, samples were annealed at 700 °C for 10 min with oxygen atmosphere. Then, 3 different cooling rates were tried as 20 °C/min, 10 °C and 6.8 °C.

Figure 5.6 illustrates SEM image for TiO_2:Sm with 3 different cooling rates. Images were observed by SE2 mode with 4 keV and magnitude was $\times$ 40 K. For 6.8 °C cooled sample showed slightly smaller crystallines than that for others, whilst crack was observed on surface of 20 °C annealed which was possibly caused by quick cooling.

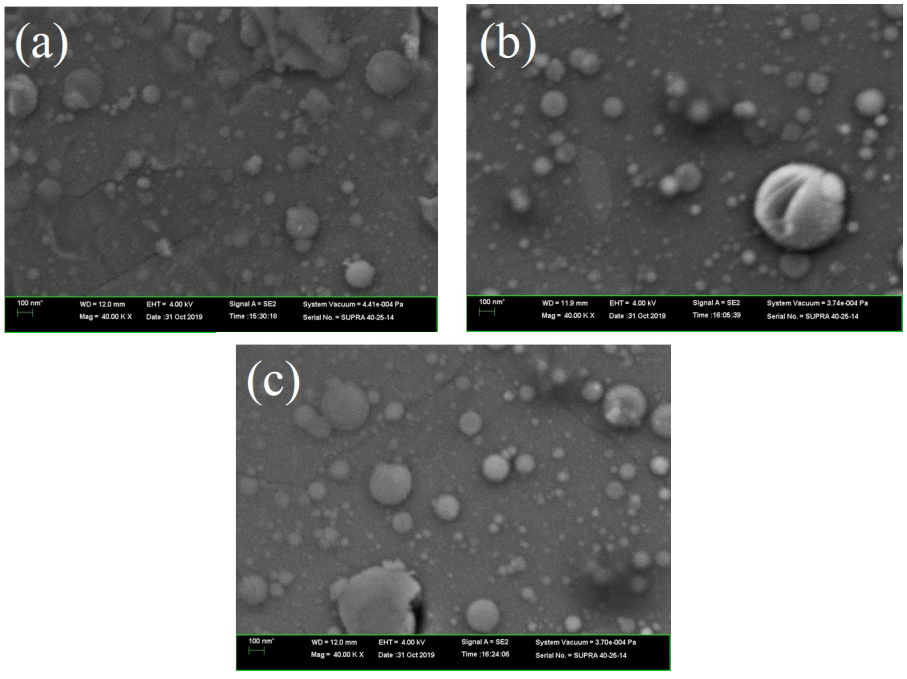

Figure 5.6: SEM image of TiO_2:Sm samples cooled down (a) 6.8°C/min, (b) 10°C/min and 20°C/min after annealing.

Figure 5.7 shows grain size of TiO_2:Sm thin films with different cooling rates (6.8, 10, 20 °C). Grain size was obtained from calculation through the Scherrer equation on XRD result. 10 °C seems slightly larger than the others, however, significant change in grain size was not observed. These results suggest that cooling rate after annealing effects on crystallinity of thin films, and improves the surface roughness, but it does not give a huge impact.

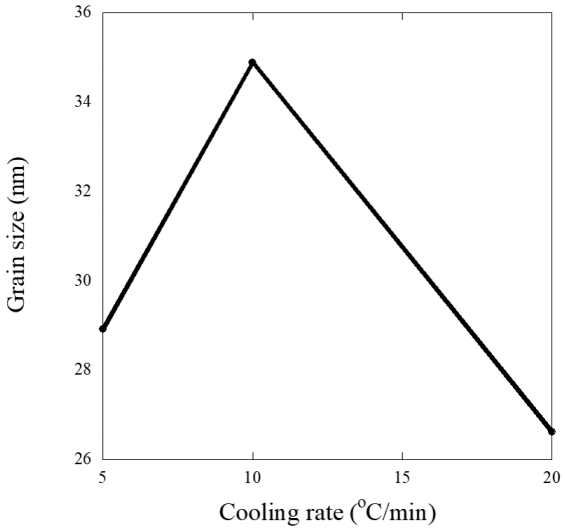

Figure 5.7: Grain size of TiO_2:Sm thin films with different cooling rates (6.8, 10, 20 °C).

Different distance between a substrate and a target in a growth chamber during laser ablating was employed for the second approach to improve crystallinity of thin films. It is expected that longer distance leads to reduction of droplets because heavy molecules would fall out on the way to a substrate, and to slow down the growth rate. This time, we selected 2 different target-substrate distances as 45 mm and 60 mm. After deposition,

samples were annealed at different temperature in the range of 500 °C to 700 °C with 100 °C intervals. Each temperature has the variation of annealing time: 30 min and 1 h. Figure 5.8 shows SEM image of TiO_2:Sm samples with target-substrate distance of (a) 45 mm and (b) 60 mm with annealing at 500 °C for 30 min, 4 keV and magnitude of 5000. For the sample fabricated with 45 mm target-substrate distance showed much more droplets on surface and larger holes than that for fabricated with 60 mm distance sample. This suggests that distance between target and substrate is effective for reducing droplets.

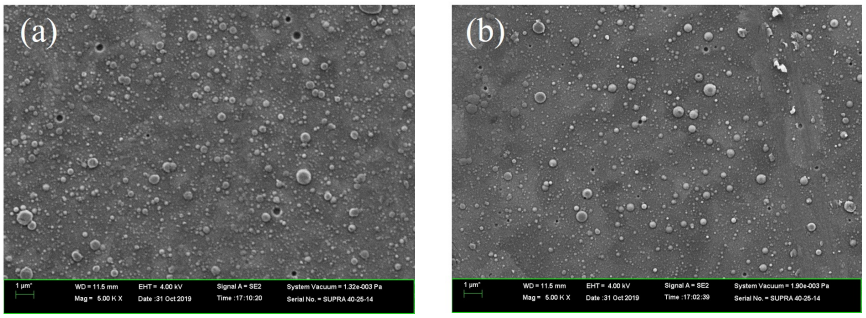

Figure 5.8: SEM image for TiO_2:Sm samples fabricated with the substrate distance of (a) 45 mm and (b) 60 mm to a target with annealing at 500 °C for 30 min.

Figure 5.9 illustrates SEM image for TiO_2:Sm samples with target-substrate distance of (a) 45 mm and (b) 60 mm with annealing at 500 °C for 1 h. The observation conditions were fixed as the previously shown samples for comparison. Droplets on the surface of the sample fabricated with 60 mm target-substrate distance were much less and small holes were smaller than that for the sample with 45 mm substrate distance. Comparing to the samples annealed for 30 min, the sample fabricated with 45 mm does not show much difference. In contrast, for the sample fabricated with 60 mm substrate

distance showed clearer SEM image with slightly larger grains as shown by the XRD measurements.

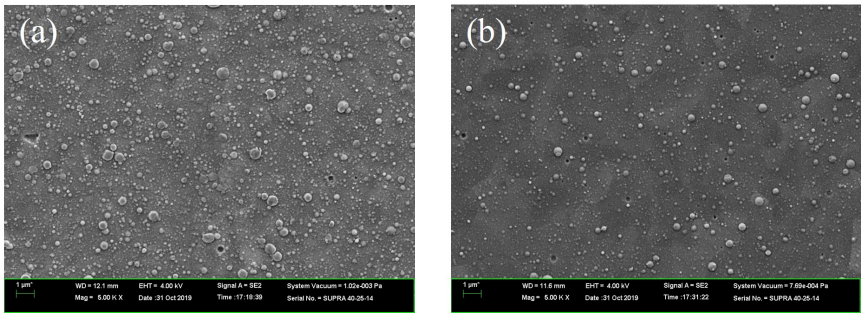

Figure 5.9: SEM image for TiO_2:Sm samples fabricated with the substrate distance of (a) 45 mm and (b) 60 mm to a target with annealing at 500 °C for 1 h.

XRD measurements were performed and grain size was calculated from XRD peak width, describing in Fig. 5.10. Note that dotted lines are for 1 h annealing time whereas solid lines are for 30 min. Grain size of samples fabricated with longer substrate distance was larger than that for samples fabricated with shorter substrate distance at any annealing temperature or time. Also, for longer substrate distance samples with 1 h annealing increased their grain size with increase of annealing temperature. These results might suggest that longer distance reduce droplets and clusters of molecules so that pure clusters in thin films increased which makes annealing much more effective for crystalline growth rather than mixture of clusters and droplets. At least, this result reveals that longer substrate distance during fabrication is more effective technique for improving crystalline growth than cooling rate in annealing process. Samples shown after this section are fabricated with longer substrate distance for fabrication and 1 h annealing time.

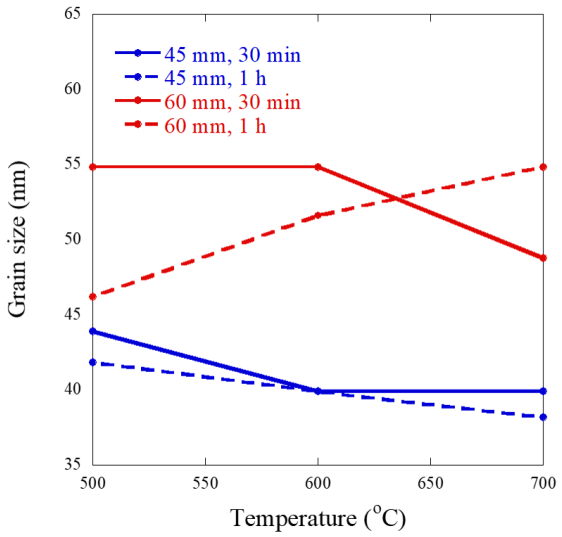

Figure 5.10: Grain size of TiO_2:Sm thin films with different distances between substrate and target and different annealing time (45 mm/60 mm, 30 min/1 h).

5.3.3 Sensitiveness of TiO_2:Sm to an atmosphere in a cryostat with vacuuming

Through these previous sections in Chapter 5, the optimal direction/sample structure of TiO_2:Sm and technique to improve crystallinity were discussed. Now we move on to prerequisite measurements for DLTS such as I-V and C-V, which is as follows:

1. Measure I-V and C-V at RT.

If the leakage current is less than 10^{-4} A at -1 V (I-V), phase angle is bigger than 70° and ΔC (capacitance change) is larger than 1 pF (C-V).

2. Measure I-V and C-V with temperature sweep.

3. Measure DLTS/admittance.

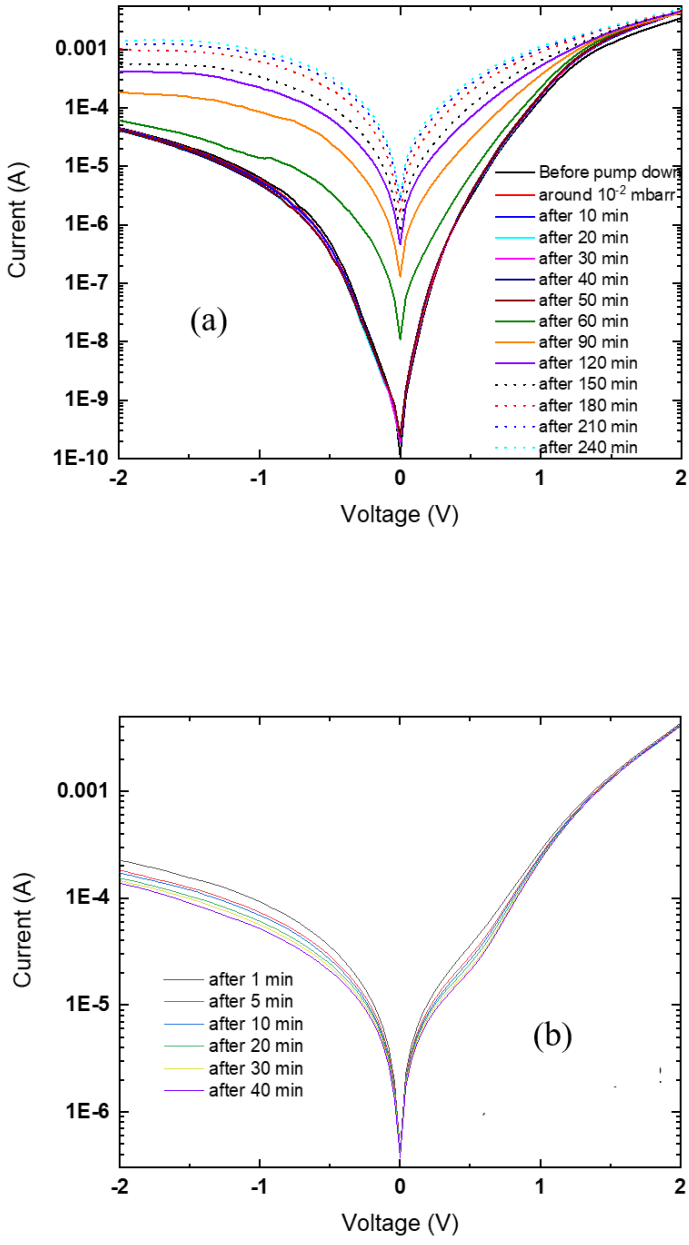

Figure 5.11: I-V curves for TiO_2:Sm with (a) vacuuming and (b) stopped pumping.

The fabrication technique showed in Section 5.3.2 allowed us to succeed in preparing samples with less leakage current and acceptable capacitance change continuously: less than 10^{-4} A at -2 V. For this result, samples were set in a cryostat for temperature sweep. Figure 5.11 (a) shows I-V curves for TiO_2:Sm on $SrTiO_3$:Nb substrate.

Rectifyication was weakened after 1 h vacuuming at RT and stop rectifying in the end. Figure 5.11 (b) shows I-V curves measured after stopping a vacuum pump. Rectification dramatically recovered after stopping vacuuming. These results suggest that the surface was affected by vacuuming since the recovery time for rectification is very quick. There are two possibility assumed as follows:

1. Moistures or gas in a cryostat passivated the surface and caused oxygen vacancies which increases donors around surface causing thinner depletion layer.
2. Moisture or gas introduced new defect level in surface states.

We considered distribution model of donor density of a sample, showing in Fig. 5.12. For a sample with too much donors, donor density decreases with getting close to the surface at RT so that depletion layer becomes thicker. However, at low temperature, the surface levels are changed by gas or moisture, which leads to thinner depletion layer and becomes Ohmic in both direction of applied voltage. It is reported that TiO_2 and some semiconductors sense gases (hydrogen, CO_2 etc) with Pt Schottky contact [84, 85, 86, 87]. Also, Komuro et al reported residual H_2O in a cryostat is absorbed to TiO_2:Er surface at 20 K, and H_2 and O_2 are diffused out by UV illumination by the decomposition of H_2O into OH^- and H^+, changing TiO_2 to Ti_2O_3 [88]. Hydrogen (or

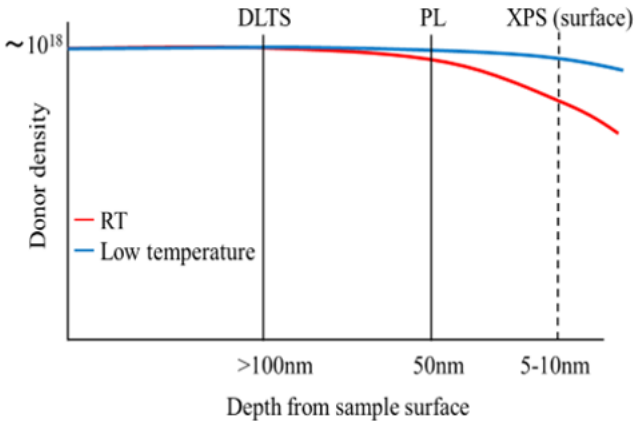

Figure 5.12: Model for donor density distribution of a sample and correlation of depth with measurable technique to evaluate defects.

H_2O) in a cryostat can be the reason which causes this degradation, however, further study including surface estimation using XPS and in-situ I-V observation with different gases using gas exchanger is needed.

5.3.4 Physical property of TiO_2 and TiO_2:Sm

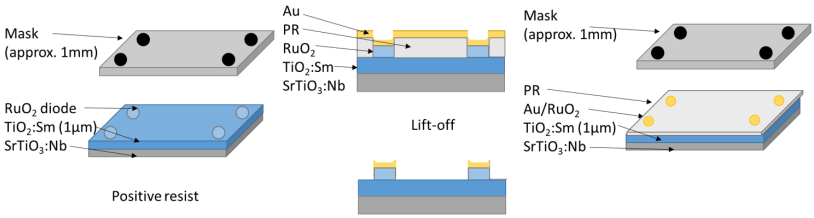

Figure 5.13: Schematic of photoresist capsulation.

To prevent gas/H_2O passivation into the sample surface, samples were capsulated with photoresist (PR). A sample structure with PR coating is the same structure as Fig.

5.4. Sample was glued on a ceramic substrate with Au plates with Ag paint. This time, Ru Schottky contacts were wired to Au plate with an Au wire to prevent damage from putting probes. Figure 5.13 describes process of PR coating. Sample was covered with positive PR except diodes and evaporated Au on the front for lift-off so that Au is removed with resolving PR in solutions. After covering the diodes, sample was coated with positive PR and exposed Xe lamp for capsulation.

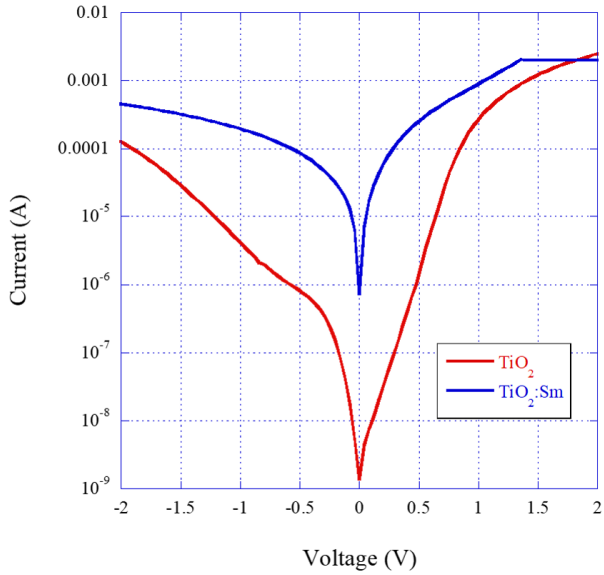

Figure 5.14: I-V curves of photoresist coated TiO_2 and TiO_2:Sm thin films.

I-V curves of photoresist capsulated TiO_2 and TiO_2:Sm thin films are shown in Fig 5.14. Both curves show rectification with relatively acceptable leakage current for DLTS measurement. TiO_2:Sm was more conductive than that for TiO_2. Note that the flat part of TiO_2:Sm (forward bias, 1.7 - 2.0 V) is overflown because the current beyond 1.7 V was higher than 4 mA which is out of the range of a used I-V system. This result suggests that doping Sm enhances conductivity of TiO_2.

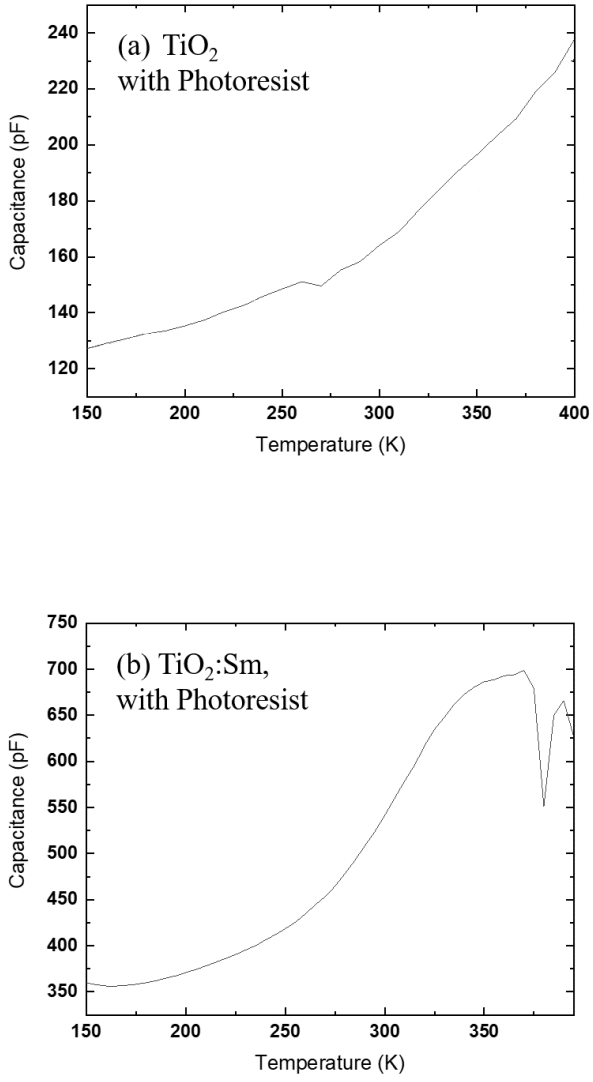

Figure 5.15: C-V results for (a) TiO_2 and (b) TiO_2:Sm.

Figure 5.15 shows C-V curves with temperature sweep from 150 to 400 K for PR coated (a) TiO_2 and (b) TiO_2:Sm. Measurement was performed both forward and backward to make sure there is no effect on capacitance from the atmosphere in a cryostat. Both sample was repeatable for C-V measurement with temperature sweep under the vacuum. Sm-doped sample has approximately three times larger capacitance than undoped TiO_2, suggesting that Sm dopant contributed to increase of carriers. In addition, a broad peak was observed around 300 to 350 K for Sm-doped sample. This result indicates that Sm-related defect was formed in this sample.

C-V result measured for these samples at RT replotted to $1/C^2$ as a function of voltage is shown in Fig. 5.16 to calculate donor density N_D and built-in potential ϕ_B. As discussed in Section 2.5.2, Chapter 2, $1/C^2$ against V_{bias} produces a straight line if the doping concentration is uniform. The doping concentration ($N_A{}^-$, $N_D{}^+$) can be determined from the slope in the plot. The depletion region of a Schottky diode behaves like a parallel plate capacitor, and they can be written using the equation 2.5.8 shown in Chapter 2 as follows:

$$(\frac{A}{C})^2 = \frac{2(V_r + V_{bi})}{q\epsilon_s\epsilon_0 N_d}, \tag{5.3.1}$$

where A is the area of a Schottky contact, V_r is reverse voltage V_{bi} is voltage at intercept, ϵ_s is electron affinity of semiconductor and ϵ_0 is electron affinity under the vacuum. Then, this equation can be written as:

$$C = \frac{\epsilon_s \epsilon_0 A}{W}, \tag{5.3.2}$$

where *W* is the width of the depletion region.

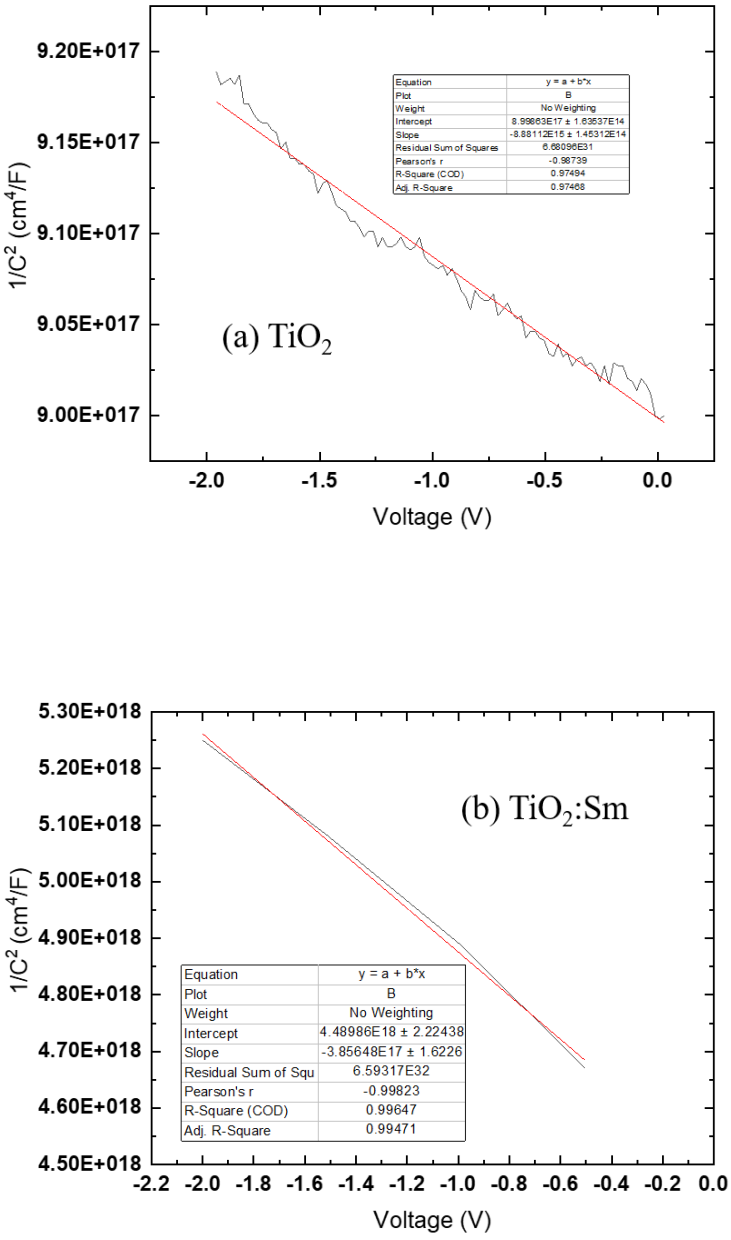

Figure 5.16: $1/C^2$ vs bias voltage for (a) TiO_2 and (b) TiO_2:Sm.

Table 5.1 demonstrates calculated donor density N_D and built-in potential ϕ_B for TiO_2 and TiO_2:Sm. Sm-doped sample has donor density two orders of magnitude more and a built-in potential is slightly smaller about 0.1 eV than undoped TiO_2 sample, indicating that Sm increased donor density of TiO_2. In addition, this result suggests that increased carriers by Sm doping plays a role to determine electrical conductivity of TiO_2 thin films according to the I-V results shown in Fig 5.14. Doped rare earth satisfies the local charge neutral condition and provides donors to TiO_2. Assumingly, doped rare earth induces oxygen vacancies in TiO_2 and they introduce a donor state which provides donors. Donor state is possibly an intermediate state of the energy transfer so that further studies including DLTS and admittance are expected.

Table 5.1: Donor density (N_D) and built-in potential (ϕ_B).

Sample	N_D /cm^3	ϕ_B eV
TiO_2	1.13×10^{16}	0.52
TiO_2:Sm(1.0 wt%)	2.78×10^{18}	0.43

5.4 Conclusion

We showed electrical property of TiO_2, TiO_2:Sm and TiO_2:Sm:Nb prepared by laser ablation on $SrTiO_3$:Nb. Although TiO_2 is so-called semi-insulator, result showed its acceptable I-V and C-V characteristics when the voltage is applied vertically. 90 Ti Ohmic contacts were deposited on a sample surface to understand the connection between the position of prepared contacts on thin films and resistivity. I-V measurements showed resistivity strongly depended on thickness of thin films: resistivity increased when we measure I-V with a contact prepared on a thinner part in thin film. These

results suggest that applying voltage vertically is better for TiO_2-based samples to avoid crystal boundaries and TiO_2:Sm:Nb is far too conductive to have a depletion layer so that it is not suitable for an active layer in LED structure. To reduce leakage current of samples and noises, samples were tried to improve their crystallinity with 2 different approaches: controlling cooling rate after annealing and distance between target and substrate during ablation to decrease growth rate. SEM images and XRD results showed there was not much difference of grain size or surface condition between different cooling rates, whereas longer substrate distance was effective to grow larger grains and reduce droplets. In addition, longer substrate distance enhances annealing influence on thin films for crystalline growth: longer substrate distance increased grain size of samples with longer annealing time. This result indicates that longer substrate distance reduces mixture of clusters of TiO_2:Sm or Sm_2O_3 (a laser just scraped a target so that bonds between atoms are not well separated by a laser) and droplets.

TiO_2:Sm on $SrTiO_3$:Nb was set in a cryostat to measure I-V with temperature sweep for preparation to DLTS and admittance measurements. The rectification became weaker after 1 h vacuuming at RT, and it stopped rectifying in the end. A vacuum pump was turned off after 240 min vacuuming, then rectification was quickly recovered, suggesting that gas or H_2O passivated into TiO_2:Sm surface and increased donor density of thin film or it introduced defect level. Further study such as surface estimation (XPS) and check the different gas effect on I-V and C-V characteristics of samples with gas exchanger is necessary.

I-V measurement for TiO_2 and TiO_2:Sm thin films revealed that Sm doping enhances electrical conductivity of TiO_2. TiO_2 and TiO_2:Sm were capsulated by photoresist to

prevent passivation of gas/H_2O. This technique allowed us to successfully measure temperature sweep C-V. Sm-doped sample showed three times larger capacitance than that for undoped TiO_2 with a huge capacitance change about ΔC = 350 pF. C-V curves measured at RT were replotted to $1/C^2$ against voltage for obtaining information of donor density N_D and built-in potential ϕ_B. Donor density for Sm-doped sample was two orders of magnitude larger, and a built-in potential was about 0.1 eV smaller than that for TiO_2 sample. This result suggests that Sm-doping increases donor density in TiO_2 thin films and increased carriers by Sm doping are responsible for determination of electrical conductivity of TiO_2. In addition, this result indicates that rare earth-doped TiO_2 thin films do not need other co-dopants such as Nb for increase of conductivity because rare earth-doping provides enough carriers to enhance conductivity. Assumingly, these donors make an intermediate state near the band gap of TiO_2 which plays an important role in the energy transfer.

This project is still not completed, however, we could yield detailed electrical and physical property of TiO_2. Further studies including DLTS and admittance to estimate defect states in TiO_2 are strongly expected.

Chapter 6

Conclusion

In this thesis, we discussed optical, electrical and local fine structural properties of TiO_2:Sm thin films. Photoluminescence (PL) measurements were carried out for optical characterisation, I-V and C-V measurements were employed for electrical characterisation and X-ray Absorption Fine Structure (XAFS) measurements were performed for local fine structural characteristion. All samples were fabricated by laser ablation and post annealed for optical activation of rare earth ions and nano-meter size crystalline growth.

Firstly, the connection between luminescent and local structural properties of TiO_2:Sm as a function of annealing temperature and comparison between 2 different crystalline phases of TiO_2 were discussed. Anatase- and rutile-phase Sm-doped (1.0 wt%) TiO_2 thin films were prepared and treated by post annealing at 8 different temperatures, which is in the range of 400 °C to 1100 °C with 100 °C intervals. PL measurement reveals sample prepared as anatase-phase TiO_2 showed much more intense

luminescence, 200 times stronger at maximum, than rutile-phase samples, indicating that anatase-TiO_2 is a better candidate for application of optoelectrical devices. For anatase-phase sample, PL intensity increased with increase of annealing temperature up to 700 °C and decreased above 700 °C. Distorted local fine structure with strongly emitting anatase-samples was revealed by XAFS analysis, and which became more distorted with increasing PL intensity. In contrast, rutile-samples showed good agreement with high symmetrical model for curve fitting. These results suggest that distortion in local fine structure plays a very important role for enhancing Sm-related luminescence.

Secondly, the connection between luminescent and local structural properties of TiO_2:Nd as a function of Al concentration and comparison of luminescent property between indirect (host-meditated) and direct (host semiconductor is not involved with exciting rare earth ions) excitation PL. TiO_2:Nd(1.0 wt%):Al(0, 0.1, 1.0, 5.0 wt%) thin films were fabricated as anatase-phase and annealed at 500 °C for 3 min. For indirect PL intensity increased with increasing Al concentration, and change in spectral shape and peak shift were observed for Al 1.0 and 5.0 wt%-co-doped samples. In contrast, direct excitation PL intensity decreased with increase of Al concentration. These results indicate Al co-doping enhances luminescence from Nd^{3+} ions under indirect excitation, and Al changes in crystal field around Nd^{3+}, which determines the transition probability (and energy distribution) of the luminescent centre, changing the PL fine structure. Co-doping Al decreased the number of pure (808 nm) Nd^{3+} centres and made a mixture of various Nd^{3+} centres and pure Nd^{3+} centres. PL time response showed the rise and decay lifetimes were increased with increasing Al concentration, suggesting a reduction in non-radiative recombination, which is consistent to the more

intense PL intensity. XAFS analysis revealed that local fine structure of samples with higher Al concentration with intensive emitting was distorted. This result correlates to PL result namely, change in PL fine structure and stronger emissions. Again, the result suggests that distortion in co-ordination around the luminescent centre is responsible for enhancing luminescence.

Quantitative and highly accurate estimations of local fine structure of rare earth, the luminescent centres with different approaches to enhance rare earth-related emissions, were successfully done. In addition, it is the first time to achieve quantitative, metrical and accurate estimations of the second nearest neighbour of rare earth ions. Especially, change in an atomic distance between rare earth and the second nearest neighnour was never discussed because of the difficulty of obtaining clear XAFS signals with low noise level and improving accuracy of fitting analysis. Distortion of the second nearest neiboughr of rare earth is possibly a better environment for enhancing energy transfer. Because the intermediate state can exist near the second nearest neighbour (Ti) of rare earth and distortion (or optimal bond length) introduces better potential valleys for energy transfer.

Finally, we showed some brief summary of electrical measurements such as I-V and C-V for TiO_2, TiO_2:Sm(1.0 wt%) and TiO_2:Sm(1.0 wt%):Nb(11.0 wt%). These are prerequisite measurements and preparation for measuring DLTS/admittance to follow behaviour of electron-hole pairs and to find rare earth-related defect which possibly is responsible for energy transfer as a intermediate level in TiO_2 host. TiO_2 is relatively conductive when voltage applies vertically although it is reported as resistive semiconductor. TiO_2:Sm:Nb was prepared to use as a conductive active layer, however, it is too

conductive with vertical application of voltage. It is very difficult to fabricate thin films with flat and even surface using laser ablation. IV measurement for sample with 90 Ti Ohmic dots revealed that thickness and evenness crucially affects on electrical property, especially on resistivity. To solve these issues and improve crystallinity of samples to reduce leakage current and noises, we empoyed 1. different cooling rate after annealing and 2. different target-substrate distance during fabrication. Difference of cooling rate after annealing did not show significant difference in grain size and surface condition. In contrast, we succeeded in reducing droplets and grew larger crystalline grains with longer substrate distance.

IV measurement with temperature sweep was carried out, and sample rectification of Ru/TiO_2:Sm/$SrTiO_3$:Nb became weaker with vacuuming after 1 h and stopped rectification in the end. However, rectification recovered right after stopped vacuum pump. This result revealed that TiO_2 is very sensitive to H_2O or gas which possibly is passivated into the TiO_2 surface and increase donor density around the surface or introduced new defect level in TiO_2 surface states. TiO_2:Sm on $SrTiO_3$:Nb substrate was capsulated with photoresist to avoid this *gas/H_2O passivation effect*. IV curves for TiO_2 and TiO_2:Sm were rectified in both samples and Sm-doped sample showed higer conductivity than that for undoped TiO_2. We succeeded in measuring C-V with temperature sweep without any affection from atmosphere in a cryostat and most importantly, measurements were repeatable. C-V with temperature sweep revealed that Sm-doped sample has larger carriers than TiO_2 sample and a broad peak was found around 300-350 K, suggesting that there is Sm-related defect was formed in TiO_2. C-V measured at RT result was replotted to $1/C^2$ to obtain information of donor density and built-in

potential of TiO_2 and TiO_2:Sm. Sm-doped sample had two orders of magnitude larger donor density than TiO_2 sample. These results indicates that Sm-doping introduces donors in TiO_2 and increased carriers by Sm doping which takes a role to determine electrical conductivity of TiO_2 thin films. This suggests that rare earth-doped TiO_2 thin films have enough carriers provided by rare earth doping thus they have no need of co-doping other metals such as Nb to enhance their conductivity. Assumingly, these donors make an intermediate state near the band gap of TiO_2 which plays an important role in the energy transfer. The further study of estimation of defects in TiO_2 such as DLTS and admittance is expected.

We conclude that local fine structure is surely responsible for enhancing emission and XAFS analysis is one of the effective and essential estimation for understanding luminescent property of rare earth phosphors: fixing the environment around rare earths as the reported optimal local structure for rare earths simply introduce the luminescent centre with strong emissions. However, it is also important to find the route of energy transfer from the host materials to rare earths and how we can improve efficiency of excitation of rare earths. An image of luminescence enhancement now we have is that distortion is possibly one of the blades in the gear which makes rare earths-related luminescence- and these gears need to be exactly fit with each other for the strong emissions. Rare earth-related defect is possibly one of these gears or it might help us to understand the system.

Bibliography

[1] Critical raw materials in lighting applications: Substitution opportunities and implication on their demand, C C Pavel, *phys status solidi (a)*, 2016, **213**, 11.

[2] Rare Earth Element Geochemistry, P Henderson, *Elsevier*, ISBN 04444421483.

[3] Rare Earth Elements: What and Where They Are, V Zepf, *a Chapter in Rare Earth Elements, Springer*, ISBN 9783642354588, 11-39.

[4] Chemistry of the rare-earth elements, N E Topp, *J Chem Educ*, 1966, **43**, 2, A160.

[5] Introduction to Solid State Physics, C Kittel, *Wiley*, **8th edition** ISBN 047141526X.

[6] Inorganic Chemistry, C E Housecroft and A Sharpe, *Pearson Edu Lim*, ISBN 9781292134161.

[7] The Lanthanide Contraction, B E Douglas, *J Chem Educ*, 1954, **31**, 11, 598.

[8] Lanthanide contraction and magnetism in the heavy rare earth elements, I D Hughes, M Dane, A Ernst, W Hergert, M Luders, J Poulter, J B Staunton, A Svane, Z Szotek and W M Temmerman, *Nature Lett*, 2007, **446**, 650-653.

[9] Quantum Mechanics, A S Davydov, *Elsevier*, ISBN 978080204383.

[10] New Regularities In The Spectra Of The Alkaline Earth, H N Russell and F A Saunders, *Astrophys J*, 1925, **61** 38-68.

[11] Recent developments in rare-earth doped materials for optoelectronics, A J Kenyon, *Prog Quantum Electron*, 2002, **26**, 4-5, 225–84.

[12] Rare Earth Materials: Properties and Applications, A R Jha, *Routledge*, ISBN 1138033871.

[13] Science of Rare Earths, G Adachi, *Kagakudojin*, IBSN 475980806X.

[14] Luminescent Materials, G Blasse and B C Grabmaier, *Springer*, IBSN 0387580190.

[15] Rare-Earth Doped III-Nitrides for Optoelecrtronic and Spintronic Applications, K O'Donnell, K Peter and D Volkmar, *Springer*, ISBN 9789048128761.

[16] 50th annivesary of the Judd-Ofelt theory: An expeimentalist's view of the formalism and its application, M P Hehlen, M G Brik and K W Kramer *J Lumin*, 2013, **136**, 221-239.

[17] Energy Level Diagrams and Extranuclear Building of the Elements, R N Keller, *J Chem Edu*, 1962, **39**, 6, 289-293.

[18] The intensity of the 173 nm emission of LaFs3:Nd3+ scintillation crystals, P Dorenbos, J T M de Haas and C W E van Eijik, 1996, *J Lumin*, **69**, 229-233.

[19] From Lighting To Photoprotection: Fundamentals and Applications of Rare Earth Materials, P C de S Filho, J F Lima and O A Serra, *J Braz Chem Soc*, 2015, **26**, 12, 2471-2495.

[20] The surface science of titanium dioxide, U Diebold, *Surf Sci Rep*, 2003, **48**, 5-8, 53-229.

[21] Doped-TiO_2: A Review, A Zaleska, *Recent Pat Eng*, 2009, **2**, 157-164.

[22] Review on: Titanium Dioxide Applications, A J Haider, Z N Jameel and I H M Al-Hussaini, *Energy Procedia*, 2019, **157**, 17-29.

[23] Electrical properties of nanocrystalline anatase TiO_2 thin films with different crystallite size, B Huber, H Graser and C Ziegler, *Surf Sci*, 2004, **566-568**, Part 1, 419-424.

[24] Synthesis and applications of nano-TiO_2: a review, M T Noman, M A Ashraf and A Ali, *Environ Sci Pollut R*, 2019, **26**, 3262-3291.

[25] Review on Undoped/Doped TiO_2 Nanomaterial; Synthesis and Photocatalytic and Antimicrobial Activity, S Yadav and G Jaisear, *J Chin Chem Soc*, 2016 **64**, 103-116.

[26] A mini-review on rare earth metal-doped TiO_2 for photocatalytic remediation of waste water, N U Saqib, R Adnan and I Shah, *Environ Sci Pollut R*, 2016, **23**, 15941-15951.

[27] Review of functional titanium oxides. I: TiO_2 and its modifications, N Rahimi, R A Pax and E M Gray, *Prog Solid State Ch*, 2016, **44**, 3, 86-105.

[28] Correlation between anatase-to-rutile transformation and grain growth in nanocrystalline titania powders, X Z Ding and X H Liu, *J Mater Res*, 1998, **13**, 9, 2556-2559.

[29] Comparison of the electronic structure of anatase and rutile TiO_2 single-crystal surfaces using resonant photoemission and x-ray absorption spectroscopy, A G Thomas, R Stockbauer, S Warren, T K Johal, S Patel, D Holland, A T Ibrahimi and F Wiame, *Phys Rev B*, 2007, **75**, 3, 035105.

[30] Semiconductor Material and Device Characterization, D K Schroder, *Wiley*, ISBN 0471739065.

[31] Laser Ablation, R E Russo, *Appl Spectrosc*, 1995, **49**, 9, 14A-28A.

[32] Laser ablation inductively coupled plasma mass spectrometry: achievements, problems, prospects, S F Durrant, *J Anal At Spectrom*, 1999, **14**, 1385-1403.

[33] Laser Spectroscopy 1, W Demtroder, *Springer*, ISBN 9783642538582.

[34] Annealing, W F Hosford, *in Iron and Steel, Cambridge University Press*, ISBN 076132111X, 51-65.

[35] Recrystallization and Related Annealing Phenomena, F J Humphreys and M Hatherly, *Pergamon*, ISBN 9780080441641.

[36] Photoluminescence properties of samarium-doped TiO_2 semiconductor nanocrystalline powders, L Hu, H Song, G Pan, B Yan, R Qin, Q Dai, L Fan, S Li and X Bai, *J Lumin*, 2007, **127**, 371-376.

[37] Luminescence properties of sol-gel-derived TiO_2:Sm powder, V Kiisk, V Reedo, O Sild and I Sildos, *Opt Mater*, 2009, **31**, 1376-1379.

[38] Luminescence properties of Sm^{3+}-doped TiO_2 thin films prepared by laser ablation, F Jing, S Harako, S Komuro and X Zhao, *J Phys D: Appl Phys*, 2009, **42**, 085109.

[39] Sensitization effect of Al co-doping on Nd-related photoluminescence in TiO_2 matrix, Y Aizawa, T Ohtsuki, S Harako, S Komuro and X Zhao, *Jpn J Appl Phys*, 2014, **53**, 6, 06JG06.

[40] X-ray Characterization of Materials, E Lifshin, *Wiley-VCH*, 1999, ISBN: 9783527613755.

[41] X-ray Diffraction: Modern Experimental Techniques, O H Seeck and B Murphy, *Pan Stanford*, ISBN 9789814303590.

[42] Application Of X-ray Diffraction Techniques To Semiconductor Materials Caracterization, S S Laderman , M Scott, R Smith and A Nel, *Proc SPIE*, 1985, **0524**.

[43] X-ray Diffraction Procedures for Polycrystalline and Amorphous Materials, P Klug and L E Alexander, *Wiley, New York*, 1974, ISBN: 9780471493693.

[44] Photoluminescence and Structural Analysis of Samarium Doped TiO_2 Thin Films and Their Applications to Visible LEDs, M Murayama, K Yoda, K Shiraishi, S Guan, S Komuro and X Zhao, *OPJ*, 2018, **8**, 5, 146-164.

[45] Fundamentals of XAFS, M Newville, *Rev Mineral Geochem*, 2014, **78**, 1, 33-74.

[46] Introduction to XAFS, G B Bunker, *Cambridge University Press*, ISBN 9780521767750.

[47] X-ray absorption fine structure and nanostructure, S W Han, 2006, *Int J Nanotechol*, 2006, **33**, 3, 396-413.

[48] Some notes on XAFS measurement: hole and thickness effects, Y Takahashi, *Jap Magazine of Mineralogical and Petrological Sci*, 2016, **45**, 93-98.

[49] Optical Measurement Techniques, R Myllyla, R Myllyla and A V Priezzhev, *Springer*, ISBN 9783540719267.

[50] Optical characterization of semiconductors: infrared, Raman, and photoluminescence spectroscopy, S Perkowits, *Elsevier*, ISBN 9780080984278.

[51] Silicon photonic materials obtained by ion implantation and rapid thermal processing, I F Crowe, *PhD Thesis to the University of Manchester*, 2010.

[52] Radiative and non-radiative transitions of excited Ti^{3+} cations in sapphire, A Shirakov, Z Burshtein, Y Shimony, E Frumker and A A Ishaaya, *Sci Rep*, 2019, **9**, 18810.

[53] SEM microcharacteraization of semiconductors, D B Holt et al, *Elsevier*, ISBN 9780123538550.

[54] ATHENA, ARTEMIS, HEPHAESTUS: data analysis for X-ray absorption spectroscopy using FEFF, B Ravel et al, 2005, *J Synchrotron Rad* **12**, 537-541.

[55] Metal-Semiconductor Contacts, E H Rhoderick, *Elsevier*, ISBN 0198593368.

[56] Graphene Schottky diodes: An experimental review of the rectifying graphene/semiconductor heterojunction, A D Bartolomeo, *Phys Rep*, 2016, **606**, 1-58.

[57] Tuning the electronic band alignment properties of TiO_2 nanotubes by boron doping, S S Surah, M Vishwakarma, R Kumar, R Nain, S Sirohi and G Kumar, *Results Phys*, 2019, **12**, 1725-1731.

[58] Preparation of Ruthenium Metal and Ruthenium Oxide Thin Films by a Low-Temperature Solution Process, Y Murakami, P T Tue, H Tsukada, J Li and T Shimoda, *JAIST Repository, Conference paper for Green Device Research Center*, 2013, http://hdl.handle.net/10119/12159.

[59] CRC Handbook of Chemistry and Physics, D R Lide, *J Am Soc*, 2008, **130**, 1, 382.

[60] Thermal and optical emission and capture rates and cross sections of electrons and holes at imperfection centers in semiconductors from photo and dark junction current and capacitance experiments, C T Sah, L Forbes, L L Rosier and A F Tasch Jr, *Sol-Stat Electron*, 1970, **13**, 759-788.

[61] Tutorial: Junction spectroscopy techniques and deep-level defects in semiconductors, A R Peaker, V P Markevish and J Coutinho, *J Appl Phys*, 2018, **123**, 161559.

[62] Bulk Lifetime Limiting Defects in Czochralski Silicon and Graphene Oxide as a Surface Passivation Material, M V Contreras, *PhD Thesis to the University of Manchester*, 2018.

[63] DLTS Study of Recombination Active Defects In Sokar Silicon, J Mullins, *PhD Thesis to the University of Manchester*, 2018.

[64] Electrical and Optical Defect Evaluation Technique for Electronic and Solar Grade Silicon, A R Peaker and V P Markevich, *In Defects and Impurities in Silicon Materials, Springer*, 2015, IBSN 9784431558002.

[65] Study on atomic coordination around Er doped into anatase- and rutile TiO_2: Er-O clustering dependent on the host crystal phase, M Ishii, S Komuro and T Morikawa, *J Appl Phys*, 2003, **94**, 3823.

[66] Atomic-scale distortion of optically activated Sm dopants identified with site-selective X-ray absorption spectroscopy, M Ishii, I F Crowe, M P Halsall, B Hamilton, Y Hu, T K Sham, S Harako, X Zhao and S Komuro, *J Appl Phys*, 2013, **114**, 133505.

[67] Photoluminescence Enhancement and Change in the Second Nearest Neighbor Distance of Sm-Doped TiO_2 Thin Films, M Murayama, K Yoda, K Shiraishi, I F Crowe, S Komuro and X Zhao, *Phys Status Solidi B*, 2019, 1800522.

[68] Review of the Anatase to Rutile Phase Transition, D A H Hanaor and C Sorrell, *J Mater Sci*, 2011, **45**, 4, 855-874.

[69] Theoretical prediction of local distortion in an ErO_3 cluster: Stabilization of a C_{4v} structure by a rack and ponion effect, M Ishii and Y Komukai, *App Phys Lett*, 2001, **79**, 7.

[70] Effect of Bi^{3+} ions on luminescence properties of $ZnWO_4$:Eu^{3+}, Sm^{3+}, Bi^{3+} nanorods, M Zhao, D Liu, S Ma and K Wang, *J Mater Sci*, 2018, **53**, 11512-11523.

[71] Effect of silver ions on nthe energy transfer from host defects to Tb ions in sol-gel silica glass, A E Abbass, H C Swart and R E Kroon, *J Lumin*, 2004, **160**, 22-26.

[72] Electron-spin-echo envelope-modulation study of distance between Nd^{3+} ions and Al^{3+} ions in the co-doped SiO_2 glasses, K Arari, S Yamasaki, J Isoya and H Namikawa, *J Non-Cryst Solids*, 1996, **196**, 216-220.

[73] Dissolution of rare-earth clusters in SiO_2 by Al codoping: A microscopic model, J Laegsgaard, *Phys Rev B*, 2002, **65**, 174114.

[74] Reabsorption cross section of Nd^{3+}-doped quasi-three-level lasers, F Chen, J Sun, R Yan and X Yu, 2019, *Sci Rep*, **9**, 5620.

[75] Effect of Al co-doping on the luminescence properties of Nd^{3+}-doped TiO_2 thin films, M Murayama, K Yoda, S Komuro, I F Crowe and X Zhao, *J Lumin*, 2019, **216**, 116656.

[76] Influence of Al on the local structure of Nd-doped TiO_2 thin films: A combined luminescence and X-ray absorption fine structure analysis, M Murayama, K Yoda, S Komuro, H Nitani, I F Crowe and X Zhao, *Mater Sci & Eng B*, 2019, **246**, 49-52.

[77] Time response of 1.54 μm emission from highly Er-doped nanocrystalline Si thin films prepared by laser ablation, S Komuro, T Katsumata, T Morikawa, X Zhao, H Isshiki and Y Aoyagi, *Appl Phys Lett*, 1995, **74**, 377.

[78] 1.54 μm emission dynamics of erbium-doped zinc-oxide thin films, S Komuro, T Katsumata, T Morikawa, X Zhao, H Isshiki and Y Aoyagi, *Appl Phys Lett*, 2000, **76**, 3935.

[79] Fabrication of highly conductive $Ti_{1-x}Nb_xO_2$ polycrystalline films on glass substrates via crystallization of amorphous phase grown by pulsed laser deposition, T Hitosugi, A Ueda, S Nakao, N Yamada, Y Furubayashi, Y Hirose, T Shimada and T Hasegawa, *Appl Phys Lett*, 2007, **90**, 212106.

[80] A transparent metal: Nb-doped anatase TiO_2, Y Furubayashi, T Hitosugi, Y Yamamoto, K Inaba, G Kinoda, Y Hirose, T Shimada and T Hasegawa, *Appl Phys Lett*, 2005, **86**, 252101.

[81] Doping and compensation in Nb-doped anatase and rutile TiO_2, H-Y Lee and J Robertson, *J Appl Phys*, 2013, **113**, 213706.

[82] Color chart for thin SiC films grown on Si substrates, L Wang, S Dimitrijev, G Walker, J Han, A Iacopi, P Tanner, L Hold, Y Zha and F Iacopi, *Mater Sci Forum*, 2013, **740-742**, 279-282.

[83] The Effect of Various Annealing Cooling Rates on Electrical and Morphological Properties of TiO_2 Thin Films, S Asalzadeh and K Yasserian, *Semiconductors*, 2019, **53**, 12, 1603-1607.

[84] Deep Level Transient Spectroscopy Analysis of an Anatase Epitaxial Film Grown by Metal Organic Chemical Vapor Deposition, T Miyagi, T Ogawa, M Kamei, Y Wada, T Mitsuhashi, A Yamazaki, E Ohta and T Sato, *Jpn J Appl Phys*, 2001, **40**, 4B, L404-L406.

[85] Pt/GaN Schottky diodes for hydrogen gas sensors, M Ali, V Camalla, V Lebedev, H Romanus, V Tilak, D Merfield, P Sandvik and O Ambacher, *Sens Actuat*, 2006, **113**, 2, 797-804.

[86] First-Principles study of rectifying properties of Pt/TiO_2 interface, T Tamura, S Ishibashi, K Terakura and H Weng, *Phys Rev B*, 2009, **80**, 195302.

[87] Deep-level transient spectroscopy at platinum/titanium-dioxide hydrogen sensors, L Schnorr, M Cerchez, D Ostermann and T Heinzel, *Phys Status Solidi B*, 2016, **253**, 4, 690-696.

[88] Change in photoluminescence from Er-doped TiO_2 thin films induced by optically assisted reduction, S Komuro, T Katsumata, H Kokai, T Morikawa and X Zhao, *Appl Phy Lett*, 2002, **81**, 25, 4733.